

INFORMATION TO USERS

This manuscript has been reproduced from the microfilm master. UMI films the text directly from the original or copy submitted. Thus, some thesis and dissertation copies are in typewriter face, while others may be from any type of computer printer.

The quality of this reproduction is dependent upon the quality of the copy submitted. Broken or indistinct print, colored or poor quality illustrations and photographs, print bleedthrough, substandard margins, and improper alignment can adversely affect reproduction..

In the unlikely event that the author did not send UMI a complete manuscript and there are missing pages, these will be noted. Also, if unauthorized copyright material had to be removed, a note will indicate the deletion.

Oversize materials (e.g., maps, drawings, charts) are reproduced by sectioning the original, beginning at the upper left-hand corner and continuing from left to right in equal sections with small overlaps.

Photographs included in the original manuscript have been reproduced xerographically in this copy. Higher quality 6" x 9" black and white photographic prints are available for any photographs or illustrations appearing in this copy for an additional charge. Contact UMI directly to order.

ProQuest Information and Learning
300 North Zeeb Road, Ann Arbor, MI 48106-1346 USA
800-521-0600

UMI[®]

University of Alberta

Fast Ion Flows in the Earth's Magnetotail

by

James A. Wanliss ©

A thesis submitted to the Faculty of Graduate Studies and Research
in partial fulfillment of the requirements
for the degree of Doctor of Philosophy

Department of Physics

Edmonton, Alberta

Fall 2000



**National Library
of Canada**

**Acquisitions and
Bibliographic Services**

**395 Wellington Street
Ottawa ON K1A 0N4
Canada**

**Bibliothèque nationale
du Canada**

**Acquisitions et
services bibliographiques**

**395, rue Wellington
Ottawa ON K1A 0N4
Canada**

Your file Votre référence

Our file Notre référence

The author has granted a non-exclusive licence allowing the National Library of Canada to reproduce, loan, distribute or sell copies of this thesis in microform, paper or electronic formats.

The author retains ownership of the copyright in this thesis. Neither the thesis nor substantial extracts from it may be printed or otherwise reproduced without the author's permission.

L'auteur a accordé une licence non exclusive permettant à la Bibliothèque nationale du Canada de reproduire, prêter, distribuer ou vendre des copies de cette thèse sous la forme de microfiche/film, de reproduction sur papier ou sur format électronique.

L'auteur conserve la propriété du droit d'auteur qui protège cette thèse. Ni la thèse ni des extraits substantiels de celle-ci ne doivent être imprimés ou autrement reproduits sans son autorisation.

0-612-59694-X

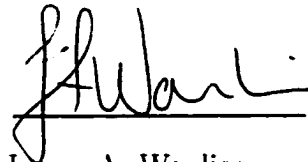
Canada

UNIVERSITY OF ALBERTA
LIBRARY RELEASE FORM

NAME OF AUTHOR: James A. Wanliss
TITLE OF THESIS: Fast Ion Flows in the
Earth's Magnetotail
DEGREE: Doctor of Philosophy
YEAR THE DEGREE GRANTED: 2000

Permission is hereby granted to the University of Alberta library to reproduce single copies of this thesis and to lend or sell such copies for private, scholarly or scientific research purposes only.

The author reserves all other publication and other rights in association with the copyright in this thesis, and except as herein before provided, neither the thesis nor any substantial portion thereof may be printed or otherwise reproduced without the author's prior written permission.



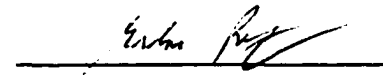
James A. Wanliss
Department of Physics
University of Alberta
Edmonton, Alberta
T6G 2J1

Date: Sept. 6, 2005

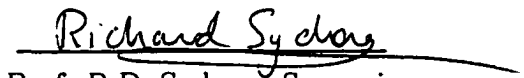
UNIVERSITY OF ALBERTA

FACULTY OF GRADUATE STUDIES AND RESEARCH

The undersigned certify that they have read, and recommend to the Faculty of Graduate Studies and Research for acceptance, a thesis entitled "Fast Ion Flows in the Earth's Magnetotail" submitted by James A. Wanliss in partial fulfilment of the requirements for the degree of Doctor of Philosophy.



Prof. G. Rostoker . Supervisor



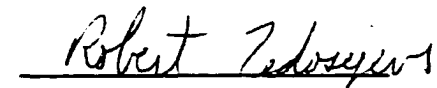
Prof. R.D. Sydora . Supervisor



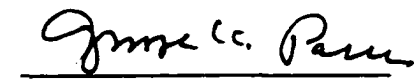
Prof. W. Rozmus



Prof. H.S. Sherif



Prof. R. Fedosejevs



Prof. G.K. Parks

Date: Sept-6/2000

Abstract

This thesis examines ion distributions and flows in the earth's magnetotail. Tailward flows in the current sheet region (CS) are usually associated with a neutral line. Another possible explanation for these tailward flows is provided through this work.

First, the meaning of ion flows is investigated in terms of aliasing problems. Data from the WIND satellite are used to demonstrate that velocity moments can be ambiguous when the distribution functions are computed with instrument sampling rates which are slow compared to the rate of change of the magnetic field. Next, ion distribution functions are generated using a test particle simulation in a newly developed magnetic field model. Constraints for the model include the unique ground based CANOPUS photometer array, which is used to demonstrate quantitatively how the crosstail current sheet thins during substorm growth phase. Such thinning corresponds to equatorward motion of auroral emissions, and earthward motion of the inner edge of the plasma sheet to distances inside $\sim 6 R_E$. Simultaneously the current sheet can thin from $2 R_E$ to $0.1 R_E$ and remain stable for tens of minutes.

Test particle simulations in the model plasma sheet boundary layer (PSBL) show that fast bulk ion flows are due to the presence of beams in the distribution functions. At the edge of the PSBL there are fast earthward beams. Closer to the CS bulk velocity slows and becomes tailwards due to counterstreaming beams. In the CS large populations of anti-earthward moving protons contribute to anisotropic tailward flows. The model thus predicts that tailward flows in the CS develop as a natural consequence of PSBL dynamics.

Finally, a first-order perturbation electrostatic field, derived from linear theory, is modelled to simulate noise in the PSBL. It is used to test and validate the previous

noise free test particle simulations. An assessment is made of the stability of the distribution functions to the model electrostatic noise in the PSBL. For electrostatic noise with realistic intensities, there is no significant change in the model distribution functions.

Dedication

To the glory of the Lord Jesus.

This most beautiful system of the sun, planets, and comets, could only proceed from the counsel and dominion of an intelligent and powerful Being. This Being governs all things, not as the soul of the world, but as Lord over all, and on account of His dominion He is wont to be called Lord God, Universal Ruler.

[Isaac Newton, *Philosophiae Naturalis Principia Mathematica*, 1686.]

Acknowledgements

I would like to thank my supervisors, Dr. Gordon Rostoker and Dr. Richard Sydora, for their support and help during the course of this research. Dr. Rostoker gave me a good grounding in space physics, and was always enthusiastic, providing encouragement and helpful advice. From him I learned a great deal about how to present my work. Also, thanks to him, I had the opportunity to meet my wife's family in Korea. Both my supervisors have supported my work, and provided numerous opportunities to present results at scientific meetings. I also extend thanks to the other members of my supervisory committee, Wojciech Rozmus, Helmy Sherif, Robert Fedosejevs, as well as my external examiner George Parks, for their careful examination of my thesis and their useful comments.

The CANOPUS and WIND teams of principle investigators, researchers, and technicians have done an exceptional job of making these missions a reality. My thanks go to the Bob Lin for use of WIND data, and to John Samson and Gordon Rostoker for setting up an excellent environment at the University of Alberta where CANOPUS data may be accessed.

Everyone in the space physics group has contributed to this work in one way or another. Thanks to Hamid Al-Nashi, Karen Apps, Sherwood Botsford, Martin Connors, Peter Damiano, Sarah Derr, Peter Dobias, Erena Friedrich, Frances Fenrich, Przemek Frycz, William Liu, Jim Mackinnon, Robert Rankin, Wojciech Rozmus, Henry Sikkema, Vladimir Tichonchuk, and Igor Voronkov. I would like to give special thanks to Henry, for moral support, prayers and encouragement in more ways than can be counted; and to William and Vladimir, for helping me with many theoretical questions as well as William's lessons in table tennis. My friend Mark Wilber deserves special mention because without his help none of the analysis of the WIND data would

have been possible. I would like to thank Mark for reading numerous drafts of chapter 2, and for never losing patience at numerous requests for help. Lynn Chandler, the graduate student secretary at the University of Alberta, has been so helpful through these years. She has answered questions, provided encouragement, and all kinds of support and friendship. Thank you, Lynn.

One of the most important parts of my life here in Edmonton has been my relationship with the Presbyterian Reformed Church of Edmonton. Dr. Peter Heaton (Professor Emeritus in Medicine at the University of Alberta) is fondly remembered for his great Christian example. The effect he and his wife, Ann, have had on my life will continually reverberate.

My family have always supported my endeavours. Thanks to my father and mother, Alexander and Denise, for most of all providing a stable and loving home. My brother Kevin and sister Megan have always encouraged me and provided hours of fun. Dis lekker by die see!

My wife Seung-Hyun has been a great support, especially in times when I felt that all this effort was pure vanity. Her interest and encouragement helped more than she knows. Although it has been difficult for her to be the wife of a student, Seung-Hyun has come through this with me, and I thank her for being my helper and true daughter of Sarah.

Most of all, my eternal thanks are for the One who made me, gave me life, and allowed me to know Him.

Contents

Dedication

Abstract

Acknowledgements

Contents

List of Tables

List of Figures

List of Symbols

1	Introduction	1
1.1	The solar wind and the earth's magnetosphere	1
1.2	Magnetospheric energy storage and release	3
1.3	Ion flows in the mantle, lobe, PS, and PSBL	8
1.4	Motivation	12
2	Plasma Flows in the Magnetotail	15
2.1	Ion distributions and moment calculations	16
2.2	Limitations due to time averaging	20

2.3	Plasma flows from the WIND satellite	21
2.3.1	September 16, 1995	22
2.3.2	October 21, 1997	27
2.4	Conclusions	32
3	Test particle modelling technique	34
3.1	Test particle simulations	34
3.2	Ion distributions	35
3.2.1	Vlasov's equation	35
3.2.2	Liouville's theorem	38
3.2.3	Distribution function calculation	40
3.3	The plasma source	43
3.3.1	Plasma mantle source	43
3.3.2	Ionospheric source	44
3.3.3	Neutral sheet source	45
3.3.4	Lobe source	45
3.4	Examples of the modelling technique	46
3.4.1	Modified Harris sheet	47
3.4.2	Distribution function results	47
4	The magnetotail model	50

4.1	Introduction	50
4.2	Key factors in the magnetotail model	51
4.2.1	The dipole field	53
4.2.2	The equilibrium tail model	54
4.2.3	Weak field region	57
4.3	Constraining the magnetic field model	61
4.3.1	Constraint from the neutral sheet magnetic field	62
4.3.2	Constraint from proton precipitation	65
4.3.3	Constraint from T96	78
4.3.4	Constraint from the lobe magnetic field	82
4.4	Model electric field	82
4.4.1	Cross polar cap potential	88
4.4.2	E_x and E_z components	91
4.4.3	Curl time scale	94
5	Simulation of magnetotail ion distribution functions	97
5.1	Comparison with previous model results	98
5.2	A novel boundary condition	101
5.2.1	PSBL/mantle/lobe distributions	102
5.3	Ion distributions from 'zeroth order' test particle simulations	107

5.3.1	PSBL/CPS region	107
5.3.2	CS region	116
5.4	Model of electrostatic noise	125
5.4.1	Solution of the electrostatic dispersion relation	127
5.4.2	Electrostatic noise spectrum	133
5.5	Ion distributions from 'first order' test particle simulations	135
5.5.1	PSBL/CPS region	136
5.5.2	CS region	136
5.6	Summary	141
6	Concluding remarks	142
6.1	Summary of results	142
6.1.1	Plasma flows in the magnetotail	142
6.1.2	Magnetic field model development	143
6.1.3	Test particle simulations	144
6.2	Future work	145
	Bibliography	147

List of Tables

1	CANOPUS instrument sites. See <i>Baker and Wing</i> [1989] for a description of the eccentric PACE invariant coordinates.	5
1	Final magnetic field model parameters.	79

List of Figures

- 1.1 A schematic portraying a generally accepted global representation of the earth's magnetosphere (after *Williams et al.* [1992]). 3
- 1.2 (a.) Meridian scanning photometer data (486.1 nm) from RANK and GILL stations in the CANOPUS array showing auroral luminosity during a substorm growth phase and subsequent expansive phase on March 9, 1995. Local magnetic time is approximately UT minus 6 hours, (b.) Magnetic X-component from the Churchill line of magnetometers, (c.) Pi2 pulsations from the Gillam magnetometer. Table 1 gives the location of the various stations in the CANOPUS array. 6
- 2.1 A schematic portraying (top two rows), from left to right, ion distribution functions in velocity space at different times. The third row shows the moments (density and velocity) calculated from the distribution functions. 18
- 2.2 A schematic portraying (top two rows), from left to right, ion distribution functions in velocity space at different times. The third row shows that the moments (density and velocity) calculated from the distributions are identical to those shown in the previous figure. 19

2.3	Magnetic field and velocity moments on September 16, 1995 from 2330-2345 UT. The top three panels show the magnetic field. The light solid, dot-dash, and dark solid curves are, respectively, the 3 second, 48 second, and 96 second averaged magnetic field in GSE coordinates. The bottom three panels are the velocity moments. The dot-dash and solid curves are, respectively, calculated from the 48 and 96 second distribution functions.	23
2.4	Velocity moments on September 16, 1995 from 2330-2345 UT. The top two panels show the velocity in directions parallel and perpendicular to the magnetic field. The dot-dash and solid curves are, respectively, calculated from the 48 and 96 second distribution functions. The bottom three panels show the projections of the perpendicular velocity into the GSE plane.	24
2.5	Ion distribution functions in velocity space on September 16, 1995. All four velocity distribution functions are consecutively measured using a 48-s integration period. Each panel shows logarithmically spaced isocontours of ion phase space density in $(V_{\parallel}, V_{\perp})$ -space. Negative V_{\perp} points correspond to particles with velocities having $V_{\perp} \cdot U_{\perp} < 0$; where U_{\perp} is the component of the bulk flow velocity perpendicular to the magnetic field vector. Concentric dashed circles indicate total velocities of 1000 and 2000 km/s. The UT time about which the data are centred is shown below each distribution function. Bulk velocity moments and average magnetic field, in GSE-coordinates, are shown on each plot. .	25

2.6	Magnetic field and velocity moments on October 21, 1997 from 1340-1355 UT. The top three panels show the magnetic field. The light solid, dot-dash, and dark solid curves are, respectively, the 3 second, 48 second, and 96 second averaged magnetic field in GSE coordinates. The bottom three panels are the velocity moments. The dot-dash and solid curves are, respectively, calculated from the 48 and 96 second distribution functions.	28
2.7	Velocity moments on October 21, 1997 from 1340-1355 UT. The top two panels show the components of velocity in directions parallel and perpendicular to the magnetic field. The dot-dash and solid curves are, respectively, calculated from the 48 and 96 second distribution functions. The bottom three panels show the projections of the perpendicular velocity into the GSE plane.	29
2.8	Ion distribution functions in velocity space on October 21, 1997. All four velocity distribution functions are consecutively measured using 48-s integration period. Each panel shows logarithmically spaced isocontours of ion phase space density in $(V_{ }, V_{\perp})$ -space. Negative V_{\perp} points correspond to particles with velocities having $V_{\perp} \cdot U_{\perp} < 0$; where U_{\perp} is the component of the bulk flow velocity perpendicular to the magnetic field vector. Concentric dashed circles indicate total velocities of 1000 and 2000 km/s. The time about which the data are centred is shown below each distribution function. Bulk velocity moments and average magnetic field, in GSE-coordinates, are shown on each plot.	30

3.1	Conservation of particles and momentum in the absence of collisions is applied to a finite volume in phase space. Trajectories in phase space are labelled with arrows in the direction from the volume V_0 to the volume V . Each trajectory corresponds to a line of constant phase space density.	37
3.2	(a.) The cartoon illustrates how pseudo-particles, with initial position and velocity (r, v_i) move through space to a source region. (b.) The upper distribution function shows contours of constant phase space density. Numerous pseudo-particles are followed from unique initial locations in velocity space (lower distribution) to the source (upper distribution). Since the velocity distribution is known at the source, Liouville's theorem allows each initial pseudo-particle to be tagged with a known phase space density.	41
3.3	Model ion velocity distribution functions in the $V_B - V_C$ plane, and at the $V_E = 0$ cut. Velocities are in thousands of km/s . The contours are in intervals of $10^{-0.5}$ from $10^{-17.5} s^3/m^6$. (a.) This calculation is for $z = L_z$; (b) for $z = 0.5L_z$; (c) an example of a singular case of a proton's orbit when it is trapped in the current sheet and never reaches the source. These kinds of orbits comprise the phase space gaps found in (a) and have a figure eight shape; and (d) a typical Speiser orbit for a proton that forms part of the field-aligned beam at the edge of the current sheet.	48
4.1	Contour plot in the noon-midnight meridian showing values of the crosstail electric current density, J_y^{Tail} in units of nA/m^2 . This azimuthal current is positive in the westward direction (dawn-to-dusk).	55

4.2	Vectors in the equatorial plane showing the variation of the crosstail electric current density for the model WFR.	59
4.3	Vectors at $X=-9 R_E$ (top) and $X=-13 R_E$ (bottom) showing the variation of the crosstail electric current density for the WFR.	60
4.4	Model magnetic field values in the neutral sheet compared to various satellite measurements. The dotted line indicates the model magnetic field, the solid line is the empirical function of <i>Rostoker and Skone</i> [1993], calculated irrespective of substorm phase. The circles and triangles indicate B_z during disturbed and quiet periods from the measurements of <i>Nakai et al.</i> [1997]. The squares are the values from <i>Lui et al.</i> [1992], measured just prior to the onset of magnetic field dipolarisation, the single star is for the growth phase measurements at $X=-11 R_E$ by <i>Sergeev et al.</i> [1993].	63
4.5	Model magnetic field lines in the noon-midnight meridian for current sheet half-thickness (a.) $L_z = 1R_E$ and (b.) $L_z = 0.05R_E$. In the latter case the thinner current sheet is evidenced by the decreased magnetic field line radius of curvature.	67
4.6	Model predictions for the regions of proton precipitation in the ionosphere. Precipitation is assumed to occur in the region between the high- and low-latitude borders. The ordinate is invariant latitude in degrees, and the abscissa is the model current sheet half-thickness, normalised to $L_{min} = 0.05 R_E$. These curves were computed by calculating the regions in the magnetotail where 10, 20, and 30 keV protons achieve $1 \leq \kappa \leq 3$, and then mapping these regions to the ionosphere. The parameter κ is defined in Equation 4.4.3.14.	68

4.7	(a.) Meridian scanning photometer data (486.1 nm) from RANK and GILL in the CANOPUS array showing the growth phase and intensification of a substorm event on March 9, 1995. AACGM coordinates are explained by <i>Baker and Wing</i> [1989]. (b.) Magnetic X-component from the Churchill line of magnetometers, (c.) Magnetic X-component Pi2 pulsations at GILL. Local magnetic time is approximately UT minus 6 hours for the Churchill line.	72
4.8	(a.) March 9, 1995 H_{β} emission boundaries are shown by the solid line, with error bars. The best fit values, calculated from the magnetic model predicted precipitation regions, are shown as circles. (b.) Model predictions for the current sheet thickness at $8 R_E$ (left ordinate), and plasma sheet inner edge position (right ordinate).	73
4.9	(a.) Meridian scanning photometer data (486.1 nm) from RANK and GILL in the CANOPUS array showing the growth phase and intensification of a substorm event on February 9, 1995. AACGM coordinates are explained by <i>Baker and Wing</i> [1989]. (b.) Magnetic X-component from the Churchill line of magnetometers, (c.) Magnetic X-component Pi2 pulsations at BACK. Local magnetic time is approximately UT minus 6 hours for the Churchill line.	75
4.10	(a.) February 9, 1995 H_{β} emission boundaries are shown by the solid line, with error bars. The best fit values, calculated from the magnetic model predicted precipitation regions, are shown as circles. (b.) Model predictions for the current sheet thickness at $8 R_E$ (left ordinate), and plasma sheet inner edge position (right ordinate).	76

4.11	Components of the magnetic field plotted as a function of distance from the neutral sheet Z , calculated at $X=-15 R_E$ and $Y=0$. The new model is the dashed and T96 is the solid curve. Parameters for T96 are $P_{DYN}=1$ nPa, $DST=-40$, $B_Y^{IMF}=0$, $B_Z^{IMF}=-1$, $TILT=0^\circ$	80
4.12	Components of the magnetic field plotted as a function of distance from the neutral sheet Z , calculated at $X=-15 R_E$ and $Y=2$. The new model is the dashed and T96 is the solid curve. Parameters for T96 are $P_{DYN}=1$ nPa, $DST=-40$, $B_Y^{IMF}=0$, $B_Z^{IMF}=-1$, $TILT=0^\circ$	81
4.13	Comparison of the model magnetic streamlines to the empirical T96 model. (a.) T96 model with $P_{DYN}=1$ nPa, $DST=-40$, $B_Y^{IMF}=0$, $B_Z^{IMF}=-1$, $TILT=0^\circ$ and (b.) the new model.	83
4.14	T96 model with $P_{DYN}=1$ nPa, $DST=-40$, $B_Y^{IMF}=0$, $B_Z^{IMF}=-1$, $TILT=0^\circ$. Contours of constant (a.) B_x (nT), (b.) B_z (nT), (c.) $J_y(nA/m^2)$ in the noon-midnight meridian.	84
4.15	Contours of constant (a.) B_x (nT), (b.) B_z (nT), (c.) $J_y(nA/m^2)$ for the new magnetic field model, plotted in the noon-midnight meridian.	85
4.16	Lobe field strength for the new model (solid curve), calculated at $(Y, Z) = (0, 10) R_E$, is compared with the empirical functions of <i>Slavin et al.</i> [1985] (dot-dash curve) and <i>Nakai et al.</i> [1991] (dashed curve).	86

4.17	Superposed epoch analysis of polar cap potential drop and IMF B_z for various activity levels as quantified by the AE index (after <i>Weimer et al.</i> [1992]). The onset of substorm expansive phase is identified as $t = 0$. The solid circles show measured potential differences, obtained from an integration of the electric field. The error bars show the integration errors associated with the electric field uncertainty of 2 mV/m. The lines extending upward from the circles end at the "corrected potential", which is an estimate of what the true potential drop may have been, based on the magnetic local times at the reversals, as discussed in <i>Weimer et al.</i> [1992].	90
4.18	Contour plots of $\log_{10}(L_g)$ where L_g (in R_E) is the gradient scale length defined in Equation 4.4.4.24. The contours are in the $X - Y$ plane at $Z=0 R_E$ (top) and $Z=0.1 R_E$ (bottom).	93
4.19	Contour plot of $\log_{10}(T/t_{curt})$ defined in Equation 4.4.4.27. The top figure shows contours in the $X - Y$ plane at $Z=0 R_E$. The bottom figure is for data computed in the $X - Y$ plane at $Z=0.1 R_E$	96
5.1	Model ion two-dimensional velocity space distributions at four locations in the PSBL, $Z=2.4, 2.0, 1.0,$ and $0.1 R_E$, all at $X=-15 R_E$. The parallel velocity is in the earthward direction. The closely spaced contours centred at zero speed correspond to the cool lobe plasma. The higher speed particles correspond to the hot central plasma sheet particles which have entered the boundary layer with initially most of their energy in parallel motion. Two contours per decade are shown, with the lowest value being at $-17.5 s^3/m^6$	100

5.2	A schematic diagram showing the model boundary, which is the magnetic field line which crosses the NS at $X=-100 R_E$ (solid line). The probability of observing mantle/PSBL plasma increases/decreases with distance downtail. Model velocity distribution functions at various positions along the boundary are shown as line drawings with the ordinate corresponding to phase space density and the abscissa to the earthward velocity, V_x	103
5.3	Model variables against downtail position for (top) the perpendicular temperature (T_\perp), (middle) number density (n), and (bottom) velocity (V_b) are shown for the core term (solid curves) and the beam term (dashed curves).	105
5.4	Two-dimensional cuts in the $V_{\parallel} - V_\perp$ plane of the model boundary condition (BC) distribution functions at different downtail positions for positive Z . The V_{\parallel} direction is earthwards. In the near-earth region the distributions are representative of the outer edge of the PSBL. In the midtail region the distributions are representative of an intermediate region including lobe-mantle plasma. The distant tail is representative of an almost pure mantle BC. The contours of constant phase space density are plotted every two decades from -23 to $-10 s^3/m^6$	106
5.5	Model ion velocity distributions shown as (left column) two-dimensional distributions in the V_B-V_C plane, and (right column) cuts in the V_B direction ($V_C=0$) at four locations in the noon-midnight meridian, (a.) $Z=3.2$, (b.) 2.25, (c.) 0.75, and (d.) $0.3 R_E$, all at $X=-20 R_E$	108

- 5.6 Two dimensional cuts through model distribution functions calculated at $X=-20 R_E$ and (left column) $Z=3.5 R_E$ and (right column) $Z=0.75 R_E$. The velocities are expressed in terms of the direction of the magnetic field (V_B), electric field (V_E), and convection (V_C). The top row shows the cut in the $V_B - V_C$ plane, the middle row shows the cut in the $V_B - V_E$ plane, and the bottom row is the cut in the $V_C - V_E$ plane. . 109
- 5.7 (Top) Model two-dimensional ion velocity distribution in the $V_B - V_C$ plane, calculated at $(X, Y, Z) = (-20, 0, 1) R_E$. Several initial positions in velocity space are selected in order to demonstrate the representative behaviour of particles comprising the core and beam components of the distribution. The particles comprising part of the earthward moving beam are labelled with crosses and points A1, A2. The sample particle orbits from the core component are labelled as circles and B1, B2. For the counterstreaming component the labels are squares and C1, C2, C3. The lower figure shows the trajectory traces corresponding to the initial conditions chosen in the upper figure. Arrows show the direction of particle motion. 112
- 5.8 Model (top) number density and (bottom) velocity moments calculated at various Z -distances from the NS at $X=-20 R_E$. The velocities are expressed in terms of the directions of the magnetic field (V_B), electric field (V_E) and convection (V_C). 115
- 5.9 Model ion velocity distributions distributions shown as two-dimensional distributions in the V_B-V_C plane. The distribution functions are plotted for different downtail positions, from $X = -20 R_E$ to $-75 R_E$. The X -positions are indicated in each subplot. 117

5.10 (Top) Model two-dimensional ion velocity distribution in the $V_B - V_C$ plane, calculated at $(X, Y, Z) = (-24, 0, 0.0001) R_E$. At this location $V_B \approx V_z$ and $V_C \approx -V_x$. Several initial positions in velocity space are selected in order to demonstrate the representative behaviour of particles comprising the different components of the distribution function. Particles from the convective phase space density enhancements (CPSDE), are labelled 1-4. The CPSDE at negative/positive V_B is formed from mirrored ion beams that initially come from the northern/southern hemisphere. The phase space density of the negative V_B CPSDE is slightly higher than its $+V_B$ counterstreaming counterpart. The lower figure shows the trajectory traces corresponding to the initial conditions chosen in the upper figure. Arrows show the direction of particle motion. 118

5.11 The trajectory of a particle in the $X - Z$ plane is shown (left ordinate, solid line) as a reference against which to compare the variation of the magnetic moment (μ) which is the dashed-dot line and right ordinate. The magnetic moment is normalised. The particle comes from the model boundary in the southern hemisphere, and arrives at the observation location at $(X, Z) = (-24, 0.0001) R_E$ with a velocity $(V_B, V_C, V_E) = (500, -1060, 0) \text{ km/s}$ 120

- 5.12 Two dimensional cuts of the model velocity distribution calculated at $(X, Z) = (-22, 0.0001) R_E$. The velocities are expressed in terms of the directions of the magnetic field (V_B), electric field (V_E) and convection velocity(V_C). The top row shows cuts in the $V_B - V_C$ plane at $V_E = 0km/s$ (left) and $200km/s$ (right). The middle row shows cuts in the $V_B - V_E$ plane at $V_C = 0km/s$ (left) and $200km/s$ (right). The bottom row shows cuts in the $V_C - V_E$ plane at $V_B = 0km/s$ (left) and $200km/s$ (right). At this location $V_C \approx V_x, V_B \approx V_z, V_E \approx V_y$ 121
- 5.13 Model (top) density and (bottom) velocity moments calculated in the magnetotail CS region ($Z = 0.0001 R_E$) in the noon-midnight meridian. The velocities are expressed in terms of the directions of the magnetic field (V_B), electric field (V_E) and convection velocity(V_C). At these locations in the CS region $V_C \approx V_x, V_B \approx V_z, V_E \approx V_y$ 122
- 5.14 Model velocity moments in the $V_C (\approx V_x)$ direction calculated in the magnetotail CS region ($Z = 0.0001 R_E$). The moments are shown for three different current sheet half-thickness parameters ($L_z = 1, 11, 19$). L_z has been normalised to the model value selected in the previous chapter, viz. $L_z = 1 \equiv 0.05 R_E$ 124

- 5.15 Solutions to the kinetic dispersion relation in the simple plasma model for (a.) $n_b/n_e=0.8$, (b.) 0.7., (c.) 0.2. For both (a.) and (b.) $T_i/T_e = 0.09$; $T_i = T_b$; $T_e=500$ eV. These temperatures and densities correspond approximately to the situation at $X=-21 R_E$ ($V_b \sim 12V_{thi}$) and $X=-34 R_E$ ($V_b \sim 10V_{thi}$), respectively, along the model boundary. For (c.) $T_e/T_i=2$ and $T_b/T_i=0.05$. This corresponds to the situation at $X=-85 R_E$ ($V_b \sim 2.5V_{thi}$). The upper panels show the normalised frequency at peak growth versus normalised beam drift speed. The middle panels show the normalised peak growth, and the bottom panels show the wavenumber at peak growth. 131
- 5.16 (a.) Growth rate γ versus ω_r as a function of downtail distance. The position of the maximum growth rate is indicated by the circle markers. (b.) Maximum growth rate, γ , as a function of downtail distance, X , and the corresponding real frequency, ω_r , all normalised to the electron plasma frequency ω_{pe} . The vertical line separates the regions where the instability is dominated by the ion-ion or ion-electron acoustic modes. 132
- 5.17 Two-dimensional cuts of the distribution function calculated in the noon-midnight meridian and at $(X,Z)=(-20,1) R_E$. The parameter A_o refers to the electric field intensity normalised to 5 mV/m, and varies from (a.) 1 to (f.) 40. A Gaussian electrostatic spectrum was used for this case. 137
- 5.18 Two-dimensional cuts of the distribution function calculated in the noon-midnight meridian and at $(X,Z)=(-20,1) R_E$. The parameter A_o refers to the electric field intensity normalised to 5 mV/m, and varies from (a.) 1 to (f.) 40. A white electrostatic spectrum was used for this case. 138

5.19	Two-dimensional cuts of the distribution function calculated in the noon-midnight meridian and at $(X,Z)=(-26,0.0001) R_E$. The parameter A_0 refers to the electric field intensity normalised to 5 mV/m, and varies from (a.) 1 to (f.) 40. A Gaussian electrostatic spectrum was used for this case.	139
5.20	Two-dimensional cuts of the distribution function calculated in the noon-midnight meridian and at $(X,Z)=(-26,0.0001) R_E$. The parameter A_0 refers to the electric field intensity normalised to 5 mV/m, and varies from (a.) 1 to (f.) 40. A white electrostatic spectrum was used for this case.	140

List of Symbols and Abbreviations

\vec{B}	Magnetic field
B_0	Lobe magnetic field
B_n	Normal magnetic field
B_p	WFR magnetic field
CANOPUS	Canadian Auroral Network for the OPEN Program Unified Study
C_{ia}	Sound speed
CPS	Central plasma sheet
CPSDE	Convective phase space density enhancements
CS	Current sheet
DST	Worldwide magnetic storm time disturbance index
\vec{E}	Electric field
f	Phase space density
GSE	Geocentric solar ecliptic coordinate system
H_β	486.1 nm auroral optical emissions
IMF	Interplanetary magnetic field
ISEE	ISEE spacecraft
\vec{k}	Wavenumber
k_B	Boltzmann constant
K_p	Geomagnetic disturbance index
L_0	Decay length scale
L_g	Gradient length scale
L_y	WFR azimuthal length scale
L_z	Crosstail current sheet half-thickness
m	Mass

MHD	Magnetohydrodynamics
MSP	Meridian scanning photometer
n	Number density
n_b	Ion beam number density
n_e	Electron number density
n_i	Ion core number density
NENL	Near-earth neutral line
NS	Neutral sheet
PS	Plasma sheet
PSBL	Plasma sheet boundary layer
q	Charge
R	Magnetic field radius of curvature
R_E	Earth radius
t_{curl}	Curl time scale
T_b	Ion beam temperature
T_e	Electron temperature
T_i	Ion core temperature
T96	<i>Tsyganenko</i> [1996] magnetic field model
$T_{ }$	Beam temperature parallel to the magnetic field direction
T_{\perp}	Beam temperature perpendicular to the magnetic field direction
ULF	Ultra low frequency
UT	Universal time
V_A	Alfven speed
V_b	Beam speed
V_B	Velocity in the magnetic field direction
V_C	Velocity in the convection direction

V_E	Velocity in the electric field direction
V_g	Group velocity
$V_{ }$	Velocity parallel to the magnetic field
V_{\perp}	Velocity perpendicular to the magnetic field
V_{thi}	Ion thermal velocity
$V_{th }$	Thermal velocity along magnetic field direction
VDF	Velocity distribution function
WFR	Weak magnetic field region
WIND	WIND spacecraft
Z	Plasma dispersion function
α	Electric field scaling parameter
δ_k	Random phase factor
γ	Imaginary part of dispersion solution
λ_{σ}	Debye length
μ_0	Permeability of free space
ϕ	Electric potential
ρ_m	Mass density
τ	Decay time scale
ω_k	Plasma dispersion
ω_{pb}	Ion beam plasma frequency
ω_{pe}	Electron plasma frequency
ω_{pi}	Ion core plasma frequency
ω_r	Real part of dispersion solution
ζ_{σ}	Argument for the plasma dispersion function

CHAPTER 1

Introduction

1.1 The solar wind and the earth's magnetosphere

The most dramatic influence of the sun upon our terrestrial environment is related to weather patterns, and is the subject of age-old studies. More recently scientists have studied the influence of the sun on the earth's magnetic environment. Dynamic changes in the earth's magnetic field are intimately related to the continuous buffeting it experiences from the solar wind, a gusty flow of plasma from the sun. The solar wind is a nearly fully ionised gas which, at the earth, has a typical density of $2\text{-}10\text{ cm}^{-3}$, and velocity about 400 km/s . Since the solar wind exceeds the sound speed ($\sim 100\text{ km/s}$) and the Alfvén speed ($\sim 40\text{ km/s}$), the earth's motion, in the frame of the solar wind, is supersonic and super Alfvénic. Thus a magnetohydrodynamic (MHD) shock wave, called the bow shock, forms in front of the earth. The process of mass, momentum, and energy transport from the solar wind, and the interplanetary magnetic field (IMF) it carries along, modifies the dipolar geometry of the earth's magnetic field. On the dayside, the earth's magnetic field is compressed, while on the nightside it stretches away from the earth, forming a long cylindrical cavity called the magnetotail. The magnetotail is a very important component of the magnetosphere, for it acts as a dynamic reservoir of plasma and energy. A boundary, known as the magnetopause, marks the separation of the solar wind from the earth's magnetic field. The magnetopause is defined primarily by a large scale electric current – the

magnetopause current – that is induced by the plasma-magnetic field interaction. The region which it confines is called the magnetosphere. The region between the bow shock and the magnetopause is called the magnetosheath. These and other major plasma regimes are illustrated schematically in Figure 1.1.

In addition to the magnetopause current, another current system is required to maintain the tail-like geometry in the anti-sunward direction. This sheet-like current is known as the crosstail current. It is located in the current sheet (CS) region, whose midplane is called the neutral sheet (NS), and flows from the dawn flank to the dusk flank. In order to carry the electric current, the plasma has relatively high density ($\sim 0.1 \text{ cm}^{-3}$) and temperature (several keV) around the NS. This region around the NS is called the plasma sheet (PS). In this schematic picture, the crosstail current forms the central core of the PS. Both the northern and southern regions of the PS, in their high latitude locations, are adjacent to regions of strong magnetic field called the magnetotail lobes. The lobes are connected magnetically to the northern and southern polar regions of the earth, and have a low plasma population with number densities often less than 0.01 cm^{-3} .

The plasma sheet boundary layer (PSBL) is a region distinct from the central plasma sheet (CPS) and an important region of plasma transport in the tail. At its low latitude interface the PSBL borders the CPS, and it borders the lobe at its high latitude interface. Far from the earth its high latitude interface can be immediately adjacent to the plasma mantle. The PSBL features particle densities in the range of 0.1 to 1.0 cm^{-3} . One of the main characteristics of the PSBL is the earthward flowing and counterstreaming field-aligned ion beams [*De Coster and Frank, 1979; Williams, 1981; Eastman et al., 1984*]. The conventional picture is that at the outermost edge of the PSBL one finds high speed electrons. Moving further into the boundary layer earthward streaming ion beams are encountered, followed by

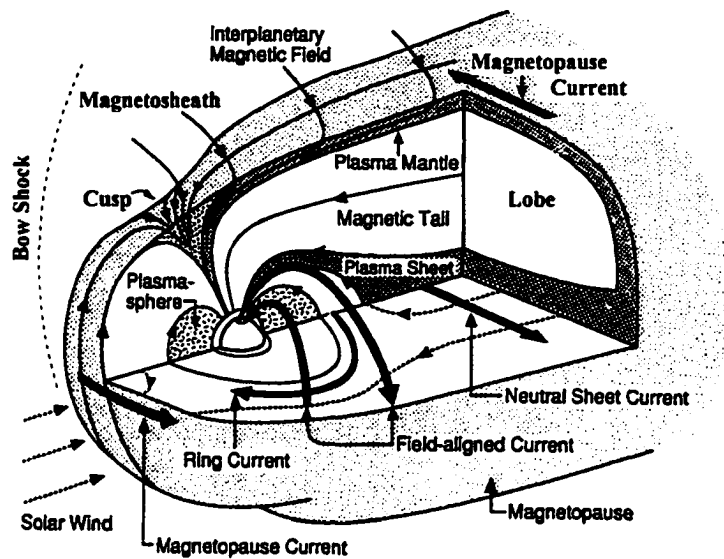


Figure 1.1: A schematic portraying a generally accepted global representation of the earth's magnetosphere (after *Williams et al.* [1992]).

counterstreaming earthward and tailward beams, and finally an evolution to a nearly isotropic CPS ion distribution. Recent observations of single tailward ion beams [*Parks et al.*, 1998], indicate, however, that the picture is sometimes more complicated. The PSBL and CS regions are among the most important in the magnetotail because microscale phenomena occurring there can be important to the system as a whole.

1.2 Magnetospheric energy storage and release

Dungey [1961] was the first to suggest that high density plasmas in the solar wind can enter the magnetosphere by magnetic field reconnection at the dayside magnetopause when the IMF is southward (opposite to the geomagnetic field direction). This produces an open magnetosphere with magnetic merging on the dayside and reconnection on the nightside. At such times solar wind mass, energy, and momentum

can directly enter the magnetosphere and energy can be stored in the magnetic field of the tail lobes and other regions of the magnetotail. While the IMF is southward the magnetosphere has some field lines that are called *open* because there is only one footpoint in the ionosphere, the other being in the sun. The footpoint located in the sun is carried tailwards by the solar wind under the frozen in condition of MHD. The combined effect of the tailward motion and convection, resulting from the action of the crosstail convection electric field, causes open field lines to eventually reconnect in the earth's magnetotail. The inner magnetosphere contains *closed* field lines with footpoints in the earth's southern and northern hemispheres, respectively. Some components of the solar wind are transported along the reconnected field lines down to the ionosphere. This ionospheric region is known as the cusp.

Since the magnetotail behaves like a reservoir of energy, at some point the stresses that cause its magnetic field lines to stretch away from the earth can no longer be maintained. The magnetotail will reach a state where it must release some energy, in the process undergoing a transition to a more relaxed state. Much of this energy is released into the inner magnetosphere impulsively during magnetically disturbed intervals called magnetospheric substorms. During substorms large amounts of energy are slowly stored and then suddenly released in the magnetosphere, the effects of which may be observed from the surface of the earth, as bright, often fast moving aurora, and large magnetic perturbations.

Observationally, the magnetospheric substorm can be described in terms of *directly driven* and *storage release* processes [Rostoker et al., 1987]. Energy storage occurs during the directly driven stage, which usually starts when the IMF turns southward. Subsequent enhancement of magnetospheric convection causes plasma from the magnetotail to move closer to the earth. Some of the magnetotail particles

are accelerated at this time and a small number of particles near the loss cone precipitate into the ionosphere. Precipitation enhances ionospheric conductivity, which permits more current to flow between the ionosphere and the magnetosphere. The directly driven process is characterised by the increase of the large scale ionospheric current systems, known as the westward and eastward ionospheric electrojets. This episode of energy storage in the magnetosphere is called the *growth phase* of the magnetospheric substorm. The enhancement of the directly driven electrojets is associated with increased magnetic perturbations that are observed on the ground. As well, during the growth phase the auroral luminosity increases and can be observed by ground-based instruments such as photometers. Figure 1.2 shows an example of magnetometer and photometer data during a magnetospheric substorm on March 9, 1995. Figure 1.2a shows the photometer data for the 486.1 *nm* wavelength at the Gillam and Rankin Inlet stations of the CANOPUS array. Figure 1.2b shows the X-component of the magnetic perturbations at various stations, and Figure 1.2c shows the impulsive ULF magnetic perturbations, known as Pi2's, detected at Gillam. CANOPUS station locations are indicated in Table 1.

Location	Station acronym	Geographic Lat. Long.	PACE Lat. Long.
Eskimo Point	ESKI	61.1 266.0	71.93 -31.75
Ft Churchill	FCHU	58.8 265.9	69.72 -30.76
Gillam	GILL	56.4 265.4	67.38 -30.93
Island Lake	ISLL	53.9 265.3	64.94 -30.33
Pinawa	PINA	50.2 264.0	61.16 -31.58
Rankin Inlet	RANK	62.8 267.9	73.72 -28.97
Taloyoak	TALO	69.5 266.5	79.65 -36.38

Table 1: CANOPUS instrument sites. See *Baker and Wing [1989]* for a description of the eccentric PACE invariant coordinates.

For this substorm event the growth phase commenced between 0325-0335 UT

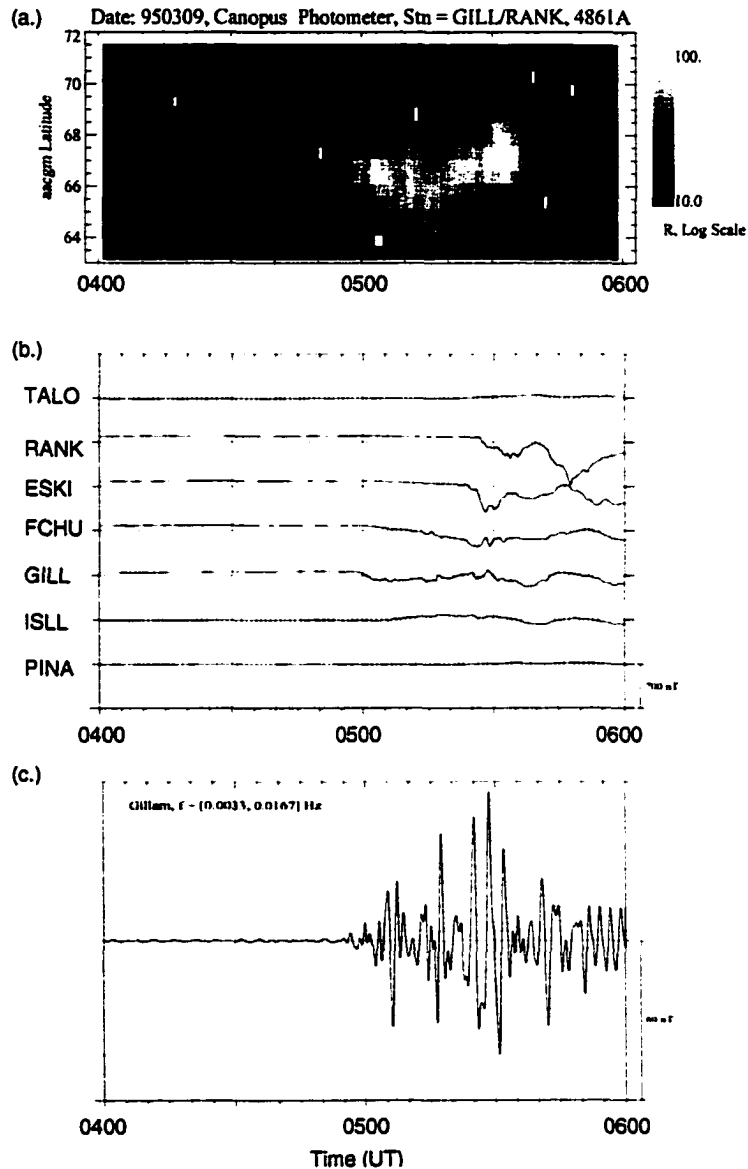


Figure 1.2: (a.) Meridian scanning photometer data (486.1 nm) from RANK and GILL stations in the CANOPUS array showing auroral luminosity during a substorm growth phase and subsequent expansive phase on March 9, 1995. Local magnetic time is approximately UT minus 6 hours, (b.) Magnetic X-component from the Churchill line of magnetometers, (c.) Pi2 pulsations from the Gillam magnetometer. Table 1 gives the location of the various stations in the CANOPUS array.

(not shown). Subsequent motion of the region of luminosity was equatorward (Figure 1.2a), and the eastward electrojet began to strengthen as signalled by a positive X-component magnetic perturbation (not shown). Distinct signatures of highly taillike magnetic fields are observed close to the earth (i.e. within geosynchronous orbit) during most growth phases, and in chapter 4 it is demonstrated that the growth phase stretching of magnetic field lines is associated with this equatorward motion of luminosity.

As energy from the solar wind is stored in the magnetic field of the lobe during the growth phase, lobe magnetic pressure is transmitted to the plasma sheet causing it to thin. Since the solar wind is, in effect, pulling the magnetotail and its contents antisunward, to maintain an equilibrium there must be some sort of reaction. This reaction is accomplished by the crosstail current thinning, intensifying, and moving closer to the earth. During the growth phase the near-earth crosstail current can thin to fractions of an earth radius (R_E) [Sergeev *et al.*, 1993; Sanny *et al.*, 1994; Kubyshkina *et al.*, 1999]. Simultaneously the crosstail current intensifies in the near-earth region [Kaufmann, 1987; Pulkkinen *et al.*, 1994]. The current intensification is restricted in radial extent, and azimuthally to within a few hours around magnetic midnight [Baker and McPherron, 1990; Iijima *et al.*, 1993; Baker *et al.*, 1993]. These changes in the crosstail current result in the magnetic field becoming very taillike in the PS [Kokubun and McPherron, 1981; Pulkkinen *et al.*, 1992; Nakai *et al.*, 1997]. and lead to a localised region of weak magnetic field in the NS.

Immediately following the growth phase (storage process) comes the release of energy during the substorm *expansive* and *recovery* phase. The expansive phase is signalled by the collapse of the near-earth crosstail current and the generation of ULF Pi2 pulsations as detected by ground magnetometers. Photometer data show an explosive brightening and poleward expansion of the region of discrete aurora.

In the example shown (Figure 1.2) expansive phase onset occurs at 0459 UT. Onset is clearest in the X-component at Gillam (GILL in Figure 1.2b and Pi2 pulsations in Figure 1.2c). The taillike magnetic field dipolarises at this time, and turbulent magnetic fields and fast flows of plasma are often seen in the magnetotail during this phase of the substorm. A long standing issue in substorm physics is that of where and when an internal magnetospheric process suddenly initiates to dissipate the stored tail energy at expansive phase onset. The most popular idea is that of the near-earth neutral line (NENL) model [McPherron *et al.*, 1973; Hones, 1979; Baker *et al.*, 1999] which posits an X-type magnetic reconnection region in the magnetotail causes expansive phase onset. The recovery phase is the final stage of the magnetospheric substorm. It follows the intense auroral displays associated with the expansive phase. During this interval the aurora in the midnight sector become weaker and quite diffuse. The magnetosphere is then effectively in a ground state, and if conditions are suitable, another substorm cycle may occur.

1.3 Ion flows in the mantle, lobe, PS, and PSBL

Injection of magnetosheath plasma into the cusp regions during the frontside magnetic field merging is followed by the convection of these high density plasmas from the dayside toward the centre of the magnetotail via the high-altitude polar cap regions (mantle). Rosenbauer *et al.* [1975] reported the existence of the tailward (100-200 km/s) mantle flows up to 18 R_E downtail. Hardy *et al.* [1979] extended the region of mantle observations to about 60 R_E , and the recent Geotail satellite mission was used by Eastman *et al.* [1998] to demonstrate its existence to 210 R_E . They found that plasma mantle intervals increase in probability of occurrence from 18% near the earth to about 50% near 205 R_E . Liu and Hill [1990] demonstrated theoretically that

the mantle becomes an especially important source of PS plasma during the substorm growth phase, when the IMF has a southward component for prolonged intervals.

When the mantle/lobe plasmas convect to the PS, they are considered to undergo some acceleration and heating processes (from several eV to several keV). Theoretical and numerical studies have been performed in order to understand these processes, particularly within the PSBL [Grabbe and Eastman, 1984; Schriver and Ashour-Abdalla, 1990]. The PSBL has been identified by the presence of ion beams [DeCoster and Frank, 1979; Sarris and Azford, 1979; Williams, 1981; Forbes et al., 1981; Eastman et al., 1984, 1985, 1986; Takahashi and Hones, 1988]. Typically, only earthward directed beams are present near the lobeward edge of the PSBL and tailward directed beams are present deeper within the layer. When counterstreaming beams are simultaneously observed, the tailward beam has a higher speed than the earthward beam [Forbes et al., 1981; Takahashi and Hones, 1988]. Several models attempt to explain the ion flows in the PSBL. Speiser [1965, 1967] proposed that the energisation mechanism is acceleration of CPS ions in the crosstail current sheet. Ions energised in the current sheet would stream earthward along the magnetic field in the PSBL, accounting for the earthward directed beams. The tailward beams would result from the mirroring of the earthward beams near the earth [Forbes et al., 1981]. Lyons and Speiser [1982] showed observational evidence supporting the Speiser model. They found that the cause of ion acceleration is the violation of the guiding centre approximation in the CS region, by which ions can gain their energies from the dawn-to-dusk electric field. This model has been pursued by several researchers (e.g. Speiser and Lyons, 1984; Ashour-Abdalla et al., 1991). Onsager et al. [1991] put forward another model of the formation of the PSBL which relies on a steady source of plasma from a spatially extended PS, together with steady equatorward and earthward $\vec{E} \times \vec{B}$ convection of the field lines due to reconnection at a neutral line.

Several researchers have used this model (e.g. *Frank et al.*, 1994; *Elphic et al.*, 1995; *Smets et al.*, 1998). At present the acceleration mechanism continues to be a source of debate [*Parks et al.*, 1998, 1999; *Fuselier and Onsager*, 1999; *Lui et al.*, 2000].

As mentioned previously, the PSBL normally has at least two ion components – high speed beams and ions transported from the lobe into the plasma sheet. *Nakamura et al.* [1992] showed experimental evidence for these two ion components. Recent observations of single tailward ion beams [*Parks et al.*, 1998, 1999] indicate that other components exist in the PSBL. Ion flows in the PSBL typically come from the ion beams propagating in both directions along the magnetic field. *Parks et al.* [1998, 1999] found that while the distribution function containing the earthward going beams consists primarily of the ion beams, the distribution of tailward going beams includes the beam plus an isotropic component. When these two types of distributions are convolved to compute the mean velocity, large mean values $> 400 \text{ km/s}$ result in the earthward direction and smaller values $< 200 \text{ km/s}$ in the tailward direction.

In the CPS the bulk flow is mainly determined by large scale $\vec{E} \times \vec{B}$ convection. Ion distributions with multiple components, as found in the PSBL, are thought to be rarely observed in the CPS. *Paterson et al.* [1998] surveyed the PS between 10 and $50 R_E$. They found that perpendicular flows were slow, and on the whole consistent with plasma convection. Surprisingly, for parallel flows the most probable value was negative, and in the range -100 to 0 km/s. Another recent study, by *Borovsky et al.* [1997], found that at low velocities ($< 250 \text{ km/s}$) plasma sheet turbulence appears to be isotropic. On the other hand, fast flows above 300 km/s appear more structured. Fast ion flows in the CPS have been extensively studied in the past two decades [*Angelopoulos et al.*, 1996a,b and references therein]. Whereas in the PSBL, the fast flows are nearly field-aligned, in the CPS and near the current sheet region about 70% of the fast flows are predominantly perpendicular to the magnetic field direction

[*Baker et al.*, 1996]. Thus in the CPS much of the fast plasma transport is across field lines rather than along them. Though fast flows in the CPS are bursty with a duration of only a few minutes, it is claimed that they are responsible for most of the tail plasma and magnetic flux transport [*Angelopoulos*, 1992, 1994]. There is, however, disagreement in the field regarding this (see *Paterson et al.*, [1998, 1999]; *Angelopoulos et al.* [1999]). A one-to-one correlation between fast bursty flows and substorm phase is not clear [*Angelopoulos et al.*, 1992].

Nakamura et al. [1991, 1992, 1994] have studied the characteristics of the plasma flows in the CS region, where the magnetic field is weak. They found that high speed flow events ($V > 300 \text{ km/s}$) are usually restricted to the region tailward of $X = -25 R_E$, and are predominantly sunward or tailward. Studies of bursty flows [*Baumjohann et al.*, 1990; *Angelopoulos et al.*, 1992, 1994] have been careful to distinguish CPS flows that are perpendicular to the ambient magnetic field from the field-aligned flows observed within the PSBL [*Eastman et al.*, 1984, 1985]. Recently, *Lyons et al.* [1999, 2000] found evidence that the flows within the CPS and those within the PSBL may not be distinct phenomena. They found that when they are observed, significant flows appear to exist throughout the entire height of the tail plasma sheet, and are associated with structured currents in the tail. This lends credence to the postulate of *Rostoker*, who writes, "Surely, at least at some times during substorm disturbed intervals, the plasma sheet thins and thickens causing flows localised in the Z-direction to be swept past a satellite giving the signature of BBFs" [*Lui et al.*, 2000].

1.4 Motivation

The principal issue addressed in this thesis is whether it is possible to have anisotropic anti-sunward flows in the PS without appealing to neutral lines. It is common to interpret fast flows during substorms in terms of a neutral line [Machida *et al.*, 1994; Nagai *et al.*, 1998; Baker *et al.*, 1999]. Fast tailward flows are normally associated with the development of the near-earth neutral line (NENL) [Angelopoulos *et al.*, 1992, 1994]. Could it be that at least some tailward flows are a consequence of PSBL dynamics, independent of any explanation related to near-earth neutral lines? This is the question addressed in this thesis.

Whether these fast flows reflect streaming along field lines, or convection has been debated (e.g., Rostoker and Boström, 1976), but the results are not conclusive. In the following chapter it is shown that a rapidly varying magnetic field may sometimes blur the distinction between parallel and perpendicular flow. Furthermore, some evidence suggests that tailward flows are not necessarily the *smoking gun* for reconnection earthward of the spacecraft. For example, Lyons *et al.* [1999, 2000] found evidence that the flows within the CPS and those within the PSBL may not be distinct phenomena, and that significant flows appear to exist throughout the entire height of the tail plasma sheet. Thus tailward flows could be associated with some flapping motion of the magnetotail in the Z-direction. If this is the case tailward flows in the current sheet might be present regardless of the presence or absence of a neutral line. Such a result would not negate the fact that neutral lines cause fast flows to jet away from them, but rather suggests caution in automatically assuming that fast flows are always caused by neutral lines. This thesis is certainly not an attempt to produce an "anti-NENL" stand, but rather springs from the strong feeling that broadening the range of possible models for tailward flows would be very healthy for

the field of space physics.

The formation of neutral lines is not a necessary prerequisite for acceleration, since acceleration in any region featuring a weak magnetic field normal to the NS also leads to plasma flows at the outer boundary of the plasma sheet [*Lyons and Speiser, 1982*]. Other possibilities include acceleration from inductive electric fields which develop as magnetic fields reconfigure during enhanced activity [*Pellinen and Heikkila, 1978*]. As well, beams of energetic ions may execute several bounces through the plasma sheet and gain energy through Fermi acceleration. The adiabatic compression (betatron) mechanism is also favourable to produce acceleration. This occurs when a particle is convected from a region of weak magnetic field into a region of strong magnetic field. A recent study by *Liu [2000]* uses an MHD approach to demonstrate that, without a neutral line or other extraneous assumptions, a highly curved current sheet can generate high-speed cross-field flows of $>100 \text{ km/s}$, when perturbed by small impulses of $\sim 10 \text{ km/s}$ at its boundary.

In the physics of the process near-earth, it appears that the most sensitive region would be in the region of the earthward edge of the intense crosstail current sheet. It is here that the crosstail electric field will have been largely shielded out. It is also here that weak magnetic field regions develop during the growth phase of the magnetospheric substorm. A charged particle near such a region will first pass through sharp gradients in magnetic field and subsequently find itself in a weak magnetic field. In this place the particle may become demagnetised through nonadiabatic processes. This research will investigate whether anisotropic tailward ion flows can be formed near the magnetotail current sheet (CS) region as a consequence of the interaction of earthward PSBL beams and the stretched magnetotail geometry at the boundary between dipolar and tail fields.

Computer test particle simulations are performed in a new magnetic model of the magnetotail which was developed to represent substorm growth phase. This model comprises a dipole and tail component. A feature of this model is a near-earth electric current configuration which is consistent with azimuthally localized enhanced magnetic field stretching. The model is constrained using statistical information and real-time data from the CANOPUS ground based scanning photometer data base of observed auroral features. Chapter 2 present examples of fast flows measured in the magnetotail, and discusses them in terms of time aliasing problems. In chapter 3 the test particle modelling technique is invoked. Thereafter, in chapter 4, the new model of the magnetotail is introduced, and is used to show that the growth phase stretching of the magnetic field lines is clearly associated with equatorward motion of luminosity. Chapter 5 applies the test particle technique to calculate ion distribution functions at various locations in the model magnetotail. Results from the computer simulations are used to demonstrate how plasma flows in the magnetotail can develop during substorm growth phase, or at times when the magnetotail magnetic field is highly stretched. Electrostatic noise, added to the model PSBL, is applied to the test particle simulation in order to study the effect of model wave-particle interactions on the distribution functions. The final chapter concludes this study with a summary and discussion of the results.

CHAPTER 2

Plasma Flows in the Magnetotail

This chapter considers the meaning of plasma flow. Since consideration of flows in different magnetotail regimes forms an important part of this thesis, it is important, from the outset, to have a good understanding of the meaning of *flow*. This discussion has at least two aspects: first, the distinctions between characteristics inferred from plasma moments and the true characteristics of the actual particle distributions, and second, errors in the interpretation of plasma moments due to time averaging effects. Ambiguities which can arise from computed moments are discussed briefly in section 2.1. The second aspect of plasma flows is more important and is discussed in the context of experimental observations of fast ion flows in the magnetotail. Sections 2.2 and 2.3 serve to demonstrate limitations due to time averaging effects, and warn against assuming a particular source of ion acceleration based on moment calculations alone. Examples of fast ion flows observed by the WIND satellite are presented, and discussed. Flows *perpendicular* to the magnetic field are especially important, since these are frequently identified with plasma transport and the start of reconnection at a neutral line [Angelopoulos *et al.*, 1992, 1994, 1996a; Sergeev *et al.*, 1995; Nagai *et al.*, 1998]. However, if the magnetic field changes very rapidly, while the distribution function is being formed, the convolution of the flow into parallel and perpendicular components may be very ambiguous, since an averaged magnetic field is used to determine these directions. Another well known aspect is that ambiguity arises when the plasma distribution itself changes very rapidly.

2.1 Ion distributions and moment calculations

Usually, one is encouraged to think of a flow as comprising a sequence of well defined entities moving from one place to another in a uniform way. Collections of particles, moving in a preferential direction, constitute a flow. In the magnetotail, particles are able to move in different directions, at different speeds while obeying the *laws* of physics in an essentially collisionless environment. To determine the flow at a detector location, one must first know the time dt over which the particles incident on the detector are to be counted as well as the energies of those particles. The ability to discriminate between ions and electrons is also a requisite. After averaging over all the particles, one may use the distribution function to calculate density, bulk velocity, as well as other moments. For example, the number density for a particle species is calculated from the velocity distribution function, $f(\vec{v})$, from

$$n = \int f(\vec{v})d^3v, \quad (2.2.1.1)$$

and the bulk velocity as

$$u_\alpha = \frac{1}{n} \int v_\alpha f(\vec{v})d^3v, \quad (2.2.1.2)$$

where the subscript α is a coordinate index.

In the example in Figure 2.1 a cartoon of consecutive ion distribution functions is shown (top) along with the density and velocity moments (bottom). The distributions are shown as isocontours in velocity space, expressed with velocities parallel and perpendicular to the ambient magnetic field. At the start of the interval the bulk velocity is in the $-V_{par}$ direction, which is along the magnetic field (V_{per} is velocity

perpendicular to the magnetic field). Soon thereafter the plasma became more dense and stagnant.

More complex situations can arise when some of the ions travel in a roughly $+V_{par}$ direction, and the rest are travelling in the opposite direction, as illustrated in Figure 2.2. In this latter case there are clearly two main groups of ions that behave differently. Although the density and velocity moments from these distribution functions come out the same, the two situations are very different on an individual particle basis. If one looks at the density and velocity moments only, and assumes that the majority of ions do not have greatly different velocities, as in Figure 2.1. then fluids-based intuition might lead one to conclude that during times $t = 0, 2$ the measurement was taken in a steady $-V_{par}$ flow. At times $t=4-10$, one has moved into a stagnant flow. The distribution functions in Figure 2.2 tell a different story and violate simple fluids-based perceptions. Of course, calculation of higher order moments, such as temperature, would give different results and in this case allow one to discriminate. However, such discrimination is not always possible via moment calculations alone. This example demonstrates the importance of looking to parent velocity distributions to understand the meaning of a flow. Although space physicists are very aware of these limitations it bears repeating since many conclusions have been based primarily on moment calculations. Due to awareness of these limitations there is increasing emphasis on analysis based on distribution functions (e.g. *Martin and Speiser, 1988; Martin et al, 1996; Nagai et al., 1998; Hoshino, 1998*), and the urgent need to go beyond the current understanding based on magnetohydrodynamic (MHD) physics is being stressed [*Parks et al., 1998, 1999, 2000*].

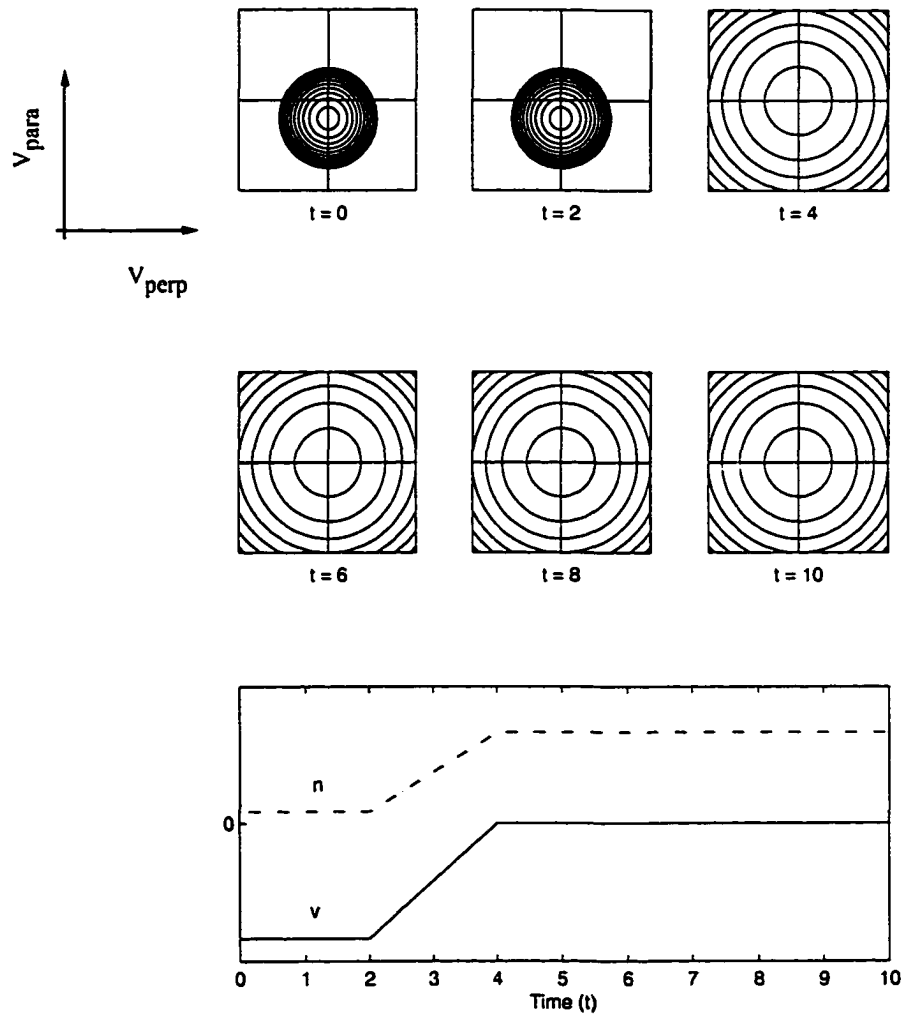


Figure 2.1: A schematic portraying (top two rows), from left to right, ion distribution functions in velocity space at different times. The third row shows the moments (density and velocity) calculated from the distribution functions.

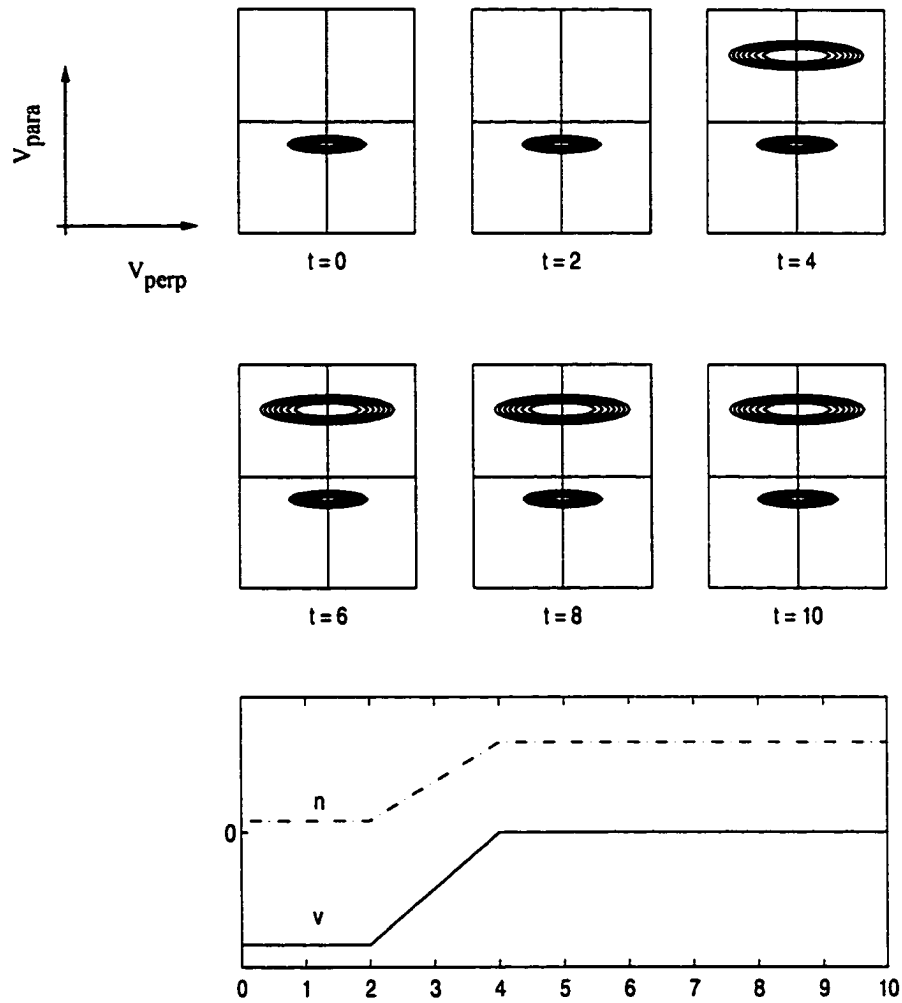


Figure 2.2: A schematic portraying (top two rows), from left to right, ion distribution functions in velocity space at different times. The third row shows that the moments (density and velocity) calculated from the distributions are identical to those shown in the previous figure.

2.2 Limitations due to time averaging

As illustrated in the simple examples from the previous section it is the distribution functions themselves, which provide information regarding the particle source regions. It is also important to consider electric and magnetic field variations when making conclusions based on moment calculations. This well-known fact bears repeating. Making conclusions on the basis of moment calculations *alone* is a science fraught with dangers. Ideally, the convolution of the distribution function, to compute moments, provides an instantaneous "measurement". In reality an experimenter needs to count particles for a certain length of time, dt , and only then add the particles up and form a distribution function. To get a clear understanding of what is happening in the flow, one requires that during dt particle and field behaviour is fairly constant. In the magnetotail, where rapidly varying electromagnetic fields are often found, moment calculations may sometimes be misleading, unless their limitations are well understood.

In principle, when the magnetic field (or electric field) is rapidly varying, there may be difficulty in separating convective flows from streaming flows. This will be especially true if the time dt , to form the distribution function, is longer than the time scale of the field variations. Since each distribution has direction defined via the average magnetic field over dt , another problem that may arise is that the position in time of the flow velocity peaks can be incorrectly estimated. These timescale limitations will now be illustrated via consideration of examples of fast magnetotail plasma flows found in the magnetotail.

2.3 Plasma flows from the WIND satellite

The WIND satellite was launched on November 1, 1994 with a large array of scientific instruments, descriptions of which are published in *Space Science Reviews*, 71, Nos.1/4, 1995, pp. 1-878. The review by *Lin et al.* [1995] describes the three-dimensional plasma and energetic particle investigation (3DP) which provides particle count rates in three orthogonal directions. These data are used to compute velocity distribution functions. The 3DP detectors are electrostatic analyzers, capable of discrimination between electrons and ions. However, discrimination between different ion species is not possible. In this section, timescale limitations in moment data are considered via a study of data measured by the 3DP instrument. Velocity distribution functions are calculated over two different count times, viz. 96- and 48-s, and the velocity moments derived from these distributions are compared. The natural frame in which the distribution function is calculated is that of the magnetic field. For directional purposes each distribution function calculated requires an average magnetic field for the selected integration interval.

Since distributions are calculated in magnetic field coordinates, the meaning of a plasma flow involves at least two further ideas - flows parallel to the magnetic field, and flows perpendicular to the magnetic field. In the MHD context flows perpendicular to the magnetic and electric field are always convective (in the $\vec{E} \times \vec{B}$ direction). However on WIND, directional information for DC electric fields is not provided, so it is not certain what proportion of the bulk perpendicular flow is convective. Since its launch the WIND spacecraft has made numerous perigee passes through the plasma sheet, about 25 of which are equatorial perigee passes. Several perigee passes have been studied, and in what follows data from September 16, 1995 and October 21, 1997 are used to demonstrate limitations due to timing of fast flows.

2.3.1 September 16, 1995

Just after 2330 UT on September 16, 1995 WIND was in the PS at $(-13.4, 8.4, 1.7) R_E$ in GSE coordinates. During 2330-2345 UT the density remained above 0.1 cm^{-3} , and the temperature increased steadily to $\sim 3 \text{ keV}$ (not shown), as WIND approached the CS region. Figure 2.3 summarises the salient features of the magnetic field behaviour and velocity moment parameters. In the upper three panels the three second magnetic field values, in GSE coordinates, are shown as the light solid line. The dot-dash and dark solid lines are, respectively, the magnetic field averages used to calculate velocity moments from 48-s and 96-s ion distribution functions. The three bottom panels show the velocity moments in GSE, calculated from the 48-s and 96-s ion distribution functions. During the interval shown, the B_x component increases from large negative values, and shows that WIND crosses the neutral sheet (NS) several times, the first time around 2338 UT. Here a NS crossing is defined as $B_x=0$. Figure 2.4 shows velocity moments in directions parallel and perpendicular to the magnetic field, and projections of the perpendicular velocity into the GSE plane.

As it crosses the NS, WIND observes a fast earthward flow, at around 2339 UT. Ground based magnetograms (not shown) indicate that at this time the magnetic field changed rapidly and was associated with a substorm intensification; it is likely that this fast flow coincides with one of several intensifications that occur after the initial expansive phase onset. Figure 2.5 shows consecutive isocontour plots of 3D ion velocity distribution functions, calculated using 48-s integration times. Each panel shows logarithmically spaced isocontours of ion phase space density in $(V_{\parallel}, V_{\perp})$ -space. Negative V_{\perp} points correspond to particles with velocities having $V_{\perp} \cdot U_{\perp} < 0$; where U_{\perp} is the component of the bulk flow velocity perpendicular to the magnetic field vector. Velocity moments from these distributions, and average magnetic field, in GSE

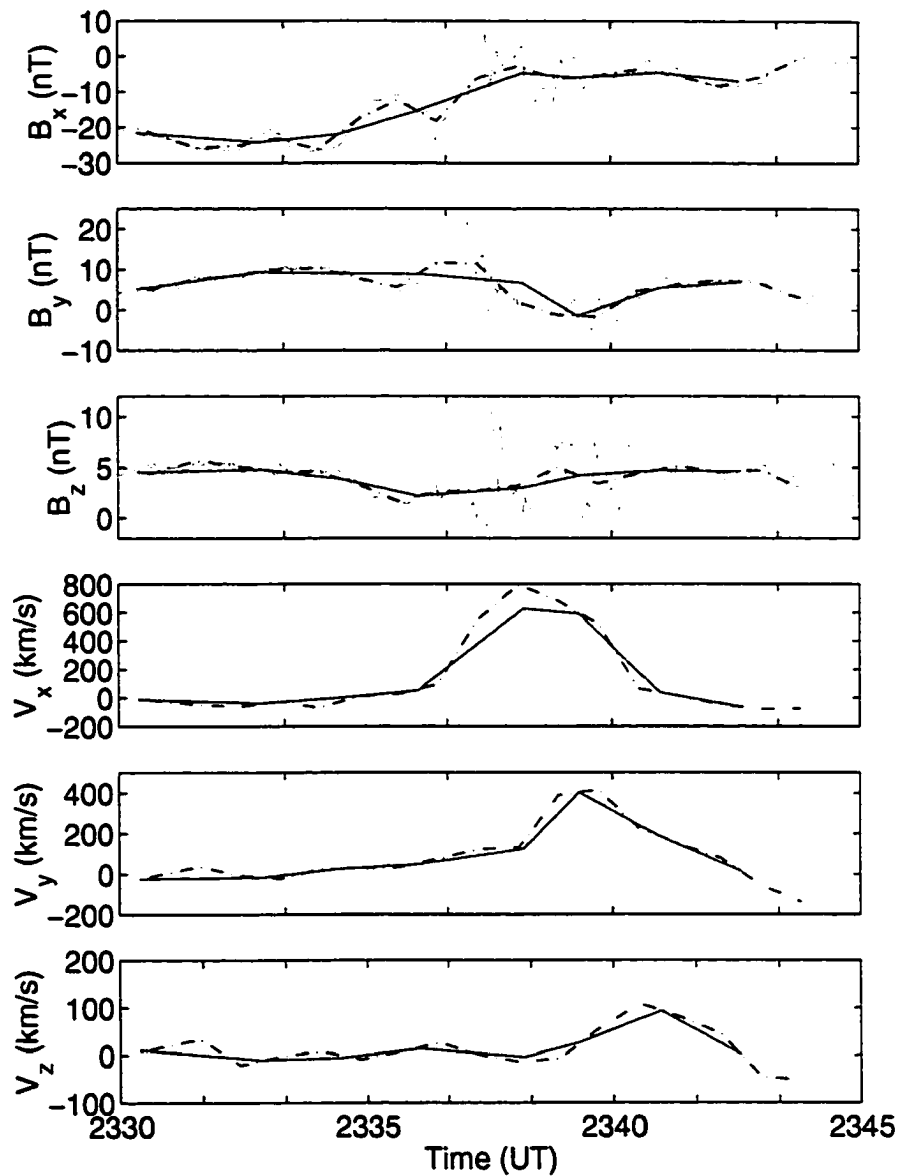


Figure 2.3: Magnetic field and velocity moments on September 16, 1995 from 2330-2345 UT. The top three panels show the magnetic field. The light solid, dot-dash, and dark solid curves are, respectively, the 3 second, 48 second, and 96 second averaged magnetic field in GSE coordinates. The bottom three panels are the velocity moments. The dot-dash and solid curves are, respectively, calculated from the 48 and 96 second distribution functions.

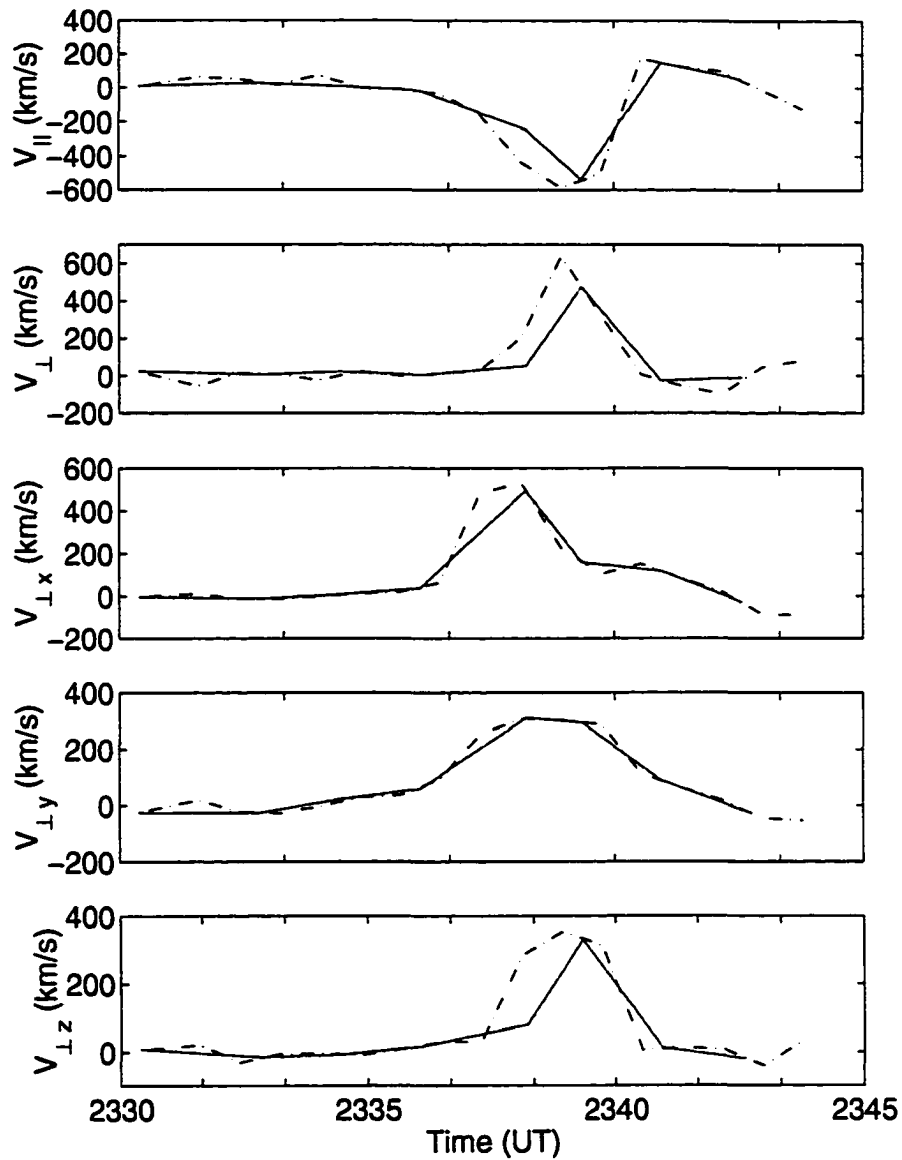


Figure 2.4: Velocity moments on September 16, 1995 from 2330-2345 UT. The top two panels show the velocity in directions parallel and perpendicular to the magnetic field. The dot-dash and solid curves are, respectively, calculated from the 48 and 96 second distribution functions. The bottom three panels show the projections of the perpendicular velocity into the GSE plane.

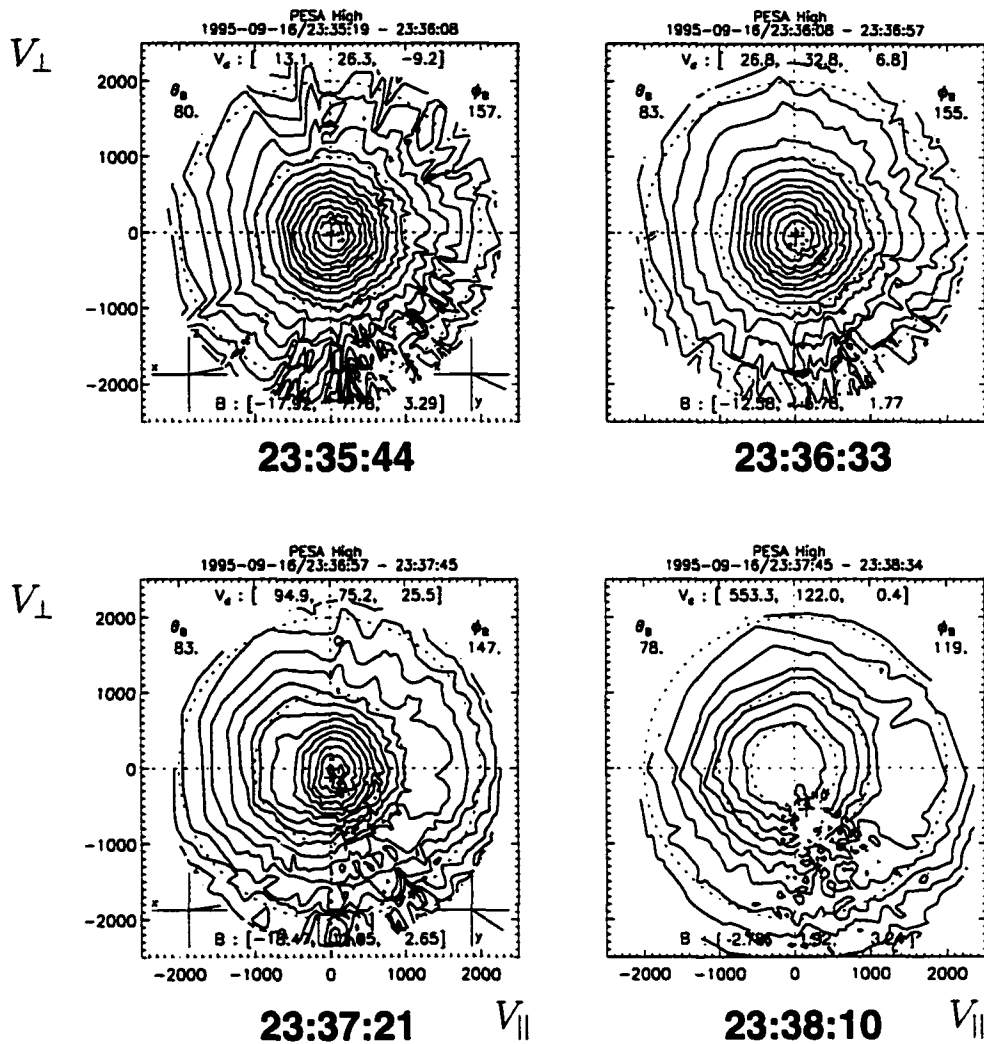


Figure 2.5: Ion distribution functions in velocity space on September 16, 1995. All four velocity distribution functions are consecutively measured using a 48-s integration period. Each panel shows logarithmically spaced isocontours of ion phase space density in $(V_{\parallel}, V_{\perp})$ -space. Negative V_{\perp} points correspond to particles with velocities having $V_{\perp} \cdot U_{\perp} < 0$; where U_{\perp} is the component of the bulk flow velocity perpendicular to the magnetic field vector. Concentric dashed circles indicate total velocities of 1000 and 2000 km/s. The UT time about which the data are centred is shown below each distribution function. Bulk velocity moments and average magnetic field, in GSE-coordinates, are shown on each plot.

coordinates, are shown in each plot. Each distribution function is centred about the time shown below it. Just after 2335 UT the satellite was sampling the CPS, and the distribution function centred around 2335:44 UT is quasi-isotropic. The second 48-s distribution, centred around 2336:33 UT is warmer, and coincides with the decrease of the B_x component of the magnetic field, which may be interpreted as movement of the satellite towards the CS region. In the third distribution the bulk velocities become non-negligible at the same time as a rapid increase in local B_y begins. The increase in B_y occurs also as B_z is rapidly varying, and these variations are possibly associated with field-aligned currents. Finally, the distribution function centred about 2338:10 UT comprises a single component distribution of ions contributing to a bulk earthward and duskward flow of $(V_x, V_y)=(553,122)$ km/s.

Figures 2.3 and 2.4 show that there is little qualitative difference between the 48-s and 96-s velocity moments. The largest differences occur when the average magnetic fields, used for the 48-s and 96-s distributions, are different. which is essentially due to time averaging. These differences are greatest between 2335-2340 UT, particularly in the B_x and B_y components. Nevertheless, the variations in the average magnetic fields result in some differences in the moment calculations. The averaging effect results in a timing difference in the peak of the fast V_x flow, and in V_{\perp} (second panel Figure 2.4) at 2338:20 UT. For the 48-s case, the estimate of the maximum perpendicular flow velocity is displaced by about 50 seconds from the estimate of the maximum perpendicular flow for the 96-s case. The other time averaging effect, due to unequal 48- and 96-s magnetic field averages, is that the differences between the 48-s and 96-s velocity moments can be over ~ 200 km/s. Such large errors are not only evident in the moments separated into parallel and perpendicular velocities, but are also seen clearly, for example, in V_x around 2338 UT.

In conclusion, substantial differences in the velocity moments come from averaging errors, when a different average magnetic field is used for the 48-s and 96-s moment calculations. Although the 3-s magnetic field values show much more structure than the averaged magnetic fields, this did not result in greater errors in the velocity moments, because neither the 48- or 96-s average magnetic field were able to resolve these rapid variations. However, the rapid variation of the magnetic field does result in ambiguities in the separation of convective flows and streaming flows; velocity moments calculated using different magnetic field averages can result in substantial differences. Rapid magnetic field variations, especially in the CS region, can imply a rapid change in magnetic field direction. When the calculation of a distribution function uses a magnetic field average that cannot resolve the rapid magnetic field variations, the perception of plasma transport can be affected. As a result statistical studies using arbitrary cutoff criteria have to be very carefully monitored so that bursty perpendicular flows are not incorrectly assigned.

2.3.2 October 21, 1997

At 1340 UT on October 21, 1997 WIND was in the PS at $(-16.5, 1.2, -1.2) R_E$ in GSE coordinates. During the interval 1340-1355 UT B_x became increasingly negative, indicating that the satellite was probably approaching the PSBL. Salient features of the magnetic field behaviour and velocity moment parameters for the time interval 1340-1355 UT, are summarised in Figures 2.6 and 2.7.

B_z was large and oscillatory during the entire interval shown. Both the 48-s and 96-s averaged magnetic fields are qualitatively in agreement with the 3-s field, but the 96-s average B_z data smooths out the oscillations seen in the 3-s data. The largest differences between the 48-s and 96-s average magnetic fields occur around

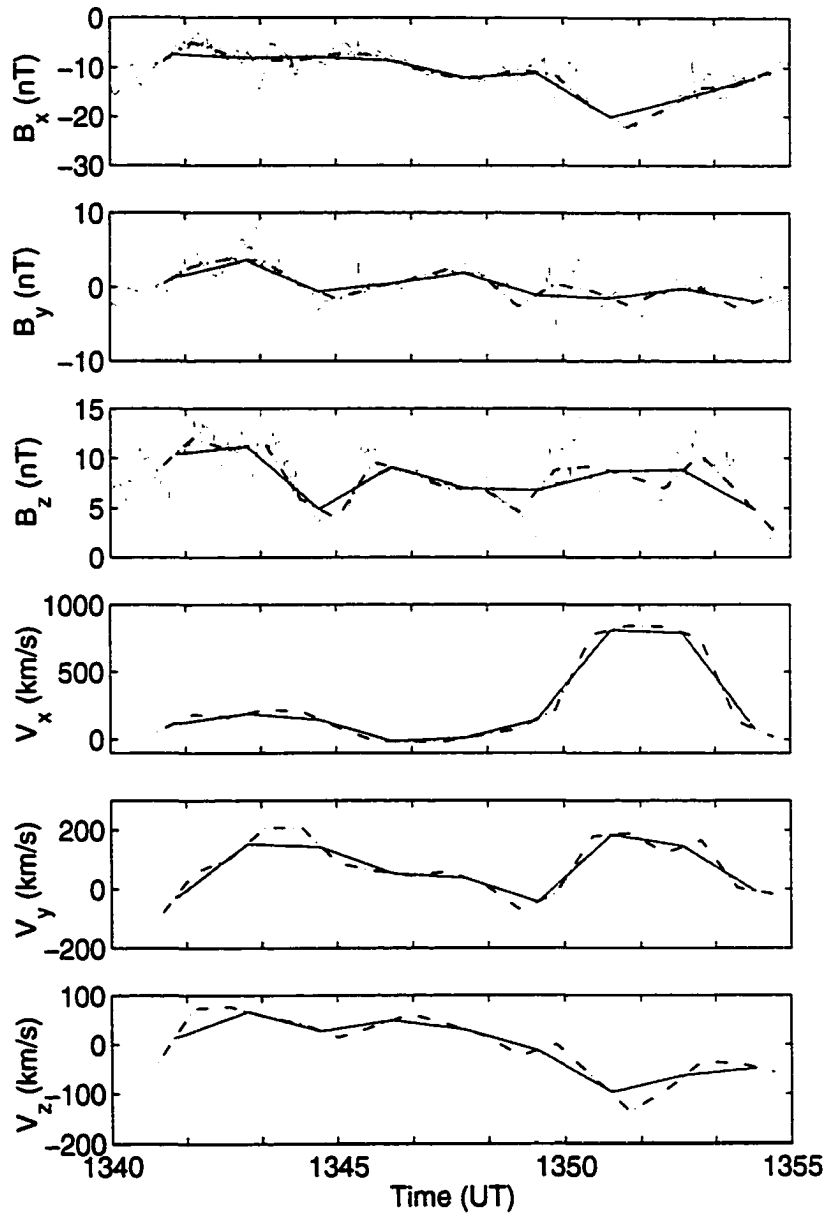


Figure 2.6: Magnetic field and velocity moments on October 21, 1997 from 1340-1355 UT. The top three panels show the magnetic field. The light solid, dot-dash, and dark solid curves are, respectively, the 3 second, 48 second, and 96 second averaged magnetic field in GSE coordinates. The bottom three panels are the velocity moments. The dot-dash and solid curves are, respectively, calculated from the 48 and 96 second distribution functions.

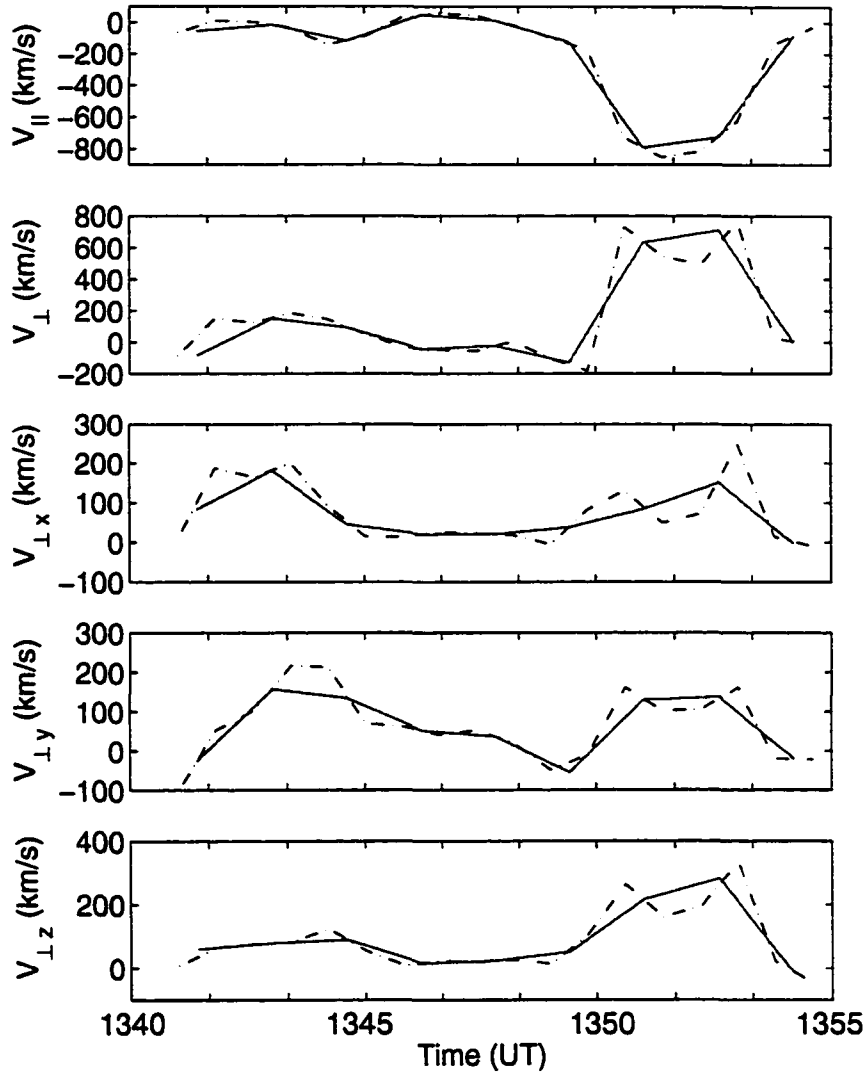


Figure 2.7: Velocity moments on October 21, 1997 from 1340-1355 UT. The top two panels show the components of velocity in directions parallel and perpendicular to the magnetic field. The dot-dash and solid curves are, respectively, calculated from the 48 and 96 second distribution functions. The bottom three panels show the projections of the perpendicular velocity into the GSE plane.

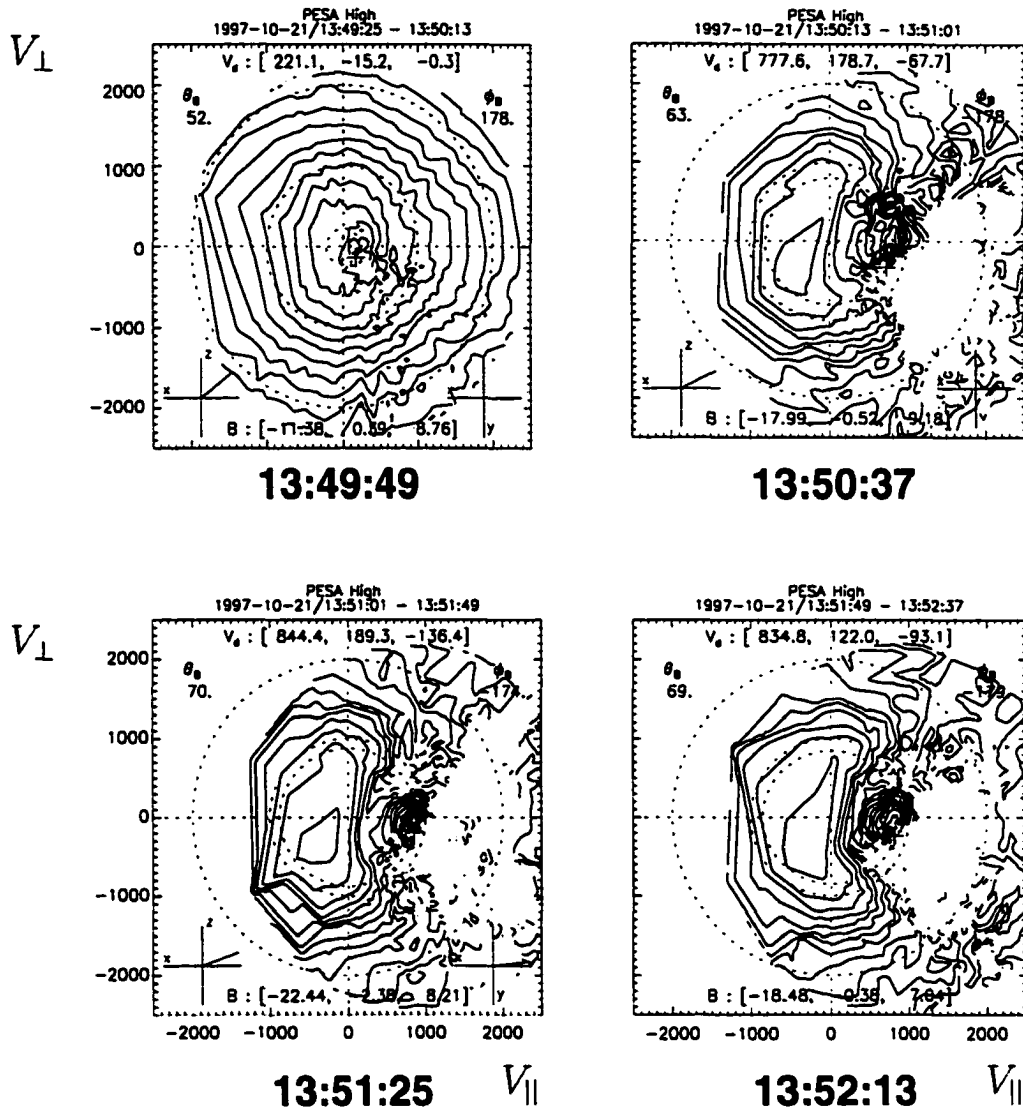


Figure 2.8: Ion distribution functions in velocity space on October 21, 1997. All four velocity distribution functions are consecutively measured using 48-s integration period. Each panel shows logarithmically spaced isocontours of ion phase space density in $(V_{\parallel}, V_{\perp})$ -space. Negative V_{\perp} points correspond to particles with velocities having $V_{\perp} \cdot U_{\perp} < 0$; where U_{\perp} is the component of the bulk flow velocity perpendicular to the magnetic field vector. Concentric dashed circles indicate total velocities of 1000 and 2000 km/s. The time about which the data are centred is shown below each distribution function. Bulk velocity moments and average magnetic field, in GSE-coordinates, are shown on each plot.

1343:20, 1349:10, and 1351:40 UT. It is around these times that large differences in the 48-s and 96-s velocity moments occur, particularly when they are expressed in coordinates parallel and perpendicular to the magnetic field.

The velocity moments show that the flow is mainly in the X -direction. Prior to ~ 1350 UT the velocities are quite small. Splitting the moments into directions parallel and perpendicular to the magnetic field shows that both parallel and perpendicular velocities are large around 1350 UT (first two panels of Figure 2.7). Whereas the 48-s moments resolve two bursts of fast V_{\perp} flow between 1349-1355 UT, time averaging results in the observation of only one steady fast flow for this interval from the 96-s moment. As for the September 19, 1995 case, during times when the 48-s and 96-s average magnetic fields differ substantially, there are differences greater than 200 km/s in the velocity moments calculated.

Figure 2.8 shows four consecutive ion distributions (48-s integration times). As before, each panel shows logarithmically spaced isocontours of ion phase space density in $(V_{\perp}, V_{\parallel})$ -space. When the fast flow is observed at ~ 1350 UT the X -component of the magnetic field is becoming increasingly negative, and the distribution functions indicate a beamlike distribution characteristic of the PSBL. The quasi-isotropic distribution, measured around 1349:49 UT, is calculated immediately prior to the observation of the fast V_x flow. Fast ion beams with flow towards the earth along the magnetic field, are seen in the next three distributions. A colder ion component exists, which has a positive V_{\perp} drift velocity, different from the negative drift velocity of the beam component, and also has a tailward drift along the magnetic field.

One might expect that serious time averaging effects would only occur when the magnetic field is so small that particles do not follow the field, but this event is primarily a PSBL event (with plasma $\beta < 1$), and shows similar problems as the

September 16, 1995 event, which was near the CS region (and had $\beta > 1$). Thus averaging effects appear to be important irrespective of observation location in the magnetotail.

2.4 Conclusions

These data demonstrate that calculation of velocity moments from distribution functions with integration times that do not adequately resolve magnetic field variations can result in velocity moments which may be misleading. The first problem noted was that sometimes a velocity peak calculated using 48-s moments is displaced in time from estimates of the peak position computed from 96-s distributions. This effect is not unexpected and was observed to some degree in all the data. One would expect that these time-difference errors would always be less than the maximum integration interval used to calculate the distributions. Another problem, which is also to be expected, is that when the integration time is large, it is not possible to detect finer structures in the flows, such as the multiple peaks in the 48-s V_y and V_{\perp} moments on October 21, 1997.

A more significant time averaging problem arises when the magnetic field averages, used to determine parallel/perpendicular flows from distributions, are quite different for the 48-s and 96-s distribution functions. This effect is seen in both examples, irrespective of whether the observation was in the PSBL or CS region. The variable magnetic field results in different magnetic field averages for the 48-s and 96-s moments, and ended in calculated velocities that can differ by more than 200 km/s. Such results should serve as a caution for studies that automate the separation of velocity moments into parallel and perpendicular components; recent interactions between *Angelopoulos et al.* [1999] and *Paterson et al.* [1999] indicate some of the

difficulties that may arise in flow studies that separate velocities into components parallel and perpendicular to the magnetic field.

In this chapter the data shown have demonstrated that, for the most part, distributions from the WIND satellite, using 48- and 96-s convolution times, produce similar velocity moments. Time-difference errors in the peaks of velocity occur, but these are never more than 96-s, the slowest integration time used in this study. The data suggest that variability of the average magnetic field can result in moments that contain errors greater than 200 km/s. Some statistical studies have used automated techniques with arbitrary velocity cutoffs to draw conclusions regarding source, and acceleration mechanisms in the magnetotail (e.g. *Baumjohann*, 1990; *Angelopoulos et al.*, 1992, 1994). The results of this study demonstrate that, in some cases, such statistical studies might possibly come to different conclusions if they used distribution functions able to adequately resolve fast magnetic field variations.

CHAPTER 3

Test particle modelling technique

3.1 Test particle simulations

A first step towards describing and understanding the motion of a system of charged particles is to study analytically how the individual particles move around in given electromagnetic fields. Even then, the Lorentz equation is not easily solved except for a few simple cases. In complex electromagnetic field geometries the Lorentz equation can be solved by perturbation methods. First-order perturbation theory, also known as guiding centre theory, is an approximate method that provides an average picture of particle motion in complex field geometries.

A better approach is to use the concept of the distribution function and the tools of statistical mechanics to study the motion of a large number of particles. Local distribution function signatures are manifestations of topological properties and carry information on large scale features in the magnetosphere. The ability of charged particles to carry information and energy over great distances ($\gg R_E$) in the essentially collisionless magnetotail, means that the global particle dynamics can influence the distribution of internal energy and currents on a large scale. Although the study of distribution functions can be rewarding, it involves solving the Boltzmann transport equation which is extremely difficult. Electron gyroradii are so small that their motion is usually completely specified by the guiding-centre drift. By contrast, especially near the magnetotail current sheet, ion gyroradii are large such that their

gyro-orbits are not complete. Guiding-centre motion does not take place and the orbits of this type of ion are primarily determined by their inertia and the electrostatic field. Magnetic fields become important when the ion gyroradius is small, i.e. of the order of the magnetic field line curvature radius. Then the particle trajectories can become chaotic.

Because of the complicated magnetic geometry of the tail, including sharp field reversals, neither a magnetohydrodynamic (MHD) approach nor guiding centre approximations can adequately describe the particle motion and dynamics. Since the tail forms the region of interest in this study, the full Lorentz force equation is used to follow single particle trajectories. In this chapter the method of distribution function calculation will be explained and demonstrated. First, important preliminaries must be discussed. Next the modelling technique is explained, and finally is demonstrated via simple models.

3.2 Ion distributions

3.2.1 Vlasov's equation

In its simplest form a plasma consists of electrons and single ion species. A more complex plasma comprises many different ion species as well as neutral atoms and molecules. For example, the earth's ionosphere includes complex molecules like O^+ , N_2^+ , and NO^+ . The dynamic plasma system of interest in this study is the magnetotail. The tail lobes and plasma sheet have a volume on the order of $10^{30} cm^3$ [Chappell *et al.*, 1987]. Density measurements indicate that on the order of 10^{30} particles reside there. Thus our system of interest is huge and contains a tenuous plasma. In tenuous plasmas, collisions between the charged particles are rare and an

understanding of plasma phenomena requires a knowledge of the individual particle motions in the electromagnetic fields. But the magnetotail contains so many particles that it is not feasible to observe the behaviour of all the individual particles. Each particle in the system follows its own special trajectory which can be labelled with the index i . It has three displacement coordinates, \vec{r}_i , and three velocity coordinates \vec{v}_i that specify its dynamic location at a particular time. Together, \vec{r}_i and \vec{v}_i describe the six-dimensional phase space, (\vec{r}_i, \vec{v}_i) . When an ion is described by its motion through phase space, one must understand that it does not really *move* in phase space, it is the system points that move. Each physical plasma particle is only *represented* by its own system point in phase space. A reference to particle motion in phase space, is in fact a reference to the motion of the system points in phase space.

So many plasma particles reside in the magnetotail that, in lieu of the coordinates of all the particles, the system is best described by a statistical distribution of particles (i.e. system points) in the phase space. For n particles, this comprises a $6n$ dimensional space. The distribution function defining the state of the phase fluid is a continuous function, $F_n(\vec{r}_1, \vec{v}_1, \dots, \vec{r}_n, \vec{v}_n, t)$, of all the single-particle displacements and velocities, as well as time. It describes the motion of a group of particles moving through the phase space, and corresponds to a phase space density. Distribution function moments are defined in terms of integrations over some of the microscopic individual phase spaces of particles contributing to F_n . An integration with respect to the whole individual phase space of particle i , removes the coordinates of this particle [Baumjohann and Treumann, 1996]. Its contribution to F_n is spread to the remaining particles as an average effect on the distribution function. Successive integrations will destroy the individuality of the particles until only one reduced distribution function $F_1(\vec{r}_1, \vec{v}_1)$ is left [*ibid.*]. This distribution function describes all the particles equally well. Thus F_1 is the number of particles which are at phase coordinates (\vec{r}_1, \vec{v}_1) per

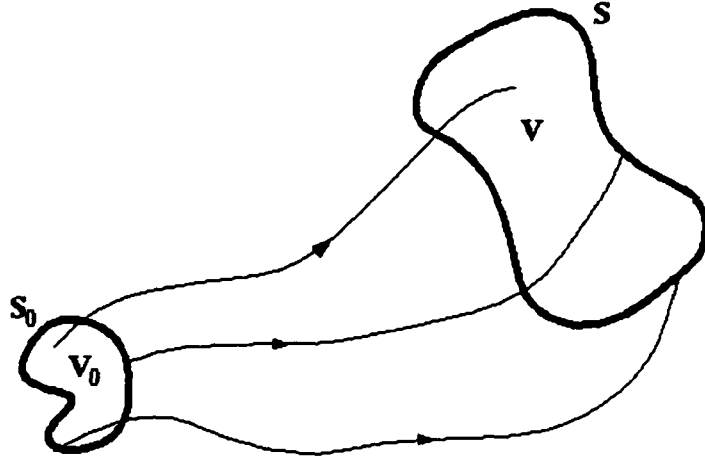


Figure 3.1: Conservation of particles and momentum in the absence of collisions is applied to a finite volume in phase space. Trajectories in phase space are labelled with arrows in the direction from the volume V_0 to the volume V . Each trajectory corresponds to a line of constant phase space density.

unit $d\vec{r}$ and per unit $d\vec{v}$ at time t . The number of particles (i.e. system points) dn_1 in the phase space volume $d\vec{r}d\vec{v}$ is

$$dn_1 = F_1(\vec{r}_1, \vec{v}_1, t)d\vec{r}d\vec{v}. \quad (3.3.2.1)$$

The trajectories of three initial conditions are shown in Figure (3.1). Here the phase space is represented in two dimensions with the three velocity components \vec{v} along the ordinate and the three position components \vec{r} along the abscissa. The trajectories in phase space never intersect at a given instant in time because each trajectory represents an independent system in the plasma ensemble. If two trajectories came together they would have the same initial values of \vec{v} and \vec{r} at that time, and their subsequent motion would be identical. Furthermore, the boundary S_0 of the phase space volume V_0 transforms into a boundary S which bounds the same group of initial conditions.

If the symbol for the reduced distribution function is replaced by $f(\vec{r}, \vec{v}, t) = F_1(\vec{r}_1, \vec{v}_1, t)$, one can obtain Vlasov's equation [Baumjohann and Treumann, 1996],

$$\frac{\partial f}{\partial t} + \vec{v} \cdot \frac{\partial f}{\partial \vec{r}} + \frac{q}{m} (\vec{E} + \vec{v} \times \vec{B}) \cdot \frac{\partial f}{\partial \vec{v}} = 0. \quad (3.3.2.2)$$

3.2.2 Liouville's theorem

Vlasov's equation (equation 3.3.2.2) may be rewritten

$$L f = 0 \quad (3.3.2.3)$$

where L is the operator

$$L = \frac{\partial}{\partial t} + \vec{v} \cdot \nabla + \vec{a} \cdot \nabla_v \quad (3.3.2.4)$$

This is just the total time derivative following a particle's motion in phase space; i.e.

$$\frac{df}{dt} = 0 \quad (3.3.2.5)$$

Equation (3.3.2.5) is known as Liouville's theorem and states that the density of representative points in phase space remains constant during the motion. In other words, the phase space occupied by the particles acts as an incompressible fluid in six dimensions. To understand this better consider the phase space density at a second point

$$\begin{aligned}
f(\vec{r} + \vec{v}dt, \vec{v} + \vec{a}dt, t + dt) &= f(\vec{r}, \vec{v}, t) + \frac{\partial f}{\partial t}dt + \vec{v} \cdot \frac{\partial f}{\partial \vec{r}}dt + \vec{a} \cdot \frac{\partial f}{\partial \vec{v}}dt + \dots \\
&= f(\vec{r}, \vec{v}, t) + \left(\frac{\partial f}{\partial t} + \vec{v} \cdot \nabla f + \vec{a} \cdot \nabla_v f \right) dt + \dots
\end{aligned}
\tag{3.3.2.6}$$

Liouville's theorem (Equation (3.3.2.5)) says that the coefficient of dt is zero. Thus the phase space densities at the two points differ by order dt^2 or higher. For the rate of change we need the difference divided by dt . But in the limit $dt \rightarrow 0$, that will vanish. This result means that if we were able to travel with a particle we would find that the phase space density in our neighbourhood will remain constant, i.e..

$$f(\vec{r} + \vec{v}dt, \vec{v} + \vec{a}dt, t + dt) = f(\vec{r}, \vec{v}, t) \tag{3.3.2.7}$$

Liouville's theorem says that the particle distribution function is constant along a particle orbit. In this formulation, particle orbit solutions are equivalent to solutions of the Vlasov equation. In other words, Liouville's theorem means that the distribution function (also called the phase space density), $f(\vec{r}, \vec{v}, t)$, when viewed at points along a particle's trajectory in phase space, is constant. Equation (3.3.2.7) can be rewritten as:

$$f(\vec{r}_0, \vec{v}_0, t_0) = f(\vec{r}_1, \vec{v}_1, t_1) \tag{3.3.2.8}$$

This important property may be utilised in plasma physics.

3.2.3 Distribution function calculation

In this research Liouville's theorem is used to evaluate distribution functions in the magnetosphere. To calculate the distribution function at a certain location \vec{r} in the magnetosphere, a three-dimensional array of initial velocities is specified in directions parallel to the magnetic field, \vec{V}_B , in the electric field direction, \vec{V}_E , and in the $\vec{E} \times \vec{B}$ or convection direction, \vec{V}_C . A velocity grid is chosen which divides each velocity direction into 31 bins from -2500 to +2500 km/s. Each initial velocity condition corresponds to a phase particle with coordinates (\vec{r}, \vec{v}_i) , where i is one of the 31^3 initial velocity components chosen. According to the foregoing theoretical considerations, each particle represents a system of the phase space ensemble, which moves along an orbit in phase space, carrying a piece of probability along with it. Each phase particle is used to derive a reduced distribution function $f(\vec{r}, \vec{v}_i)$ that depends only on the phase space coordinates of one pseudo-particle.

Thus the calculation begins with a single test particle (in this thesis ions are used) placed at its initial position in phase space (\vec{r}, \vec{v}_i) . This i th particle will have a value f_i assigned to its particular velocity, \vec{v}_i . However, before f_i can be known the trajectory must be integrated backward in time until the particle reaches an assumed source region. The velocity, \vec{v}_s , and position, \vec{r}_s at the source is known from integration. Thus the phase space density at the source, $f_s(\vec{r}_s, \vec{v}_s)$, may be computed according to some assumed dependence on (\vec{r}_s, \vec{v}_s) . For example, the source distribution may have a Maxwellian form. Liouville's theorem implies that the phase space density attached to \vec{r} and velocity \vec{v}_i is

$$f_i(\vec{r}, \vec{v}_i) = f_s(\vec{r}_s, \vec{v}_s) \quad (3.3.2.9)$$

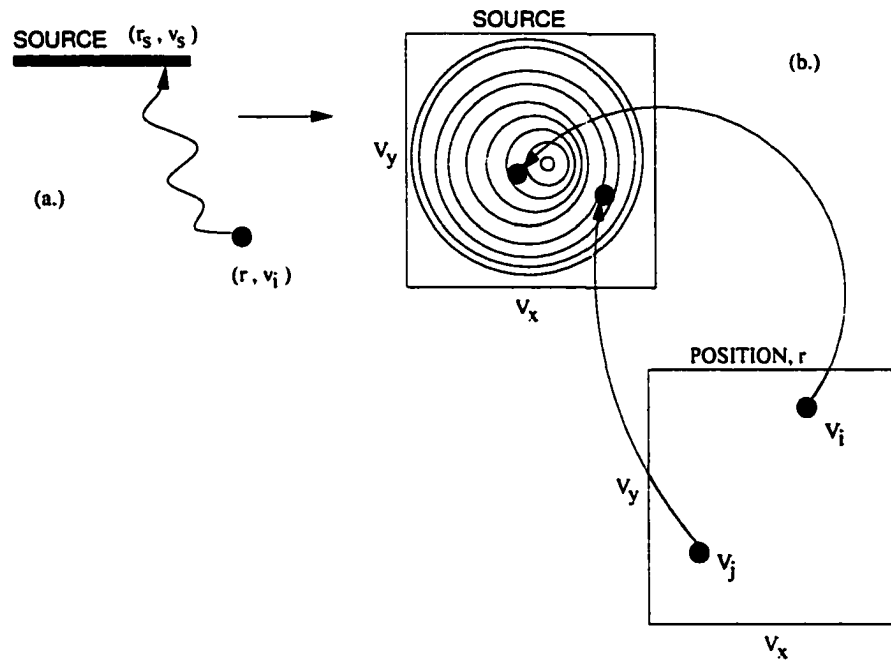


Figure 3.2: (a.) The cartoon illustrates how pseudo-particles, with initial position and velocity (r, v_i) move through space to a source region. (b.) The upper distribution function shows contours of constant phase space density. Numerous pseudo-particles are followed from unique initial locations in velocity space (lower distribution) to the source (upper distribution). Since the velocity distribution is known at the source, Liouville's theorem allows each initial pseudo-particle to be tagged with a known phase space density.

Otherwise, if the ion never reaches the source region, the phase space density for that initial condition is assigned the value zero:

$$f_i(\vec{r}, \vec{v}_i) = 0 \quad (3.3.2.10)$$

Zero's in phase space correspond to phase space holes in the velocity distribution functions. Figure 3.2a (left hand side) shows how a particle, with an initial position and velocity of (\vec{r}, \vec{v}_i) moves through space to the source boundary where it now has position and velocity (\vec{r}_s, \vec{v}_s) . After this integration the next particle of the ensemble of 31^3 particles, is placed at the same starting position \vec{r} , with a different initial velocity, \vec{v}_{i+1} , and integrated to the model boundary, and so on, until all the particles in the initial ensemble have reached the boundary. Even though the starting position, \vec{r} , is the same for all 31^3 particles, each has a unique phase space density assigned to it because each \vec{v}_i is unique. Figure 3.2b (right hand side) shows how two pseudo-particles move from their known position in velocity space to a new position in velocity space, but now at the source boundary. Once the particle reaches the source, where the distribution function is known, Liouville's theorem is applied, yielding the phase space density at the initial location in velocity space. Once the phase space density has been computed for all the initial conditions, i , the three-dimensional velocity space at position \vec{r} is completely filled. An array of phase space densities in velocity space exists at the starting position \vec{r} , and the full three-dimensional velocity distribution function at the position \vec{r} can be plotted. This distribution may also be used to compute moment integrations of the distribution function. For example, the number density for a particle species is defined as

$$n = \int f(\vec{v}) d^3v, \quad (3.3.2.11)$$

and the bulk velocity as

$$u_\alpha = \frac{1}{n} \int v_\alpha f(\vec{v}) d^3v, \quad (3.3.2.12)$$

where α is a coordinate index.

3.3 The plasma source

The location of the source is an important piece of information in any model. Once the distribution function has been constructed, one may vary parameters in the model and in the assumed source distribution, to try to model key features and asymmetries in the real distributions experimentally observed in space. Different source distributions can be used to represent different source regions. Several different source distributions that are considered in this study are discussed below. Plasma simulations in the next chapters use a combination of ionospheric, plasma mantle, and lobe sources

3.3.1 Plasma mantle source

A plasma mantle source has been frequently used in single particle studies [*Martin and Speiser, 1988; Martin et al., 1994*]. *Rosenbauer et al.* [1975] used HEOS 2 observations to characterise the plasma mantle. They found that the mantle features tailward bulk flow parallel to the magnetic field which was found to usually lie between 100 and 200 $km s^{-1}$.

They found that the mantle velocity distributions of protons showed a large temperature anisotropy, with $T_\perp/T_\parallel \approx 4$. Several prior studies have modelled the

mantle source with a flowing kappa distribution. At the source the distribution is given by [Martin and Speiser, 1988; Martin et al., 1994]

$$f(\vec{v}) = \frac{n\Gamma(\kappa + 1)}{\Gamma(\kappa - 1/2)(\pi\kappa\omega_0^2)^{3/2}} \left[1 + \frac{|\vec{v} - \vec{u}|}{\kappa\omega_0^2} \right]^{-(\kappa+1)} \quad (3.3.3.13)$$

where n is the number density, \vec{v} the particle velocity, \vec{u} the bulk velocity, κ the exponent, Γ the gamma function, and v_0 the most probable speed,

$$v_0 = \left[\frac{2k_B T_i}{m} \frac{\Gamma(\kappa - 1/2)}{\kappa\Gamma(\kappa - 3/2)} \right]^{1/2} \quad (3.3.3.14)$$

where k_B is Boltzmann's constant, m is the particle mass, and T_i is the temperature. Since a mantle source distribution is assumed, the following parameters were deemed appropriate, viz. $T_i = 0.38 \text{ keV}$, $n = 5 \times 10^4 m^{-3}$, $\vec{u} = (-350.0, 0) \text{ km/s}$. and $\kappa = 2$. One can vary the various parameters to remake the source distribution.

3.3.2 Ionospheric source

The form of the distribution function in the ionosphere is taken to be the upgoing portion of a bi-Maxwellian [Horwitz and Lockwood, 1985]. When the velocity parallel to the magnetic field is positive, $v_{\parallel} > 0$, then

$$f(v_{\perp}, v_{\parallel}) = 2n \left(\frac{m}{2\pi k_B} \right)^{3/2} \exp \left[\frac{-mv_{\perp}^2}{2k_B T_{\perp}} - \frac{-mv_{\parallel}^2}{2k_B T_{\parallel}} \right] / (T_{\perp} T_{\parallel})^{1/2} \quad (3.3.3.15)$$

otherwise

$$f(v_{\perp}, v_{\parallel}) = 0. \quad (3.3.3.16)$$

Here $k_B T_{\perp}$ and $k_B T_{\parallel}$ are the initial perpendicular and parallel thermal energies, n is the source density, and m is the particle mass. Various parameters are selected in the simulations, but unless otherwise stated the parameters will be, for O^+ : $n=1000 \text{ cm}^{-3}$, $k_B T_{\perp} = 10 \text{ eV}$, and $k_B T_{\parallel} = 1 \text{ eV}$, and for H^+ : $n=1000 \text{ cm}^{-3}$, $k_B T_{\perp} = 0.5 \text{ eV}$, and $k_B T_{\parallel} = 1 \text{ eV}$.

The ionospheric source location is chosen to be at altitudes below $r = 1.05 R_E$. In other words, the simulation is stopped whenever a particle is within 300 km of the surface of the earth, and that particle is assigned a phase space density given by equation (3.3.3.15).

3.3.3 Neutral sheet source

Onsager et al. [1991] and *Onsager and Mukai* [1996] used a neutral sheet ($B_x=0$) source population to create the PSBL distribution functions. Their model ion source comprises Maxwellian distribution functions in the neutral sheet with density decreasing linearly with distance downtail; 0.2 cm^{-3} at $X=-10 R_E$ and 0.08 cm^{-3} at $X=-90 R_E$. The neutral sheet temperature is 10 keV at $X=-10 R_E$ and 3 keV at $X=-90 R_E$.

3.3.4 Lobe source

Another one of the sources used by *Onsager et al.* [1991] and *Onsager and Mukai* [1996] was a Maxwellian lobe source. In this case the temperature is several to 10's of eV, and the density is very low $\approx 0.01 \text{ cm}^{-3}$. *Smets et al.* [1998] used a similar setup to study ion and electron distribution functions in the distant magnetotail.

3.4 Examples of the modelling technique

In this section, a well known and simple magnetotail model, including a strong crosstail current, is used to demonstrate the test particle simulation technique used in this thesis. Thereafter, in the following chapter, a new magnetotail model will be introduced and elucidated.

Distribution functions are constructed at various heights within the current sheet up to its edge at $Z = L_z$, where L_z is the current sheet half-thickness. Ion orbits (protons) are numerically integrated backwards in time from the observation location to some assumed source location. Numerical integration is implemented via a fourth order adaptive Runge-Kutta routine, with computations performed on a Silicon Graphics Power Challenge 10000, a DEC Alpha 1000, and Linux PC's. Once a particle has left the current sheet and is at least two gyroradii above or below $|Z| = L_z$ the integration is stopped. The integration time interval is limited to 45 minutes in order to catch singular cases of trapped orbits. When the particles have reached the boundary they may be tagged with any source distribution. Liouville's theorem, previously explained, is then invoked to compute the velocity distribution function at the observation location. Each distribution function is constructed by following the 31^3 particles from the desired observation point to the source boundary. This constitutes a $31 \times 31 \times 31$ velocity grid in cartesian velocity space. All the results that are presented consider the source to be a tailward flowing kappa distribution modelling plasma mantle ions, as described in the previous sections. Since a mantle source distribution is assumed, the following parameters were deemed appropriate, viz. $T_i = 0.38$ keV, $n = 5 \times 10^4 m^{-3}$, $\vec{u} = (-350, 0, 0)$ km/s. and $\kappa = 2$. The electric field was set to be constant in the duskward, or y-cartesian, direction with a value 0.25×10^{-3} V/m.

3.4.1 Modified Harris sheet

The simple Harris sheet magnetic field is given by the x-component of the following field, with all other components zero:

$$B_x = B_0 \tanh\left(\frac{z}{L_z}\right)$$

$$B_y = 0$$

$$B_z = B_n$$

Adding a nonzero constant B_z to the Harris field results in a modified Harris sheet magnetic field. In this work I have used $B_0=20$ nT, $B_n=1.1$ nT, and $L_z=0.05 R_E$.

3.4.2 Distribution function results

Lyons and Speiser [1982] have shown that a Harris current sheet with constant B_z and uniform electric field $E = E_y$ produces earthward field aligned beams at the edges of the current sheet. This corresponds to the model used here. Figure 3.3a shows the distribution function at the edge of the current sheet (i.e. $Z = L_z$). This slice is taken in the plane in which particles have zero velocity in the electric field direction; i.e. $V_E = 0$. The ordinate of this figure corresponds to velocities in the magnetic field direction, and the abscissa is in the $\vec{E} \times \vec{B}$ convection direction. The magnetic field at this observation location was $\vec{B} = (15.2, 0, 1.1)$ nT. Hence the \vec{V}_B direction is predominantly earthward (positive X-direction), and the \vec{V}_C direction is towards the neutral sheet.

Figure 3.3b shows the distribution function at $Z = 0.5L_z$. The earthward beam is still present deeper in the current sheet. One difference between Figures 3.3a and 3.3b is the small gaps in Figure 3.3a near $\vec{V}_B = 0$ and on either side of $\vec{V}_C = 0$.

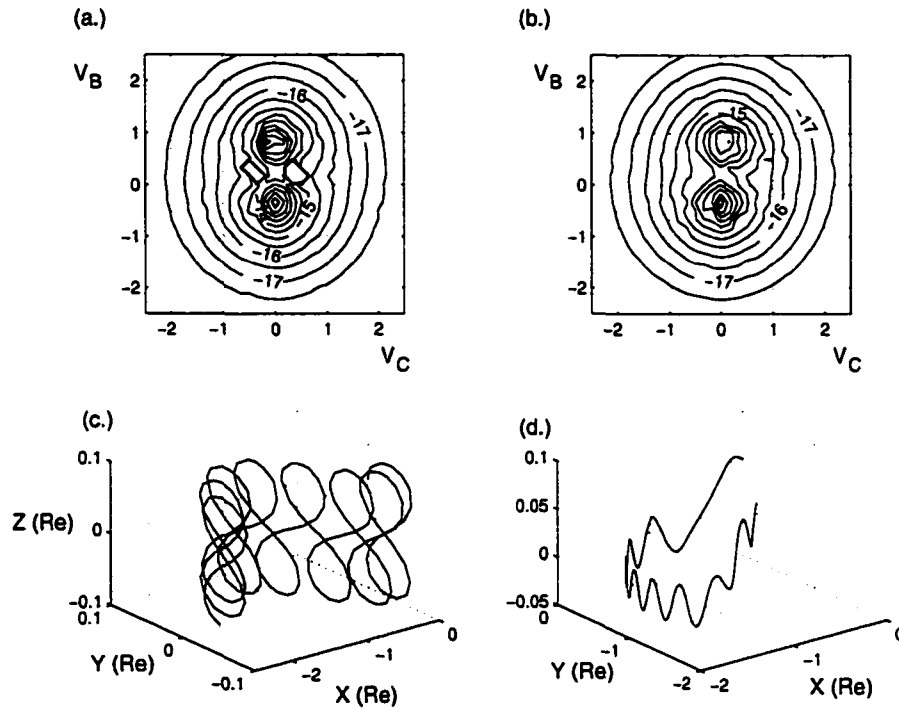


Figure 3.3: Model ion velocity distribution functions in the $V_B - V_C$ plane, and at the $V_E = 0$ cut. Velocities are in thousands of km/s . The contours are in intervals of $10^{-0.5}$ from $10^{-17.5} s^3/m^6$. (a.) This calculation is for $z = L_z$; (b) for $z = 0.5L_z$; (c) an example of a singular case of a proton's orbit when it is trapped in the current sheet and never reaches the source. These kinds of orbits comprise the phase space gaps found in (a) and have a figure eight shape; and (d) a typical Speiser orbit for a proton that forms part of the field-aligned beam at the edge of the current sheet.

These phase space *holes* correspond to singular cases of trapped proton orbits which are permanently trapped in the current sheet. Figure 3.3c shows an example of one such trapped orbit. This orbit has a figure eight appearance which is clearest in the $Y - Z$ projection. It is shown in three dimensions, and the figure eight pattern is still very clear. The orbit type is sensitively dependent on the ratio of the square root of the magnetic field radius of curvature to the particle gyroradius. This parameter, known as the κ -parameter, is a constant along the tail for the modified Harris sheet, and this 10 keV proton has $\kappa = 0.037$. Other models also produce similar orbits: for example, *Larson and Kauffman* [1996] give an example of a figure eight orbit for their model of the magnetotail (their Figure 5). They found that particles with these orbits remained trapped for longer than other particles. The formation of phase space gaps has been noted in previous simulation studies which use a preselected source population [*Ashour-Abdalla et al.*, 1991]. *Holland and Chen* [1991] showed that phase space boundaries will persist in the presence of pitch angle and energy scattering in magnetotail fields, and *Kauffman and Lu* [1993] note that all current sheets characterised by a very small κ must have phase space depletions.

The field aligned beam, with a maximum phase space density at a velocity $V_B = 800$ km/s, was found to comprise ions that behaved in a qualitatively similar manner. These ions are convected by the electric field in the direction normal to the magnetic field lines towards the earth and towards the neutral sheet. They undergo Speiser motion and acceleration in the current sheet resulting in the earthward streaming distribution at the outer edge of the PSBL. An example of one such orbit is shown in Figure 3.3d.

CHAPTER 4

The magnetotail model

4.1 Introduction

In a way similar to other explorers, space physicists create maps of the magnetosphere in order to understand it, and provide a knowledge base to aid future exploration. The most widely used magnetospheric models are those developed by N.A. Tsyganenko and his collaborators [*Tsyganenko and Usmanov*, 1982; *Tsyganenko*, 1987; *Tsyganenko*, 1989; *Tsyganenko and Peredo*, 1994; *Tsyganenko*, 1996]. Of these, the most complete was produced by *Tsyganenko* [1996] (hereafter referred to as T96).

Whereas the models prior to T96 did not have a pre-defined magnetopause and were calibrated exclusively by the K_p index, the most recent model (i.e. T96) explicitly includes (i) the solar-wind-controlled magnetopause, (ii) Region 1 and 2 Birkeland currents, and (iii) the interconnection of the magnetospheric and solar wind fields at the boundary. T96 is a statistical model based on magnetic field data collected by 11 spacecraft, covering the period from 1966 to 1986 [*Fairfield et al.*, 1994]. T96 represents the sum of the magnetic effects of the separate components of the total magnetospheric magnetic field, viz. the magnetopause current system, the ring current, the tail current sheet, the Region 1 and 2 Birkeland current systems, and the interconnection term due to partial penetration of the IMF into the magnetosphere. Each component was parameterised by its own set of input parameters, and the net model field was fitted by least squares to the entire data set of over 45000 grid

points. The input parameters to the T96 model are the solar wind dynamic pressure, DST-index, IMF B_y and B_z , and the dipole tilt angle.

At present T96 is too computationally intensive to be the primary magnetic field model in a test particle study. Furthermore, it is a global magnetospheric model whereas in this study only a limited region of the magnetosphere is being considered, viz. the magnetotail. In addition to this, T96's statistical nature implies that thin current sheets or other sharp magnetic field gradients, cannot be accurately resolved, and will be spread out; thus, it is not appropriate for studies of thin current sheets. However, since T96 is the averaged result of numerous actual satellite measurements, it can be a helpful guide in developing a simpler model. This is the procedure followed here.

4.2 Key factors in the magnetotail model

In this dissertation the test particle method and Liouville mapping are employed to compute velocity distribution functions (VDF's) during times when the magnetotail is significantly stretched, such as during the substorm growth phase. Since highly nonadiabatic ion motion in the magnetotail cannot be described by the guiding centre approximations, the complete Lorentz equation of motion is used for all particle tracing. Many calculations are needed so the magnetic field model must be selected to minimize computing time, while being as realistic as possible.

The new magnetotail model developed attempts to mimic the magnetotail during times when it has a stretched configuration. Since it is well known that the magnetotail stretches more than average during the growth phase of a magnetospheric

substorm, aspects of the growth phase that are important in causing enhanced stretching of the magnetotail are considered. It is worthwhile to repeat salient features of the growth phase currents and fields. First of all, during a substorm growth phase, the near-earth crosstail current can thin to fractions of an R_E [Sergeev *et al.*, 1993; Sanny *et al.*, 1994; Kubyshkina *et al.*, 1999]. At the same time the crosstail current greatly intensifies in the near-earth region [Kaufmann, 1987]. The current intensification is restricted in radial extent, and azimuthally to within a few hours around magnetic midnight [Baker and McPherron, 1990; Iijima *et al.*, 1993; Baker *et al.*, 1993]. These changes in the crosstail current result in the magnetic field becoming very weak and taillike in the midplane [Kokubun and McPherron, 1981; Pulkkinen *et al.*, 1992, 1999; Nakai *et al.*, 1997], and lead to a region of weak magnetic field in the near earth neutral sheet region [Erickson, 1984; Hau *et al.*, 1989; Hau, 1991; Lui *et al.*, 1992; Sergeev *et al.*, 1993, 1996]. As well, changes in current sheet structure are expected to lead to enhanced ionospheric precipitation, as particle adiabaticity is broken close to the earth [Büchner and Zelenyi, 1989]. Such behaviour is not restricted only to growth phase conditions, as determined by ground based instruments, but may occur during ostensibly quiet times.

Instead of modifying the multiparameter Tsyganenko models, a simpler magnetic field model that has fewer components is used. As mentioned before, the Tsyganenko models calculate a statistical crosstail current that represents an average over all configurations of the magnetosphere. There is good reason, therefore, to expect that these models do not adequately fit substorm growth phase, when the magnetotail is very stretched and extremely thin current sheets exist. Modifications that are required to fit these models to growth phase bear out this conviction [Pulkkinen *et al.*, 1991, 1992, 1994, 1998 and Lu *et al.*, 1999]. The model presented below has the advantage of simplicity, thus making it easier to understand the physics of the current

sheet during the growth phase. It comprises a dipole field, an equilibrium tail component, and an azimuthally and radially confined weak magnetic field region (WFR). The coordinate system is centred on the earth, with the X -axis from the earth to the sun, the Z -axis anti-parallel to the dipole moment, and the Y -axis perpendicular to the other two axes. All three modular components of the model are used to build up the final configuration

$$\vec{B}(\vec{r}) = \vec{B}_{Dipole}(\vec{r}) + \vec{B}_{Tail}(\vec{r}) + \vec{B}_{WFR}(\vec{r}) \quad (4.4.2.1)$$

Each of the components is divergence free, and so the entire magnetic field model is divergence free.

4.2.1 The dipole field

The vector magnetic potential of a dipole is given by

$$\vec{A}_{Dipole}(\vec{r}) = \frac{M}{r^3}(y\hat{x} - x\hat{y}) \quad (4.4.2.2)$$

where \vec{M} is the dipole moment and $r^2 = x^2 + y^2 + z^2$ is the radius from the centre of the earth. The earth is at the centre of the coordinate system, and the z -axis is antiparallel to \vec{M} and the x -axis is towards the sun.

$$\vec{M} = -M\hat{z} = -31100\hat{z} nTR_E^3 \quad (4.4.2.3)$$

and the resulting magnetic field is

$$\vec{B}_{Dipole}(\vec{r}) = -\frac{3Mxz}{r^5}\hat{x} - \frac{3Myz}{r^5}\hat{y} - \frac{M(3z^2 - r^2)}{r^5}\hat{z} \quad (4.4.2.4)$$

4.2.2 The equilibrium tail model

A simple model of a plasma sheet formed at the interface of two regions of opposing magnetic field would be useful to study the nonlinear dynamics of single particle trajectories. In the midtail region a two-dimensional equilibrium tail field model would be convenient for studying the neutral sheet. Equilibrium models represent magnetic fields that are derivable from approximately isotropic particle distributions. The most widely used magnetotail models for such studies are variations on the exact solution to the Vlasov-Maxwell equations by *Harris* [1962]. The magnetic field for the Harris model is

$$\vec{B}_{Harris}(\vec{r}) = B_0 \tanh\left(\frac{z}{L_z}\right)\hat{x} \quad (4.4.2.5)$$

where B_0 corresponds to the lobe field in a magnetotail model, and L_z is the parameter controlling the half-thickness of the central plasma sheet (CPS). When a weak uniform magnetic field, B_n is added, the new model is called the modified Harris model. Both the Harris model and the modified Harris model have the same associated crosstail electric current

$$\vec{J}_{Harris}(\vec{r}) = \frac{B_0}{\mu_0 L_z} \text{sech}^2\left(\frac{z}{L_z}\right)\hat{y} \quad (4.4.2.6)$$

In this thesis *Zwingmann's* [1983] two-dimensional equilibrium tail field is used. The Zwingmann tail model has a vector potential

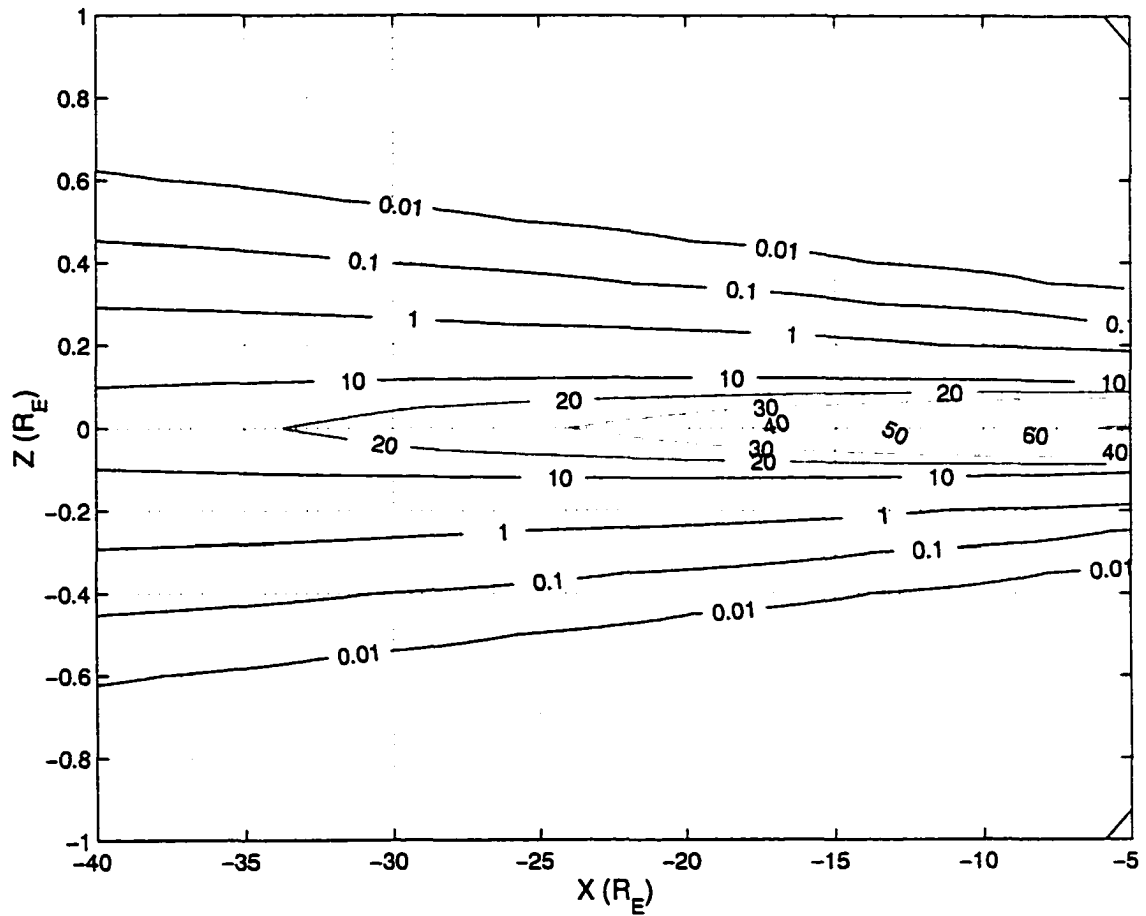


Figure 4.1: Contour plot in the noon-midnight meridian showing values of the crosstail electric current density, J_y^{Tail} in units of nA/m^2 . This azimuthal current is positive in the westward direction (dawn-to-dusk).

$$\vec{A}_{Tail}(\vec{r}) = B_0 \ln \left[\frac{\cosh(F(x) \frac{z}{L_z})}{F(x)} \right] \hat{y} + O(\epsilon^2) \quad (4.4.2.7)$$

where the function $F(x)$ is a slowly varying function of x that decreases with distance from the earth, and is chosen as

$$F(x) = \left(1 - \frac{\epsilon x}{L_z \nu}\right)^{-\nu} \quad (4.4.2.8)$$

The associated magnetic field calculated from the curl of the vector potential, \vec{A} , is given by

$$\begin{aligned} B_x^{Tail} &= B_0 F(x) \tanh(F(x) \frac{z}{L_z}) \\ B_y^{Tail} &= 0 \\ B_z^{Tail} &= B_0 L_z \frac{\partial_x F(x)}{F(x)} \left[1 - F(x) \frac{z}{L_z} \tanh(F(x) \frac{z}{L_z})\right] \end{aligned} \quad (4.4.2.9)$$

and the electric current for this case is

$$\begin{aligned} J_x^{Tail} &= 0 \\ J_y^{Tail} &= -\frac{B_0}{\mu_0} \left\{ \frac{F^2(x)}{L_z} \operatorname{sech}^2(F(x) \frac{z}{L_z}) - L_z \frac{\partial_{xx} F(x)}{F(x)} \left[1 - F(x) \frac{z}{L_z} \tanh(F(x) \frac{z}{L_z})\right] \right. \\ &\quad \left. + L_z \left(\frac{\partial_x F(x)}{F(x)}\right)^2 \left[1 + F^2(x) \frac{z^2}{L_z} \operatorname{sech}^2(F(x) \frac{z}{L_z})\right] \right\} \\ J_z^{Tail} &= 0 \end{aligned} \quad (4.4.2.10)$$

Figure 4.1 shows the crosstail current sheet distribution in the noon-midnight meridian. The current sheet intensifies and thins nearer the earth. In this figure the following values were chosen for the parameters in the Zwingmann tail model; $B_0 = 50nT$,

$L_z = 0.05R_E$, $\nu=1.25$, and $\epsilon=0.002$. The electric current density from the Zwingmann field, computed from $\nabla \times \vec{B}$, flows entirely from dawn to dusk (Y -direction) across the magnetotail. Current sheet half-thickness, L_z , is the parameter which has the strongest influence on the model topology. In the following section real magnetospheric data will be used to find a thickness that is reasonable for the growth phase.

4.2.3 Weak field region

The final component to the model is a three-dimensional magnetic structure that creates a depression, or weak magnetic field region (WFR), near the earth. The observations of *Sergeev et al.* [1993], showed that around $11 R_E$ during growth phase. the normal magnetic field in the neutral sheet was very small (≈ 1 nT). These observations imply that additional large scale current systems, and/or local current flow cause the equatorial B_z to be very small. *Nakai and Kamide* [1994] suggest that region 1 field-aligned currents [*Donovan*, 1993] and/or the neutral sheet current meandering earthward in a localised region near the midnight sector [*Baker and McPherron*, 1990] can be plausible candidates as such additional current systems. Whatever its cause, the WFR is a localised magnetic field perturbation, observed in the near-earth region during the growth phase.

The equations describing the magnetic field of the model WFR depression are given by

$$\begin{aligned} B_x &= 0 \\ B_y &= B_p L_y \operatorname{sech}\left(\frac{\bar{x}}{L_y}\right) \tanh\left(\frac{y}{L_y}\right) \partial_z G(z) \end{aligned} \tag{4.4.2.11}$$

$$B_z = B_n - B_p \operatorname{sech}\left(\frac{\bar{x}}{L_y}\right) \operatorname{sech}^2\left(\frac{y}{L_y}\right) G(z)$$

where $\bar{x} = x + 10$, $B_p = 28.45 \text{ nT}$, $B_n = 1 \text{ nT}$, $L_y = 3^{1/2} R_E$, and the function $G(z)$ is given by

$$G(z) = \left(1 + \frac{z^2}{L_y^2}\right)^{-1/3} \quad (4.4.2.12)$$

Just as for the equilibrium tail model, this component is comprised of combinations of hyperbolic functions. The WFR is so named because it creates a depression in the magnetic field around $X = -10 R_E$. It is constructed to simulate the observation, mentioned at the start of this section, that the growth phase current sheet is enhanced in a radially and azimuthally confined region. Its effect is to cause enhanced stretching of magnetic field lines in the near-earth region. This is in accord with various theoretical models that predict a region of small B_z will form in the intermediate zone between dipolelike and taillike magnetic fields under the action of a dawn-to-dusk electric field [Erickson, 1984; Hau et al., 1989; Hau, 1991]. The resultant electric current system is defined by

$$\begin{aligned} J_x^{WFR} &= \frac{B_p}{\mu_0} \left\{ \frac{2}{L_y} G(z) \operatorname{sech}\left(\frac{\bar{x}}{L_y}\right) \operatorname{sech}^2\left(\frac{y}{L_y}\right) \tanh\left(\frac{y}{L_y}\right) - L_y \operatorname{sech}\left(\frac{\bar{x}}{L_y}\right) \tanh\left(\frac{y}{L_y}\right) \partial_{zz} G(z) \right\} \\ J_y^{WFR} &= -\frac{B_p}{\mu_0} \left\{ \frac{G(z)}{L_y} \operatorname{sech}\left(\frac{\bar{x}}{L_y}\right) \tanh\left(\frac{\bar{x}}{L_y}\right) \operatorname{sech}^2\left(\frac{y}{L_y}\right) \right\} \\ J_z^{WFR} &= -\frac{B_p}{\mu_0} \left\{ \operatorname{sech}\left(\frac{\bar{x}}{L_y}\right) \tanh\left(\frac{\bar{x}}{L_y}\right) \tanh\left(\frac{y}{L_y}\right) \partial_z G(z) \right\} \end{aligned} \quad (4.4.2.13)$$

The WFR equatorial current system flows in an almost circular pattern, as shown in Figure 4.2. This is in agreement with the findings of Iijima et al. [1993] who found that during the growth phase, complicated electric currents arise which include

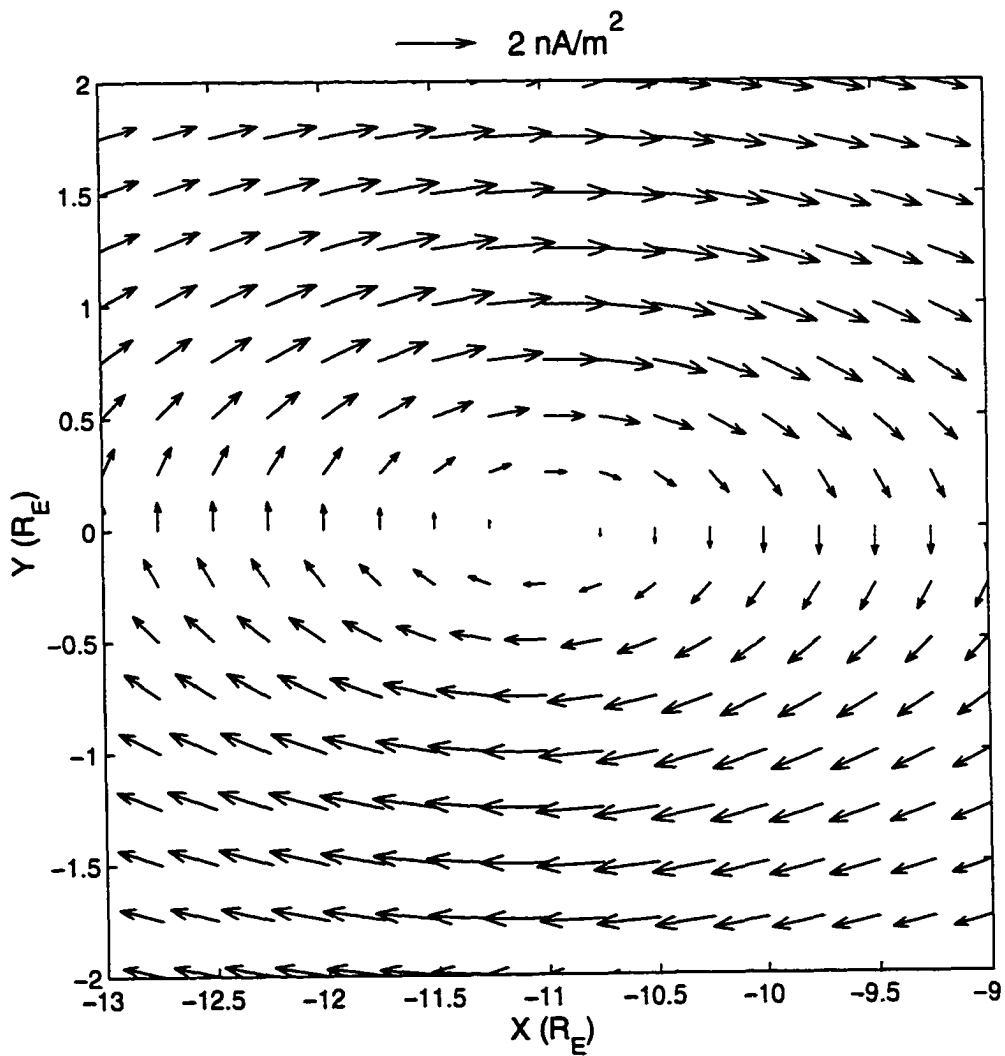


Figure 4.2: Vectors in the equatorial plane showing the variation of the crosstail electric current density for the model WFR.

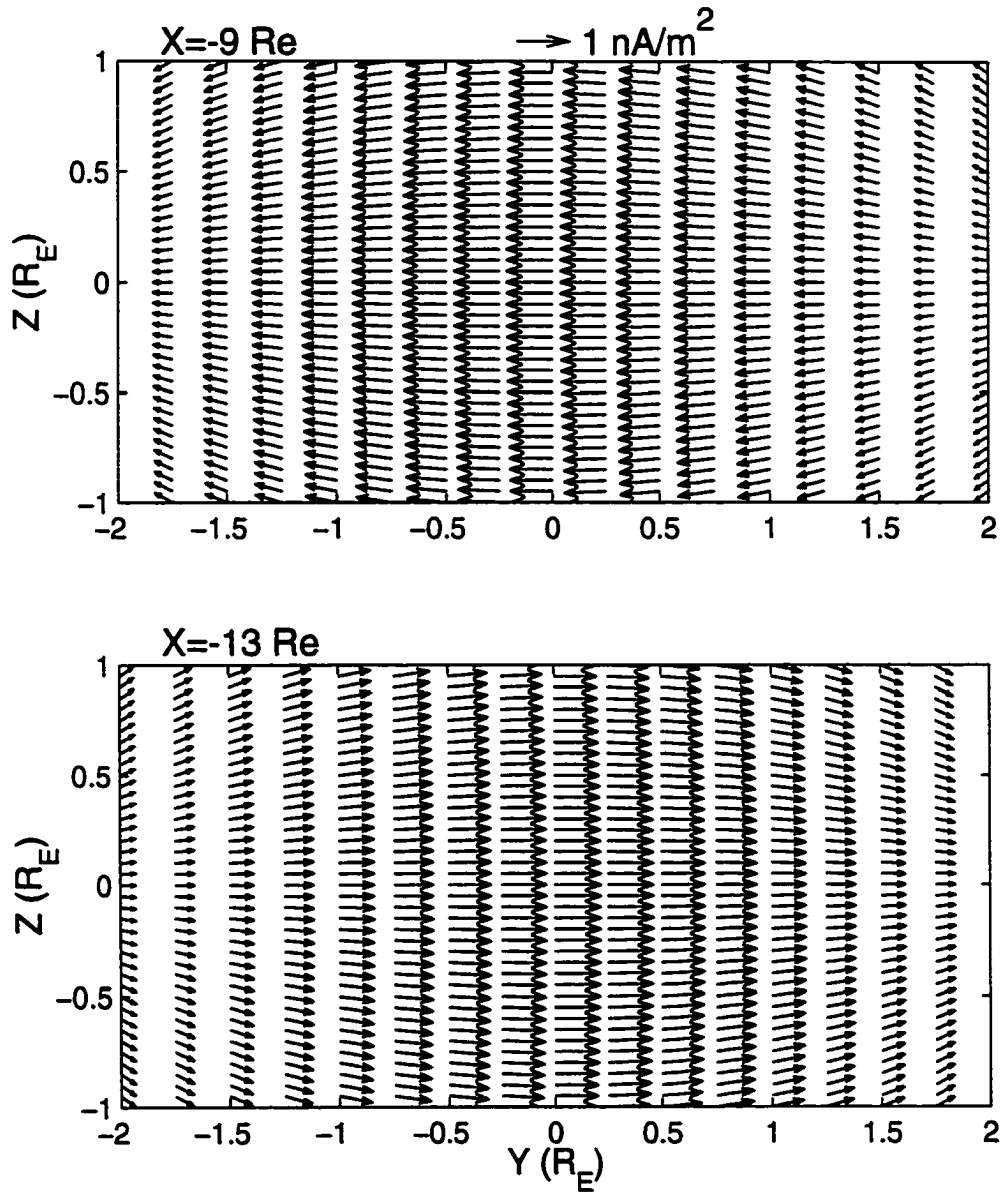


Figure 4.3: Vectors at $X = -9 R_E$ (top) and $X = -13 R_E$ (bottom) showing the variation of the cross-tail electric current density for the WFR.

an equatorial azimuthal current loop. The loop flows in the clockwise sense, with its tailward side enhancing the crosstail current, and the earthward side decreasing the crosstail current. The model WFR has the same effect; in the noon-midnight meridian it will reduce the net azimuthal crosstail current close to the earth. This reduction in current corresponds to the "current trough" signature reported by *Nakai et al.* [1997]. The WFR also tends to increase the azimuthal current slightly downtail of the "current trough", in accordance with the observations of *Iijima et al.* [1993]. In the equatorial plane, the radial component of the current flows towards the earth in the late evening to premidnight sector and flows away from the earth in the midnight to morning sector.

Figure 4.3 shows the current density in the $Y-Z$ plane at $X=-9 R_E$ and $-13 R_E$. The current density is greatest in the neutral sheet and gradually decreases with distance from the neutral sheet. The bulk of the current flows between $|Z| \leq 1 R_E$. The model ensures that current continuity is satisfied, i.e. $\nabla \cdot \vec{j}^{WFR} = 0$.

4.3 Constraining the magnetic field model

The parameter most strongly affecting particle motion in the magnetotail is undoubtedly the current sheet half-thickness, L_2 . Another important parameter is the location of the WFR. In this section the model will be constrained via the use of various statistical data, and the results of previous observational studies. A new technique will be demonstrated whereby auroral proton precipitation data will be used as a proxy to determine reasonable current sheet thicknesses during the growth phase. As well, comparisons will be made between the model, thus obtained, and T96.

4.3.1 Constraint from the neutral sheet magnetic field

Since the normal component of the magnetic field in the neutral sheet, B_z , is critical to energisation processes resulting from nonadiabatic particle motion, careful attention must be paid to the selection of this parameter. The T96 model was used as a rough guide, but there are questions as to how well it represents B_z at midnight. As well, the data used to fit the T96 model were not selected according to substorm phase. This means that the model tail represents an average over both the stretched configuration that is seen before a local substorm expansion and the more dipolar configuration seen after expansion. It is therefore not clear that the model will provide a good representation of the earth's magnetic field at any one time. Accordingly, wherever more accurate or appropriate data are available these have been used to test the model in a more realistic fashion.

The existence of the WFR has been previously justified in terms of various theoretical models [Erickson, 1984; Hau *et al.*, 1989; Hau, 1991], and observational studies [Lui *et al.*, 1992; Sergeev *et al.*, 1993]. The depth and location of the minimum of the WFR in the full model - comprising the dipole, tail and WFR - is almost independent of current sheet half-thickness L_z . For this reason it was the first parameter to be set in the new model. The chosen position for the WFR, viz. about $X = -10 R_E$, is justified below in terms of observational data. The model NS magnetic field is not a fit to the observational data presented. Rather, the comparison of the model with observational data is intended to demonstrate that the new model is reasonable.

In the study by Rostoker and Skone [1993], AMPTE, ISEE, and IMP 8 data were selected at times when clear neutral sheet crossings were taking place. Using

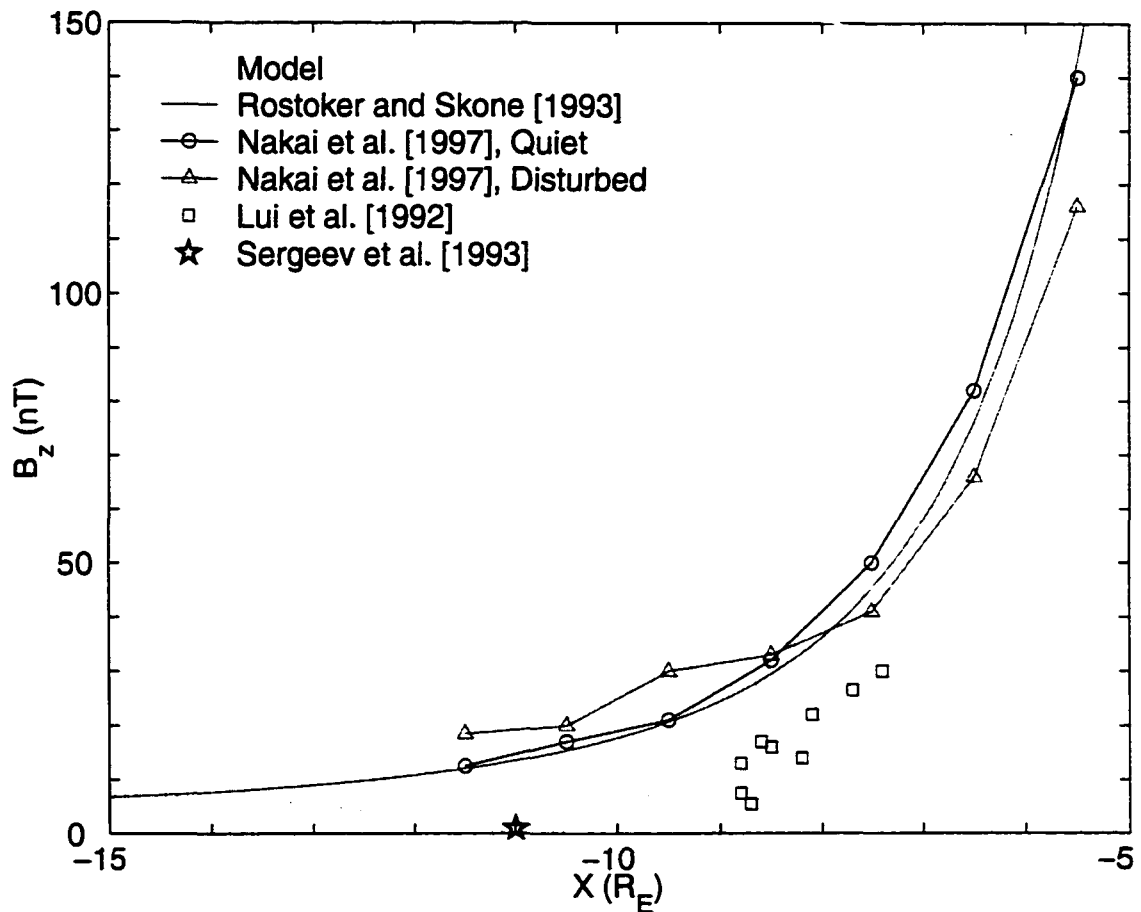


Figure 4.4: Model magnetic field values in the neutral sheet compared to various satellite measurements. The dotted line indicates the model magnetic field, the solid line is the empirical function of *Rostoker and Skone* [1993], calculated irrespective of substorm phase. The circles and triangles indicate B_z during disturbed and quiet periods from the measurements of *Nakai et al.* [1997]. The squares are the values from *Lui et al.* [1992], measured just prior to the onset of magnetic field dipolarisation, the single star is for the growth phase measurements at $X = -11 R_E$ by *Sergeev et al.* [1993].

these data they constructed an analytical representation of B_z as a function of down-tail position. In Figure 4.4 magnetic field values in the neutral sheet are compared for the new model and the empirical function of *Rostoker and Skone* [1993] (solid curve), as well as other statistical observations of neutral sheet magnetic field. The model field is a good fit of the *Rostoker and Skone* function in the regions tailward of $\sim 14 R_E$. Near $X = -11 R_E$, which is the intermediate region between dipole-like and tail-like magnetic fields, the new magnetic field model has a depression not found in that statistical model, and is larger within geostationary orbit. As with T96, the statistical model of *Rostoker and Skone* will tend to average out the extremes of magnetic field behaviour, so not too much importance should be placed on this discrepancy. This is especially so in light of experimental observations of radially confined regions of small normal magnetic field during times when the magnetotail geometry is stretched [*Sergeev et al.*, 1993].

Also included in this figure are the statistical observations of *Nakai et al.* [1997] representing equatorial B_z during quiet and disturbed conditions. These data show that during quiet times the magnetic field is larger than the *Rostoker and Skone* curve, whereas for disturbed times these data are smaller in the near-earth, but larger beyond geostationary orbit. Within the standard deviations of these data (not shown) their results are the same as for *Rostoker and Skone*. The equatorial B_z data from *Lui et al.* [1992] (squares) and *Sergeev et al.* [1993] (star) are the most useful, for they were specifically measured during case studies of the late growth phase, and are in much better agreement with the new model in the intermediate region between dipole-like and tail-like magnetic fields. These data show that, during the growth phase regions of small normal magnetic field (B_z) can occur in the near-earth. The minimum in the model magnetic field occurs around $X = -11 R_E$, and the size of the minimum can be varied via the parameter B_p in equation (4.4.2.12).

4.3.2 Constraint from proton precipitation

The Canadian Auroral Network for the OPEN Program Unified Study (CANOPUS) is a large-scale array of remote sensing equipment monitoring the high latitude ionosphere from the north-central to the north-west portion of North America. CANOPUS includes an array of four meridian scanning photometers (MSP) [Rostoker *et al.*, 1995] which are capable of scanning auroral emissions at various wavelengths. With the MSP one can monitor key auroral wavelengths that provide information useful, for example, in identifying the locale of specific auroral activations. The importance of these tools is appreciated as one considers that any region of the magnetosphere maps to the ionosphere along magnetic field lines. Such a mapping means that knowledge of where the particles and currents are in the ionosphere can give information about the state of the magnetosphere. For example, Samson *et al.* [1992] and Samson [1994] used CANOPUS MSP and low altitude satellite measurements to demonstrate that substorm expansive phase intensification starts near the earth, at no more than 8-10 R_E behind the earth.

In the earth's magnetotail, particles may not conserve the first adiabatic invariant due to significant magnetic field variations on the scale of the particle gyroradius. The kappa parameter, defined by Büchner and Zelenyi [1987], is useful in characterising the non-adiabatic particle behaviour. The parameter is defined by

$$\kappa = \sqrt{\frac{R}{\rho}}, \quad (4.4.3.14)$$

where R is the magnetic field line radius of curvature, and ρ is the particle gyroradius measured in the current sheet. The dependencies in kappa show that the type of particle motion (viz. adiabatic and chaotic) is dependent on both the magnetic field

geometry and particle energy. Magnetotail models have strongly curved field lines and the magnetic field component normal to the current sheet can become very small. When the radius of curvature of the magnetic field at the current sheet becomes comparable to the particle gyroradius, the particle is pitch angle scattered. In the distant tail $\kappa \ll 1$. *Ashour-Abdalla et al.* [1994] showed that meandering motion in this regime can lead to the formation of a thin current sheet. On the other hand, close to the earth where the dipole field is stronger, the parameter κ can be much larger than unity, and the particle motion is adiabatic. In between, at the transition between taillike and dipolelike field configurations, plasma sheet ions can have variable κ values. *Zelenyi et al.* [1990] demonstrated that for $1 \leq \kappa \leq 3$ near-earth plasma sheet ions may become untrapped. Recently, *Delcourt et al.* [1996] numerically verified that ions corresponding to κ values between 1 and 3 can be pitch angle scattered out of the current sheet, a fraction of which may enter the loss cone and precipitate into the ionosphere. If the magnetic field is very stretched, the fraction entering the loss cone can be quite significant [*Lyons and Speiser*, 1982]. *Liu et al.* [1998] quantified this effect using theoretical models of a stretched near-earth current sheet.

One may use a magnetic field model to map auroral luminosity from the ionosphere to the magnetosphere. This is done by locating the luminosity region of interest, and then following the magnetic field line that threads this region to its position in the current sheet. However, this method does not address the question of what mechanism scatters the particles out of the current sheet so that they can precipitate into the ionosphere along the magnetic field line. What is proposed here is just the opposite - a mapping from the magnetotail to the ionosphere. First, positions in the magnetotail are located where pitch angle scattering of protons can be very important (i.e. $1 \leq \kappa \leq 3$). Then these regions are mapped to the ionosphere, along

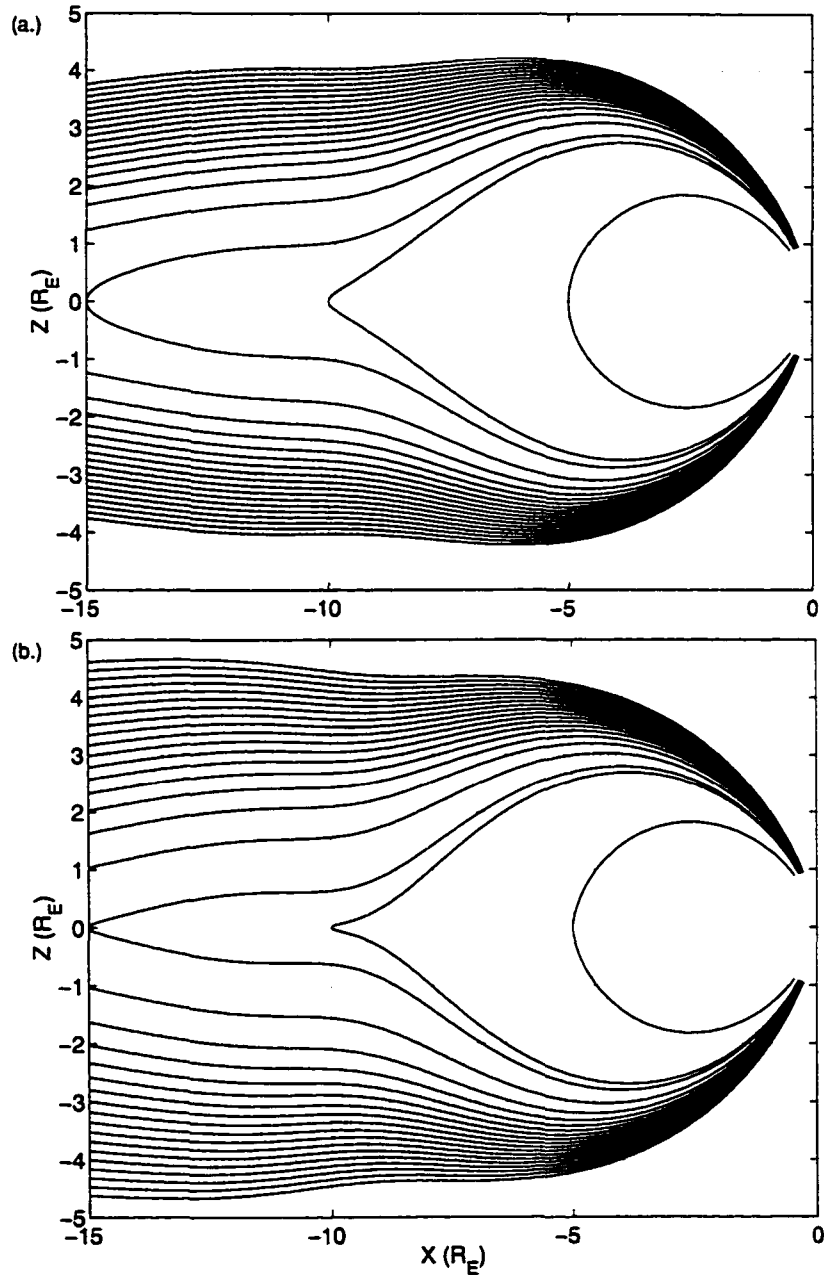


Figure 4.5: Model magnetic field lines in the noon-midnight meridian for current sheet half-thickness (a.) $L_z = 1R_E$ and (b.) $L_z = 0.05R_E$. In the latter case the thinner current sheet is evidenced by the decreased magnetic field line radius of curvature.

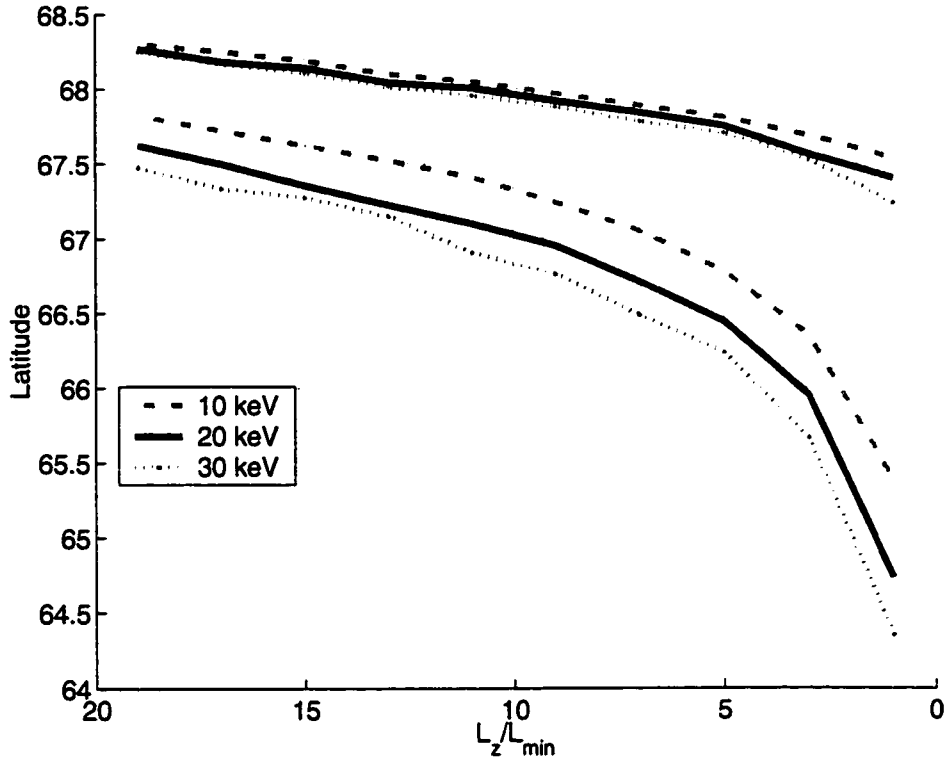


Figure 4.6: Model predictions for the regions of proton precipitation in the ionosphere. Precipitation is assumed to occur in the region between the high- and low-latitude borders. The ordinate is invariant latitude in degrees, and the abscissa is the model current sheet half-thickness, normalised to $L_{min} = 0.05 R_E$. These curves were computed by calculating the regions in the magnetotail where 10, 20, and 30 keV protons achieve $1 \leq \kappa \leq 3$, and then mapping these regions to the ionosphere. The parameter κ is defined in Equation 4.4.3.14.

magnetic field lines, where they correspond to proton auroral precipitation. Ideally this mapping would correspond to the real luminosity, measured by the MSP. However, the mapping problem depends on numerous independent parameters not known accurately. For example, the κ -parameter is sensitive to particle energy, current sheet thickness, and the normal component of the magnetic field in the crosstail current sheet region. The 486.1 nm (H_β) auroral emissions are used, for which the average energy of the precipitating protons, based on a comparison of DMSP and H_β data, is about 20 keV [Samson et al., 1992]. In order to understand the dynamics and evolution of the thin current sheet only the parameter related to the crosstail current sheet thickness will be allowed to vary. In this way it is possible to find reasonable model current sheet thicknesses, observed during growth phase. Samson et al. [1992] showed that the 486.1 nm (H_β) emissions, can be used to delineate the earthward edge of the plasma sheet. Thus in addition to the current sheet thickness, it is possible to derive the position of the inner edge of the plasma sheet from the equatorward edge of the H_β emissions.

In his paper, Kaufmann [1987] showed that a requirement of growth phase was enhanced stretching of field lines, particularly in the near-tail region. He achieved the requisite taillike field configuration at $\sim 6.6 R_E$ by using a field model comprising a dipole field, and a system of three infinitely thin current sheets in the tail. The new magnetic field model is only slightly more complex, and reproduces field geometries similar to those in Kaufmann [1987]. Figure 4.5 shows magnetic streamlines for (a.) thick ($L_z = 1R_E$) and (b.) thin ($L_z = 0.05R_E$) crosstail half-thickness parameter. Thinning of the current sheet is evidenced by the decreased magnetic field radius of curvature in Figure 4.5b. These two figures are similar to Figures 2 and 3 from Kaufmann [1987]. The magnetic field model may be used to predict where in the

ionosphere regions of auroral proton precipitation will occur. In light of the observational constraints for H_{β} proton energies of 10, 20, and 30 keV are used to calculate the κ -parameter in the crosstail current sheet. Thus the modelling is restricted to an energy range close to the average. Figure 4.6 shows the predicted latitudes of auroral proton precipitation, plotted against current sheet thickness parameter, L_z . The borders for the 10 keV protons are shown as dot-dashed lines, 20 keV are solid, and 30 keV are dotted. In all cases it is clear that, as the current sheet thins the precipitation region moves equatorward. As well, the lower border of the precipitation moves equatorward at a faster rate for smaller current sheet thicknesses. This lower precipitation border corresponds to the inner edge of the plasma sheet [Samson *et al.*, 1992]. Least squares fitting of these data to the actual MSP measurements will now be used to see what values of L_z result in the best fits of auroral luminosity regions.

March 9, 1995

The interval of interest for the substorm on March 9, 1995 is 0400-0600 UT. Voronkov *et al.* [1999] studied this event in detail and estimated that growth phase commences between 0325-0335 UT. In Figure 4.7a the H_{β} (486.1 nm) emission data are shown for 0400-0600 UT. The data are in the form of emission intensity versus invariant latitude and time, and have a 1 minute temporal resolution. At 0400 UT preexisting proton aurora were moving slowly equatorward, and the equatorward motion increased rapidly after \sim 0430 UT. Figure 4.7b presents the simultaneous magnetometer data from the Churchill line of magnetometer stations. Only the geomagnetic north-south (X) component is shown. A positive perturbation of the magnetic X -component appeared after \sim 0400 UT, which indicates an enhancement in the eastward electrojet. The perturbation grew in magnitude until the expansive phase onset began at 0459 UT. Figure 4.7c shows the impulsive Pi2 pulsations obtained by filtering the raw data from

the Gillam station. These data also indicate that expansive phase onset takes place at 0459 UT. No Pi2 pulsations are present prior to expansive phase onset, indicating a "quiet" growth phase.

A time series of the poleward and equatorward border positions for the H_{β} luminosity is needed to fit the model data to the MSP emissions. These were obtained by fitting the emission borders to a Gaussian function. Where it was not possible to get a good fit using the Gaussian, a step-fit was adopted [Blanchard *et al.*, 1995]. Figure 4.8a shows the poleward and equatorward borders obtained in this way during the late growth phase and early expansive phase between 0430-0510 UT. Error bars are included, as well as the model best fit predictions which are shown as circles. The error bars are equal to the latitudinal resolution of the photometer observations. The least-squares best fit was obtained by varying the model current sheet thickness, and allowing three possible proton energies (*viz.* 10, 20, 30 keV). Using these time series, estimates are obtained for the model current sheet thickness during the late growth and early expansive phases (curve with circle markers in Figure 4.8b). The thickness quoted here is calculated at $X = -8 R_E$. Samson *et al.* [1992] found that the onset of the substorm intensification occurs in the region of proton precipitation which maps to the inner edge of the plasma sheet. This corresponds to the $\kappa = 3$ boundary, the $\kappa = 1$ boundary occurring further downtail. The solid line in Figure 4.8b (right-hand ordinate) indicates the location of the model plasma sheet inner edge. According to the model calculations, the plasma sheet inner edge moved towards the earth, and by substorm intensification it was inside $6 R_E$.

At the start of the modelling interval the current sheet was almost $2 R_E$ thick. It rapidly decreased and within 20 minutes was $0.2 R_E$ thick. This is consistent with satellite measurements [Fairfield, 1984; Mitchell *et al.*, 1990; Sergeev *et al.*, 1993]. Next the current sheet thickness was calculated as a function of time. A least squares

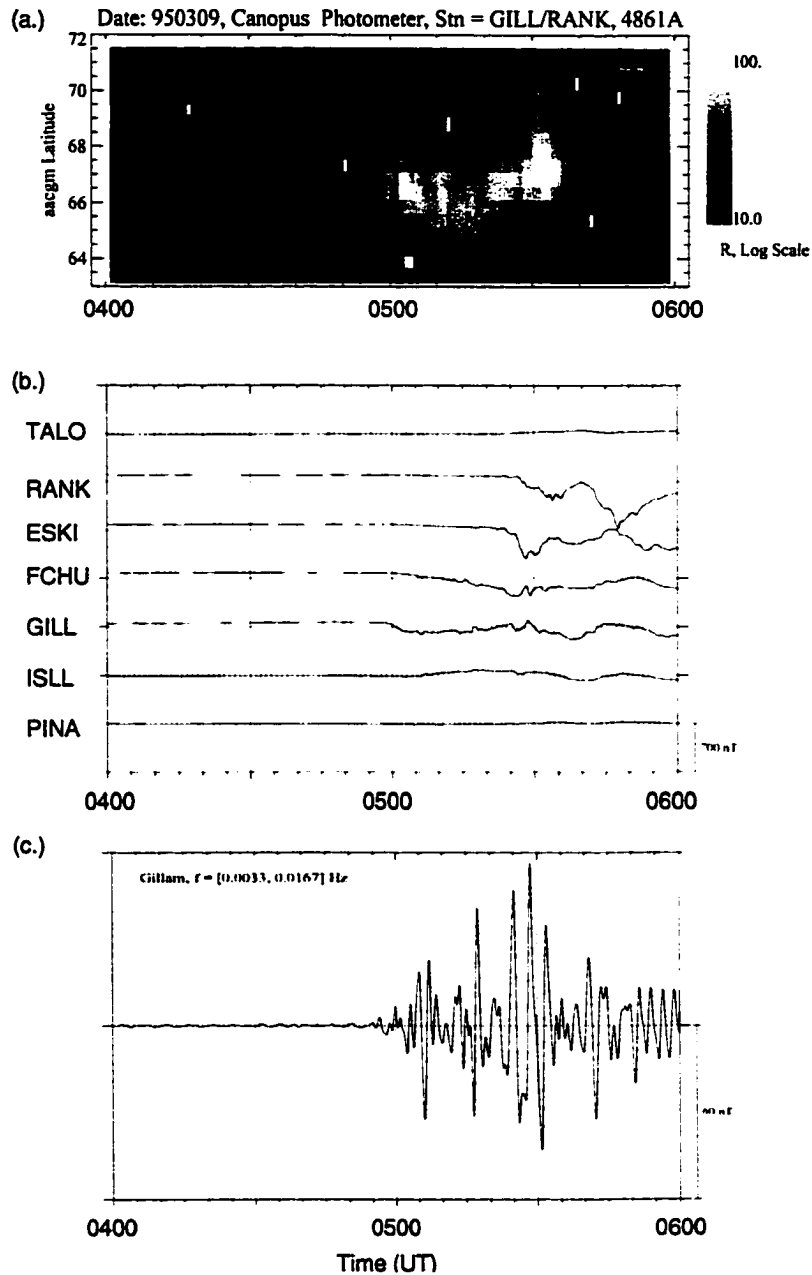


Figure 4.7: (a.) Meridian scanning photometer data (486.1 nm) from RANK and GILL in the CANOPUS array showing the growth phase and intensification of a substorm event on March 9, 1995. AACGM coordinates are explained by *Baker and Wing* [1989]. (b.) Magnetic X-component from the Churchill line of magnetometers, (c.) Magnetic X-component Pi2 pulsations at GILL. Local magnetic time is approximately UT minus 6 hours for the Churchill line.

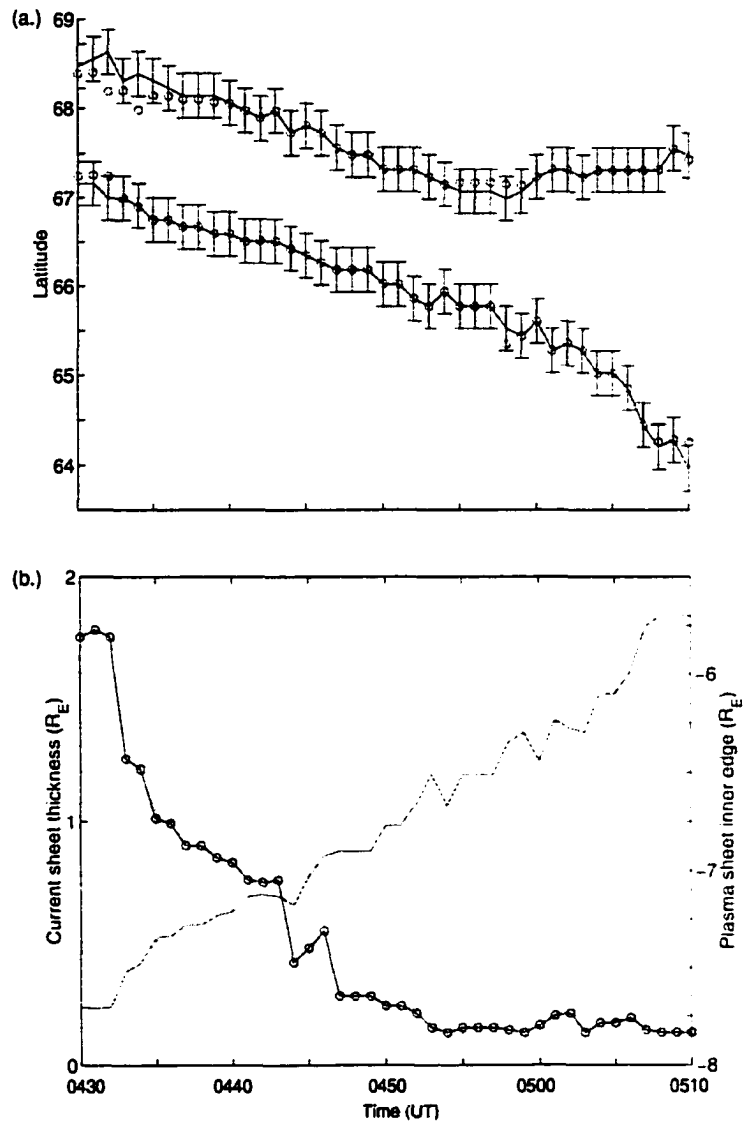


Figure 4.8: (a.) March 9, 1995 H_β emission boundaries are shown by the solid line, with error bars. The best fit values, calculated from the magnetic model predicted precipitation regions, are shown as circles. (b.) Model predictions for the current sheet thickness at $8 R_E$ (left ordinate), and plasma sheet inner edge position (right ordinate).

fitting for an exponential function was calculated between 0430-0510 UT. The best fit, expressed in terms of the current sheet half-thickness, L_z , is

$$L_z(t) = L_0 \exp(-t/\tau) \quad (4.4.3.15)$$

where the calculated values are $L_0 = 0.89 R_E$, and the timescale $\tau = 9.6$ minutes.

It is noteworthy that there is a high degree of correlation between the thinning of the current sheet, corresponding to magnetic field line stretching, and the equatorward motion of the proton aurora. In the framework of the model, this implies that the equatorward motion of auroral precipitation is directly related to the stretching of the magnetic field lines in the magnetotail.

February 9, 1995

This substorm has been extensively studied [Lui *et al.*, 1998]. Due to an unusually long interval of northward interplanetary magnetic field, the magnetosphere was as close to a low energy or "quiet" state as is likely possible before the advent of a substorm. Figure 4.9 shows the H_β emissions from 0330-0530 UT. The growth phase began at ~ 0335 UT, as seen in enhanced H_β emissions and the magnetometer data. From this time the H_β emissions continued moving equatorward until the expansive phase onset at 0437 UT, at which time the region of emissions rapidly expanded poleward. Figure 4.9b shows the ground magnetometer X -component at various locations in the Churchill line. Figure 4.9c shows the Pi2 pulsations obtained by filtering the raw data from the Back station.

The best least-squares fit of the model precipitation regions to the emission borders, calculated between 0400-0440 UT, is shown in Figure 4.10a. The best fit only

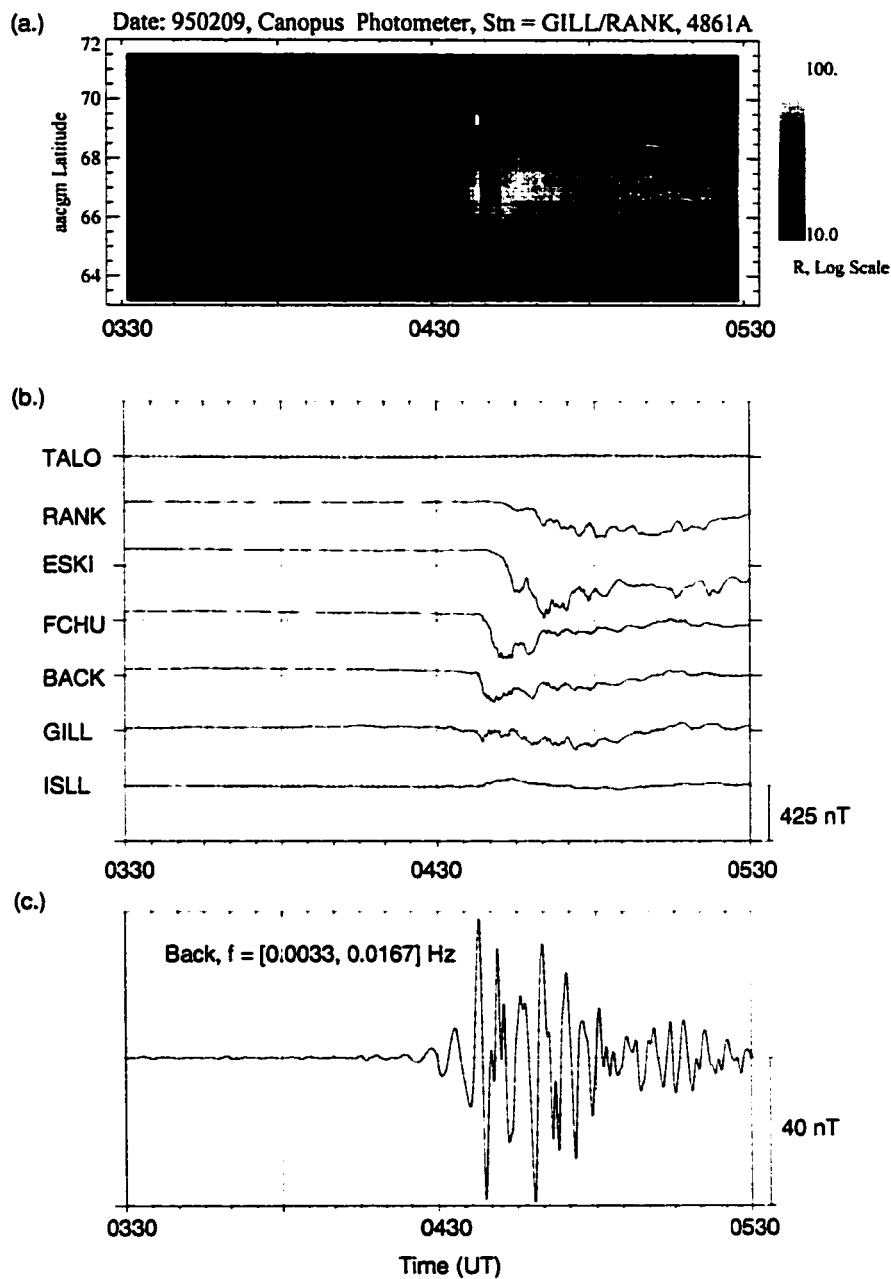


Figure 4.9: (a.) Meridian scanning photometer data (486.1 nm) from RANK and GILL in the CANOPUS array showing the growth phase and intensification of a substorm event on February 9, 1995. AACGM coordinates are explained by *Baker and Wing* [1989]. (b.) Magnetic X-component from the Churchill line of magnetometers, (c.) Magnetic X-component Pi2 pulsations at BACK. Local magnetic time is approximately UT minus 6 hours for the Churchill line.

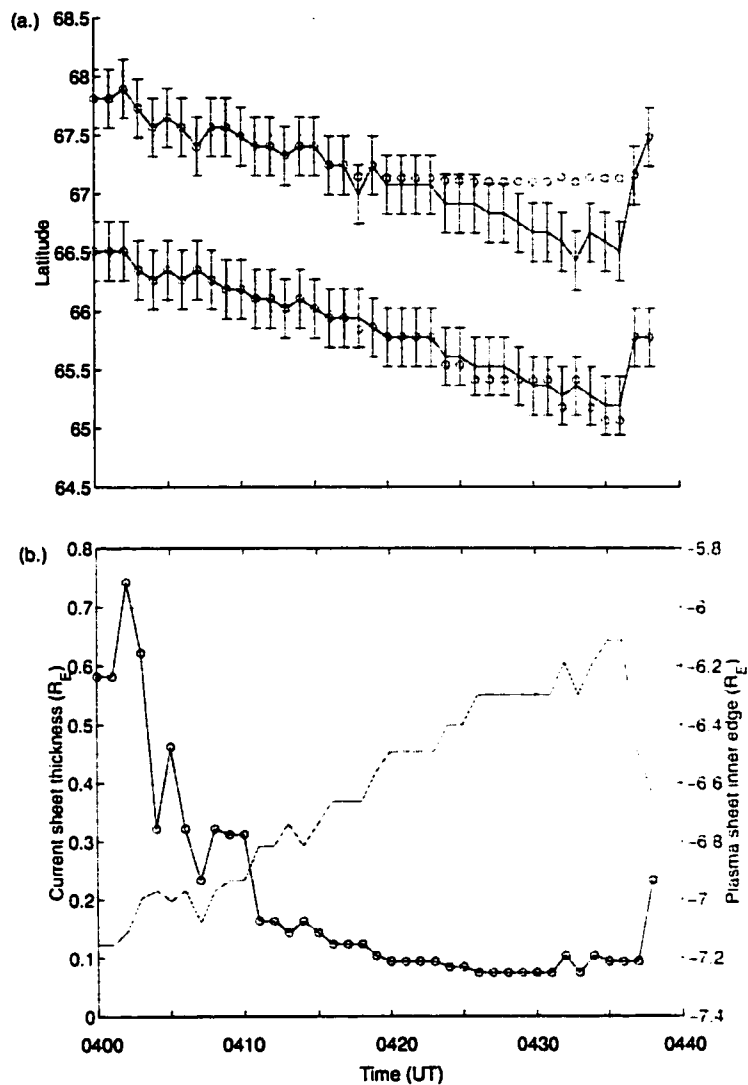


Figure 4.10: (a.) February 9, 1995 H_β emission boundaries are shown by the solid line, with error bars. The best fit values, calculated from the magnetic model predicted precipitation regions, are shown as circles. (b.) Model predictions for the current sheet thickness at $8 R_E$ (left ordinate), and plasma sheet inner edge position (right ordinate).

appears to be reasonable up to about 0428 UT; after this time the model is not a good fit to the high latitude precipitation border (Figure 4.10a). As with the previous example, the model plasma sheet inner edge moved towards the earth, and was little more than $6 R_E$ away at intensification. During the early stages of the modelling interval the predicted current sheet thickness is about $0.7 R_E$. By 0430 UT it is slightly less than $0.1 R_E$ thick. An interesting observation is that the current sheet remains extremely thin (close to $0.1 R_E$) for tens of minutes prior to the substorm intensification. This observation is helpful in theoretical modelling of growth phase, and gives a good estimate for the thin current sheet.

An exponential fit to the model crosstail current sheet half-thickness yielded $L_0 = 0.60 R_E$, and $\tau = 5.2$ minutes. The exponential fit was calculated between 0402-0428 UT. In this case, the timescale of growth phase thinning is smaller than that for the March 9, 1995 event. If one assumes that current sheet thickness corresponds to energy input into the magnetosphere, this implies that the rate of energy input was faster than for the March 9, 1995 case. Equatorward motion of the region of auroral luminosity acts as a proxy for the energy input into the auroral oval. If one assumes that current sheet thickness corresponds to energy input into the magnetosphere, this implies that the rate of energy input was faster than for the March 9, 1995 case.

For interest, also shown is the best fit at expansive phase onset (~ 0437 UT) and it is fascinating that the model predicts an impulsive thickening of the current sheet and tailward motion of the plasma sheet inner edge. However, not too much confidence should be placed in the model statistics at onset because the magnetotail geometry is changing so rapidly at this time. In each of the events studied the predicted locations of precipitating protons proceed equatorward at the same rate as the H_β auroral luminosity. Again, this provides evidence of the correlation between magnetic field line stretching and the equatorward motion of the proton aurora.

Summary of findings

Together with the MSP data and a simple magnetic field model the above analysis has shown that the crosstail current sheet does indeed thin during the course of a typical growth phase, and that this thinning corresponds to an equatorward motion of the region of proton auroral emissions. For these case studies it was found that the current sheet can thin dramatically during the growth phase, from $2 R_E$ to $0.1 R_E$. This is in accordance with the findings of previous studies, where very thin current sheets, as thin as $0.1 R_E$ have been inferred [Sergeev *et al.*, 1993; Sanny *et al.*, 1994; Kubyshkina *et al.*, 1999]. Furthermore, such extremely thin current sheets can remain stable for tens of minutes. Together with the fact that the H_β emissions mark the earthward edge of the plasma sheet, this analysis demonstrates quantitatively, and for the first time, that the model inner edge of the plasma sheet moves several R_E closer to the earth during the course of the substorm growth phase, sometimes to the region earthward of $6 R_E$ (as in the March 9, 1995 case). A current sheet half-thickness $L_z=0.05 R_E$ is thus selected for the model magnetic field.

4.3.3 Constraint from T96

The magnetospheric models of *Tsyganenko* [1987; 1989; 1996] depend on a relatively large number of parameters and are not appropriate (at present) for use in test particle simulations. Despite this fact, certain key features of the T96 model were relied upon to act as a proxy for the magnetotail while setting the parameters in the new model. In fact profiles of the T96 magnetic field were studied in order to find a simple functional representation for the model fields, and led to the present form of the WFR. The previous analysis demonstrates that using a current sheet thickness of $0.1 R_E$ (i.e. $L_z = 0.05 R_E$) is perfectly reasonable for the late stages of the growth

phase. Thus the model is complete, comprising the components of the dipole, tail, and WFR. The parameters for the model magnetic field are summarised in Table 1.

Field component	Parameter name	Value
Dipole	$M (nt/R_E^3)$	31100
Tail	$B_0(nT)$	50
Tail	$L_z(R_E)$	0.05
Tail	ν	1.25
Tail	ϵ	0.002
WFR	$B_p(nT)$	28.45
WFR	$B_n(nT)$	1
WFR	$L_y(R_E)$	$3^{1/2}$

Table 1: Final magnetic field model parameters.

Figures 4.11 and 4.12 show comparisons of the T96 field with the complete model magnetic field (dipole+tail+WFR). T96 input parameters that are feasible for growth phase conditions were selected; $B_Y^{MF} = 0$ was used so that there would be no skewing of the magnetic field. For substorms, *Turner et al.* [2000] found that DST can be as large as -80 nT, and that the tail current typically contributes about 25% to DST . A $DST=-40$ nT value was chosen and considered not unreasonable for late growth phase. The new magnetic field model tends to have larger field values than T96, especially around the NS region. It is not particularly worrying that the model fields are larger since T96 is a statistical average model encompassing maximum and minimum values. What is more important, from the modelling aspect, is that the shapes of the magnetic field profiles are essentially the same. The clearest difference in the models comes from the thin current sheet. Whereas the B_x component of T96 is slowly varying about the neutral sheet, B_x for the new model varies relatively strongly, due to the thin current sheet. Figure 4.13 shows a comparison of the new magnetic field model field lines to the empirical T96 model field lines. In the region

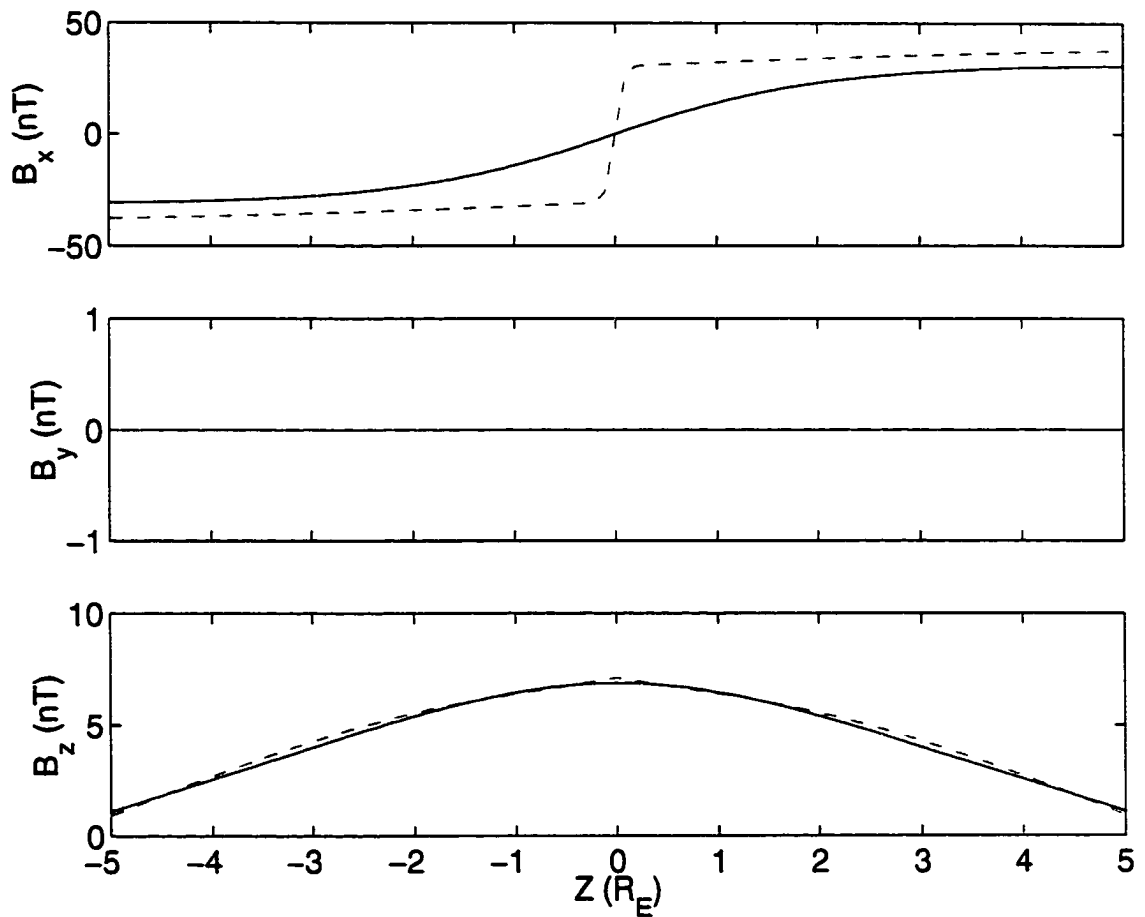


Figure 4.11: Components of the magnetic field plotted as a function of distance from the neutral sheet Z , calculated at $X=-15 R_E$ and $Y=0$. The new model is the dashed and T96 is the solid curve. Parameters for T96 are $P_{DYN}=1$ nPa, $DST=-40$, $B_Y^{IMF}=0$, $B_Z^{IMF}=-1$, $TILT=0^\circ$.

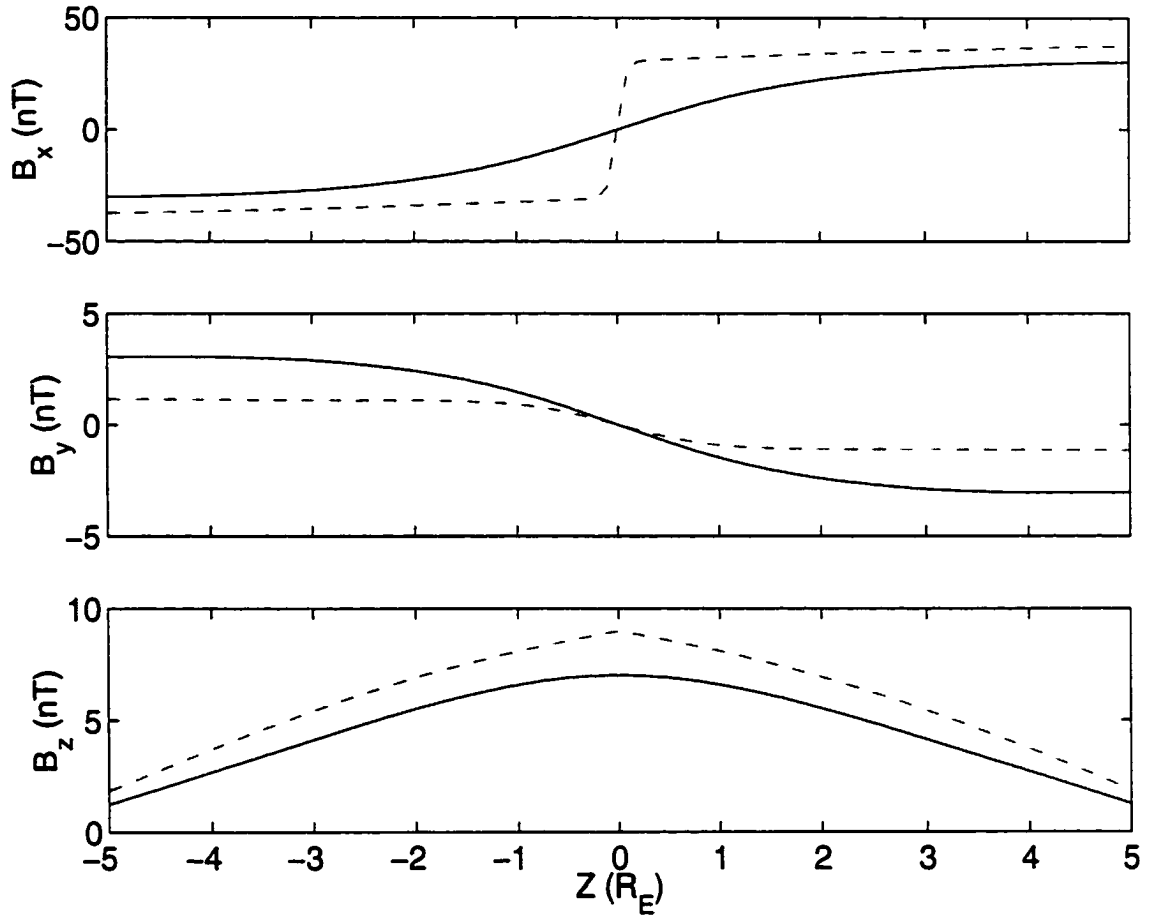


Figure 4.12: Components of the magnetic field plotted as a function of distance from the neutral sheet Z , calculated at $X=-15 R_E$ and $Y=2$. The new model is the dashed and T96 is the solid curve. Parameters for T96 are $P_{DYN}=1$ nPa, $DST=-40$, $B_Y^{IMF}=0$, $B_Z^{IMF}=-1$, $TILT=0^\circ$.

of the current sheet the T96 model is very different. This is to be expected, since the new model introduced here assumes an extremely thin current sheet that would occur near the end of a growth phase. Since T96 is a statistical fit over all phases of geomagnetic activity, one cannot expect it to represent the late growth phase current sheet region with reasonable accuracy. Any empirical model tends to have a thicker current sheet than is present in the actual magnetotail on many occasions. This is because the actual magnetotail flaps up and down in the Z -direction. Such tail flapping increases the apparent observed thickness obtained by averaging or binning the satellite data. It is clear that T96 is more flared downtail, and that the new model is more stretched, particularly in the near-earth region, where clear negative curvature occurs. Further comparisons of the B_x , B_z , and J_y components are shown in Figures 4.14 and 4.15.

4.3.4 Constraint from the lobe magnetic field

Slavin et al. [1985] used the ISEE 3 satellite to calculate the radial falloff of the tail lobe magnetic field from 20 to 130 R_E downtail. A more recent study by *Nakai et al.* [1991] uses the ISEE I satellite to investigate the lobe magnetic field in the region from 10 to 22.6 R_E downtail. A comparison of these empirical results with the new model lobe field, calculated at $Z = 10 R_E$, is shown in Figure 4.16.

4.4 Model electric field

Instead of modelling the electric field as a constant it is allowed it to vary with position, and is directed primarily in the Y -direction. Previous studies of test particle motion have tended to use a model featuring constant electric field, directed in the

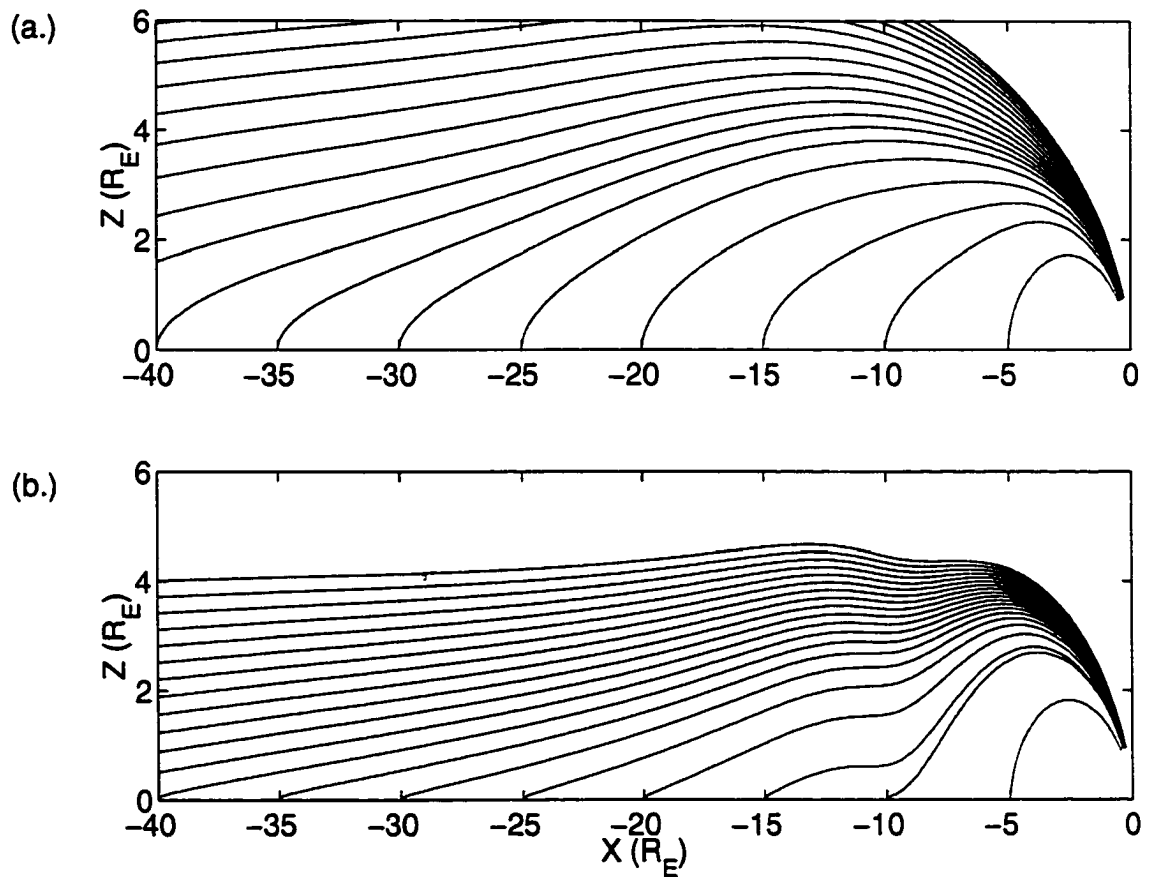


Figure 4.13: Comparison of the model magnetic streamlines to the empirical T96 model. (a.) T96 model with $P_{DYN}=1$ nPa, $DST=-40$, $B_Y^{IMF}=0$, $B_Z^{IMF}=-1$, $TILT=0^\circ$ and (b.) the new model.

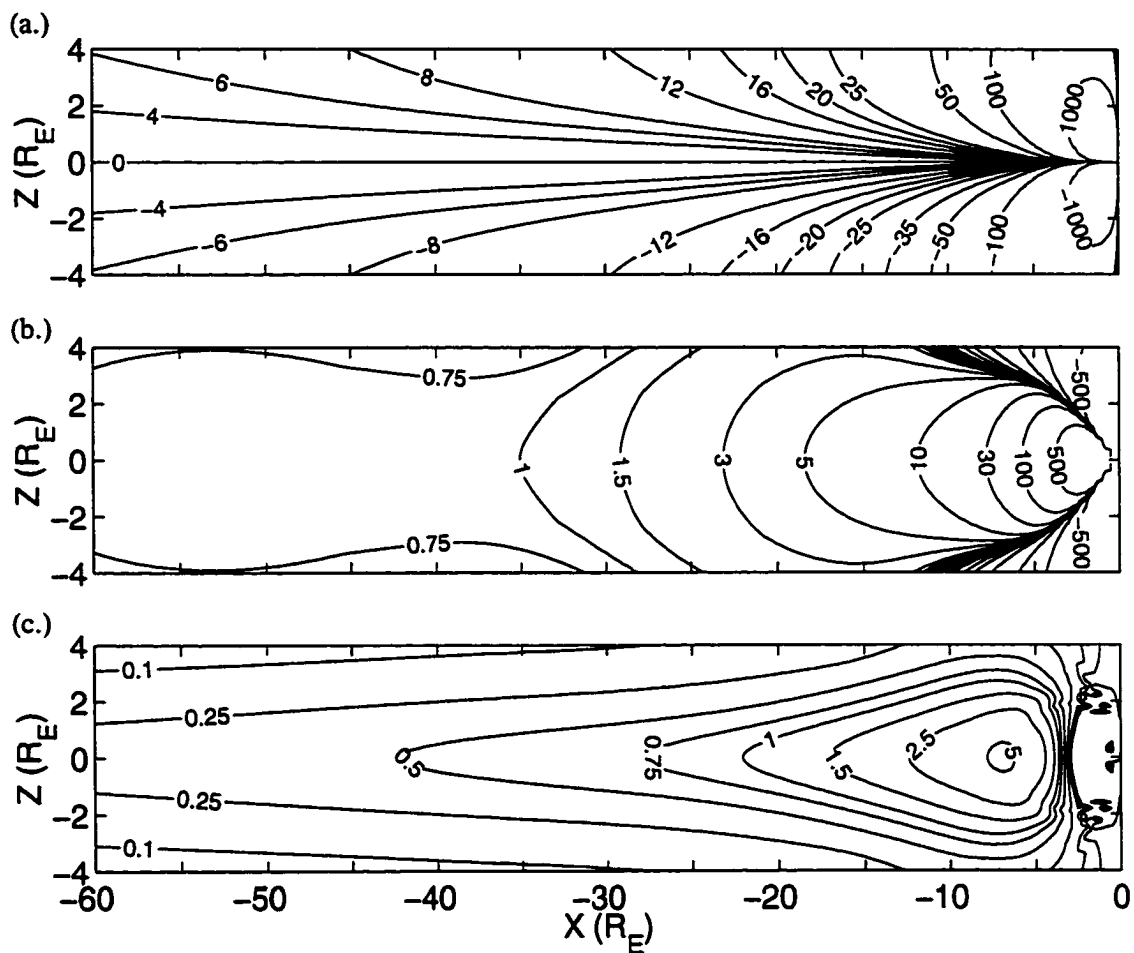


Figure 4.14: T96 model with $P_{DYN}=1$ nPa, $DST=-40$, $B_V^{IMF}=0$, $B_Z^{IMF}=-1$, $TILT=0^\circ$. Contours of constant (a.) B_x (nT), (b.) B_z (nT), (c.) J_y (nA/m^2) in the noon-midnight meridian.

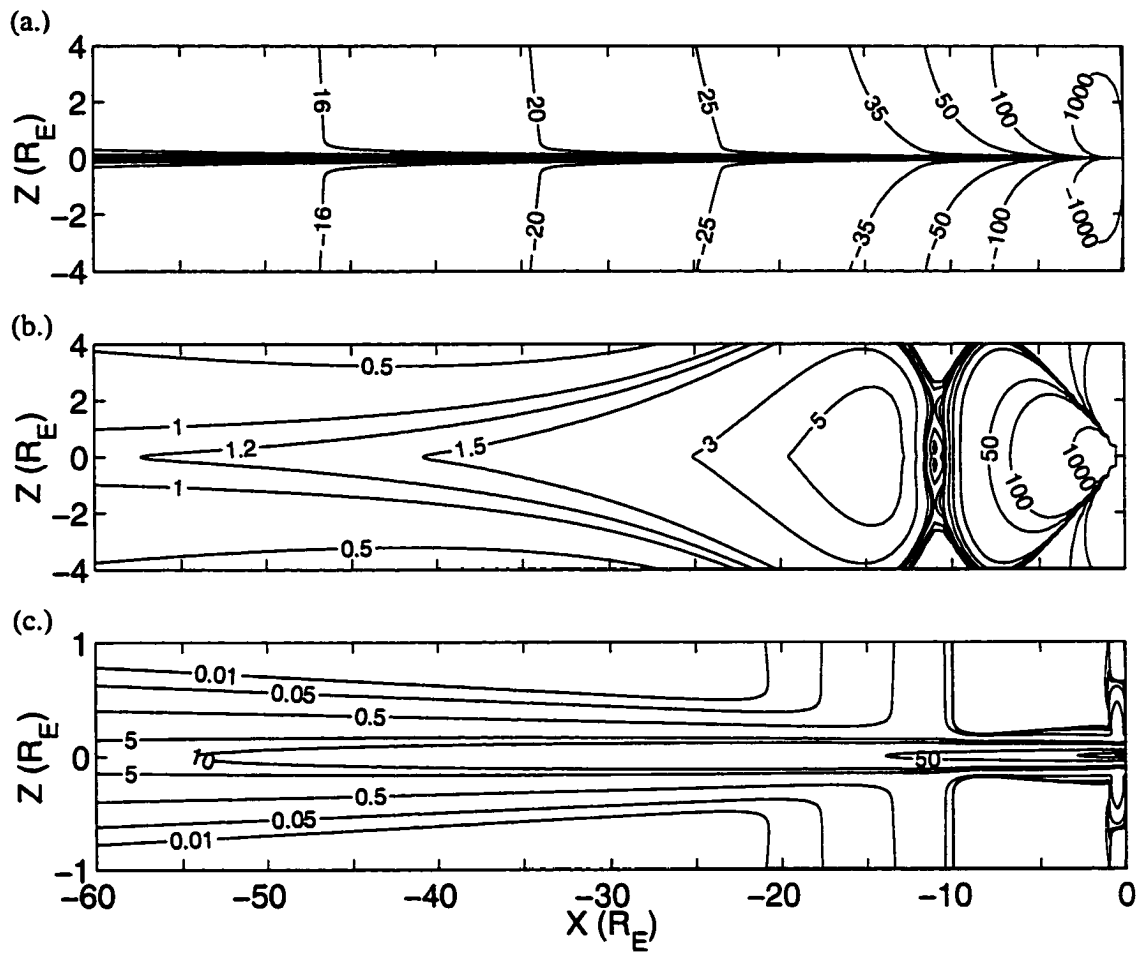


Figure 4.15: Contours of constant (a.) B_x (nT), (b.) B_z (nT), (c.) J_y (nA/m²) for the new magnetic field model, plotted in the noon-midnight meridian.

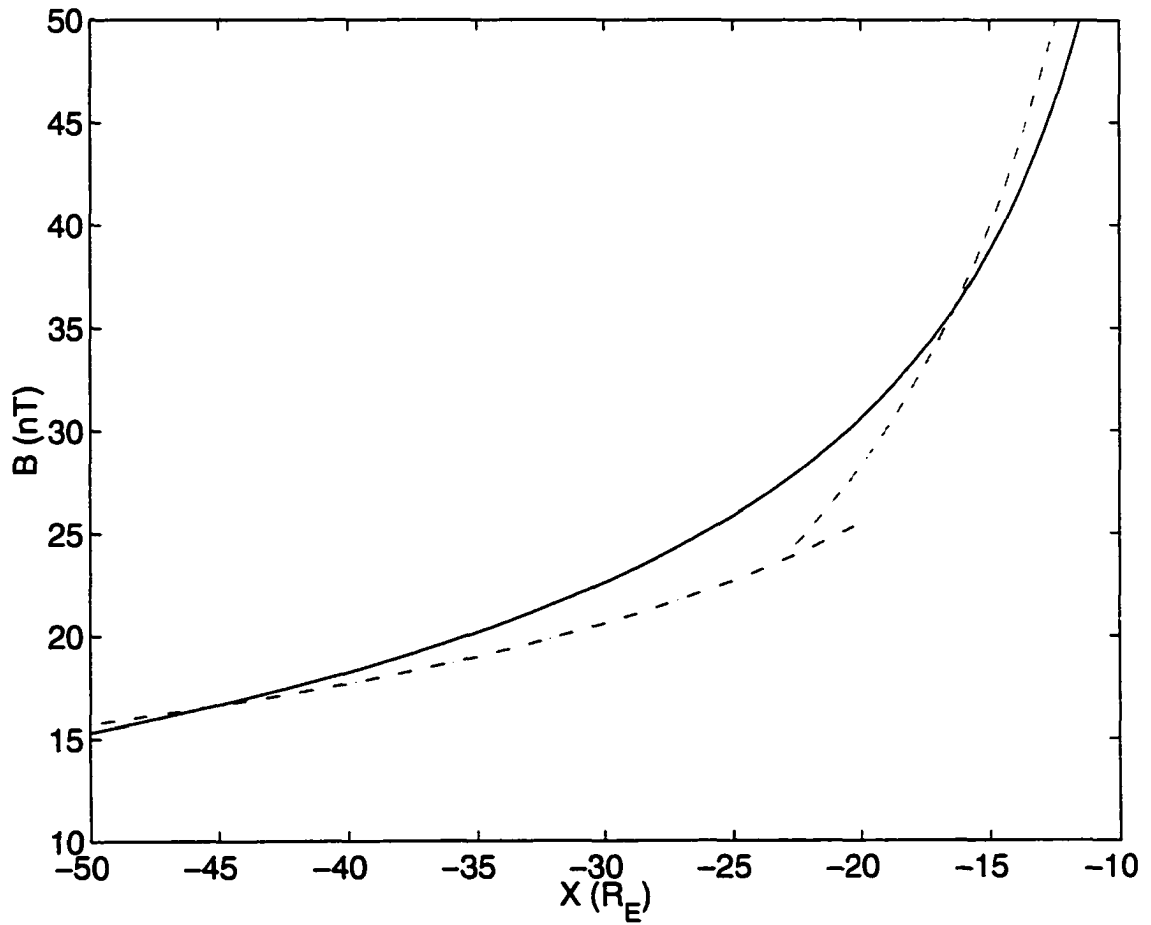


Figure 4.16: Lobe field strength for the new model (solid curve), calculated at $(Y, Z) = (0, 10) R_E$, is compared with the empirical functions of *Slavin et al.* [1985] (dot-dash curve) and *Nakai et al.* [1991] (dashed curve).

Y-direction (e.g. *Onsager et al.*, 1991; *Ashour-Abdalla et al.*, 1991a, 1991b, 1996; *Larson and Kaufmann*, 1996), although there are some models that have used non-constant electric fields [*Cladis*, 1986; *Sauvaud and Delcourt*, 1987; *Joyce et al.*, 1995]. The problem with a constant electric field model lies in the fact that the magnetotail electric field is usually largest at high latitudes, and typically smallest near the NS. Test particle simulations were performed with a constant electric field model ($E_y = 2mV/m$), and it was possible to arrive at similar results to those that will be discussed in Chapter 5. However, this field amplitude is unreasonable near the NS region, and it was decided to use a model that is more realistic. Furthermore, since the model WFR produces very small equatorial B_z in the near-earth region, a constant electric field model results in unrealistic convection velocities in the neutral sheet around the WFR. To attempt to solve this problem of what constitutes a more realistic electric field model, one needs to consider a magnetic flux tube that extends from the ionosphere to the neutral sheet. Next one assumes that magnetic field lines in the flux tube are electric equipotentials; i.e.

$$V = \oint \vec{E} \cdot d\vec{r} = constant \quad (4.4.4.16)$$

Since the integral

$$\oint \vec{B} \cdot d\vec{A} = constant \quad (4.4.4.17)$$

is the same for any closed surface that cuts through the flux tube then the electric field at \vec{r} is given by

$$\vec{E}_y(\vec{r}) = \vec{E}_{eq} \left(\frac{B}{B_{eq}} \right)^{1/2} \quad (4.4.4.18)$$

where \vec{E}_{eq} and B_{eq} are, respectively, the electric field vector and total magnetic field at the footpoint in the neutral sheet for the magnetic field line that passes through \vec{r} .

This model forms the basis for a computationally more efficient electric field model, given by

$$E_y(\vec{r}) = \alpha B^{1/2} \quad (4.4.4.19)$$

where α is a constant, related to the polar cap potential, and the electric field is directed in the Y -direction. After some dimensional analysis, the units for α are found to be $(V/s)^{1/2}$.

4.4.1 Cross polar cap potential

To select a reasonable value for α requires knowledge of the cross polar cap potential difference. This potential can be mapped along open field lines, and assuming a crosstail magnetosphere width of $40 R_E$, the appropriate large scale crosstail electric field can be calculated by

$$E_y = \Delta\phi/40R_E. \quad (4.4.4.20)$$

Kan et al. [1988] demonstrated that the polar cap potential drop needed to exceed a minimum level, 70 kV in their model, prior to substorm expansive phase. This is thus the minimum allowable potential drop in the new model, and corresponds to $E_y \sim 0.3$ mV/m in the distant tail where $B_z \sim 1$ nT. This, in turn, corresponds to $\alpha = 9$ $(V/s)^{1/2}$. *Alexeev et al.* [1993] used theoretical considerations to show that the potential drop was large for southward IMF, and for $B_z^{IMF} < -5$ nT was

$$\Delta\phi(kV) \sim 70 - 7.3B_z^{IMF}(nT) \quad (4.4.4.21)$$

Since most substorm growth phases feature times of negative B_z^{IMF} , this equation can be used to show that growth phases with a reasonable $B_z^{IMF} \sim -3$ nT produce $\Delta\phi \sim 90$ kV. This corresponds to $\alpha \sim 11.4$ (V/s)^{1/2}.

The observational study of *Weimer et al.* [1992] is of special interest, since they studied variations of polar cap potential, measured during different stages of 64 isolated substorms. Their Figures 3 and 7 are reproduced here in Figure 4.17. The left hand side of Figure 4.17 shows the polar cap potential measured as a function of time relative to the time from substorm expansive phase onset. They have been grouped according to the peak magnitude of the AE index during the associated substorm. The right hand column in Figure 4.17 shows IMF B_z , in GSM coordinates, plotted against time relative to expansive phase onset, and grouped as before. It is clear that IMF B_z becomes negative prior to onset, and can remain negative for over an hour. For moderate ($600 < \text{peak AE} < 1000$ nT) and large ($\text{peak AE} > 1000$ nT) substorms, B_z prior to expansive phase onset can be large and negative, often exceeding -5 nT for over an hour. A general trend in the left column of Figure 4.17a,b, and c is that cross polar cap potential increases during the time preceeding expansive phase onset. For the small substorms ($\text{peak AE} < 600$ nT; Figure 4.17a) the polar cap potential is in the range 40 to 80 kV during the late growth phase, shortly before expansive phase onset. Intermediate substorms ($600 \text{ nT} < \text{peak AE} < 1000$ nT) showed that in some cases potentials over 70 kV were measured more than 2 hours before onset, and potentials over 110 kV were measured at 1 hour before onset. The large substorms ($\text{peak AE} > 1000$ nT) have cross polar cap potentials from 90 kV to over 150 kV during the growth phase (i.e. $\alpha=11.4$ to >18.6 (V/s)^{1/2}). These data indicate that a cross polar potential drop of 60-120 kV ($\alpha=8-16$ (V/s)^{1/2}) is not unreasonable during

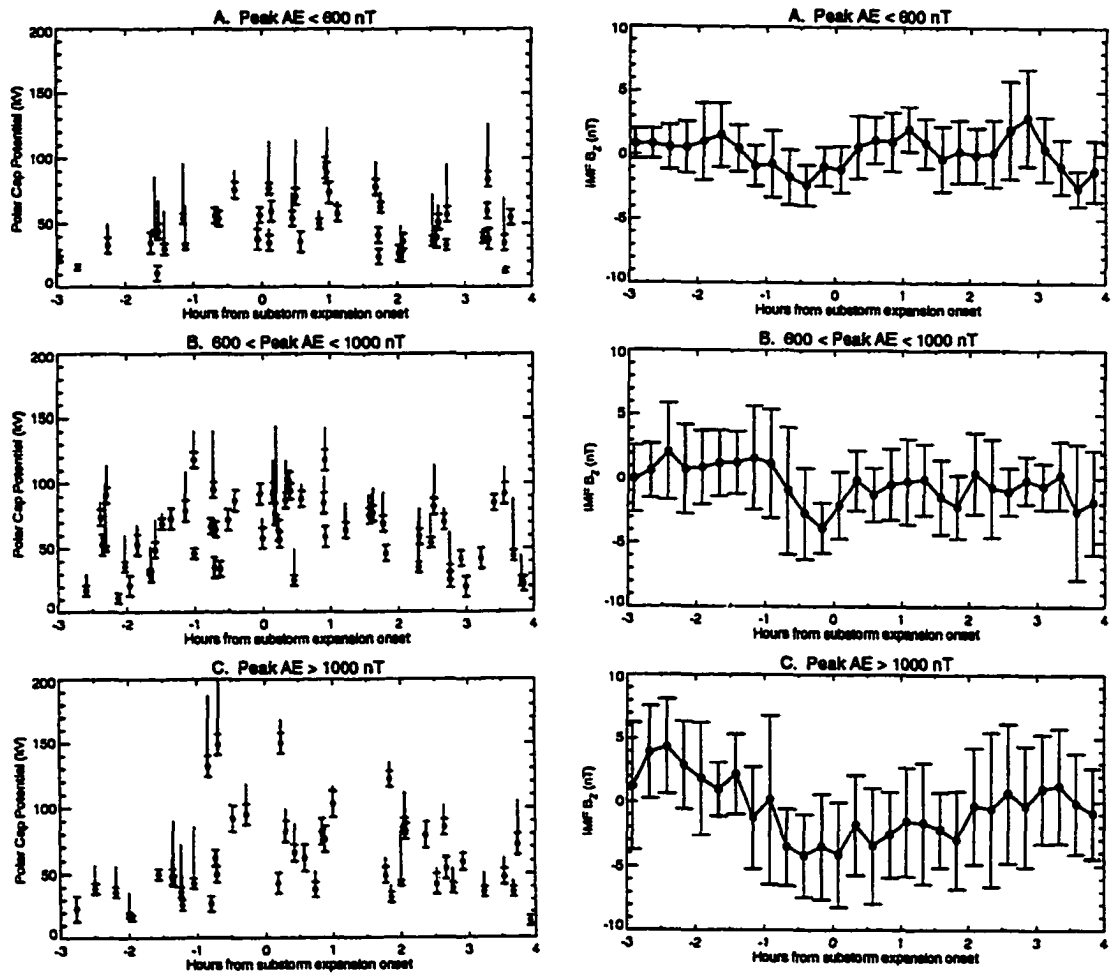


Figure 4.17: Superposed epoch analysis of polar cap potential drop and IMF B_z for various activity levels as quantified by the AE index (after *Weimer et al.* [1992]). The onset of substorm expansive phase is identified as $t = 0$. The solid circles show measured potential differences, obtained from an integration of the electric field. The error bars show the integration errors associated with the electric field uncertainty of 2 mV/m. The lines extending upward from the circles end at the "corrected potential", which is an estimate of what the true potential drop may have been, based on the magnetic local times at the reversals, as discussed in *Weimer et al.* [1992].

the latter stages of a substorm growth phase, and would correspond to potentials observed during intermediate and large scale substorms. This would result in electric fields of 0.25-0.5 mV/m in the distant tail neutral sheet.

The recent study of *Miyashita et al.* [1999] serves to further confirm that a value $\alpha=16 (V/s)^{1/2}$ is reasonable for the late substorm growth phase. *Miyashita et al.* [1999] selected 263 substorm events and statistically investigated, amongst other parameters, the time variations of the electric field in the region $-7.5 \geq X \geq -52.5R_E$ and $-15 \leq Y \leq 15R_E$ in GSM coordinates. The electric field was calculated using the frozen in relation, $\vec{E} = -\vec{V} \times \vec{B}$. They found that, at 10 minutes before substorm expansive phase onset, and for $X \approx -10R_E$ and $X \approx -28R_E$, the electric field E_y values are large, with an average about 0.7 mV/m. In the intermediate region around $X \approx -18 R_E$ the electric field E_y is about 0.4 mV/m. Accordingly, $\alpha=16 (V/s)^{1/2}$ is used for the simulations in the next chapter.

4.4.2 E_x and E_z components

The main concern with the electric field (Equation 4.4.4.19) is that at certain locations, notably in the neutral sheet region, it is possible to have $\nabla \times \vec{E} \neq 0$. Although this form of the electric field does not satisfy $\nabla \times \vec{E} = 0$ everywhere, if it is sufficiently small on the relevant scales it will be unimportant. Qualitatively, it would be expected that since the magnetic field changes slowly on the relevant length scales in the distant magnetotail $\nabla \times \vec{E}$ would be relatively small and no problems will arise. This is also true closer to the earth. However, in the region of the NS and near the WFR $\nabla \times \vec{E}$ could become large and thus affect particle motion. To ameliorate the effects of nonzero $\nabla \times \vec{E}$, other components of the electric field are included, i.e. E_x, E_z .

From Maxwell's equations

$$\nabla \times \vec{E} = -\partial_t \vec{B}. \quad (4.4.4.22)$$

For this situation, where the magnetic fields are time independent, the right hand side of Equation 4.4.4.22 is zero. Breaking this equation into components, one arrives at the following expressions for E_x and E_z .

$$\begin{aligned} E_x &= \int dy \partial_x E_y \\ E_z &= \int dy \partial_z E_y. \end{aligned} \quad (4.4.4.23)$$

If it is assumed that E_y is slowly varying in the Y -direction then further simplifications may be used. To approach this problem quantitatively a gradient scale length is defined as

$$L_g = \left| \frac{\partial_y E_y(\vec{r})}{E_y} \right|^{-1} \quad (4.4.4.24)$$

If L_g is large compared to the magnetotail scale lengths in the Y -direction, then E_y is indeed slowly varying in Y . The quantity L_g is plotted in the $X - Y$ plane in Figure 4.18. The upper figure shows contours of constant $L_g(R_E)$ in \log_{10} units plotted in the $Z=0$ plane. As can be seen from this figure, the gradient scale length is smallest exactly at the equatorial plane at $Z=0 R_E$ around $X=-11 R_E$. It's smallest value is $L_g \sim 0.2 R_E$, implying that, in this narrow region (in X) slightly beyond $Y=0.2 R_E$ the approximation is not valid. The lower figure, calculated at $Z=0.1 R_E$, shows that further from the NS the assumption is easily satisfied.

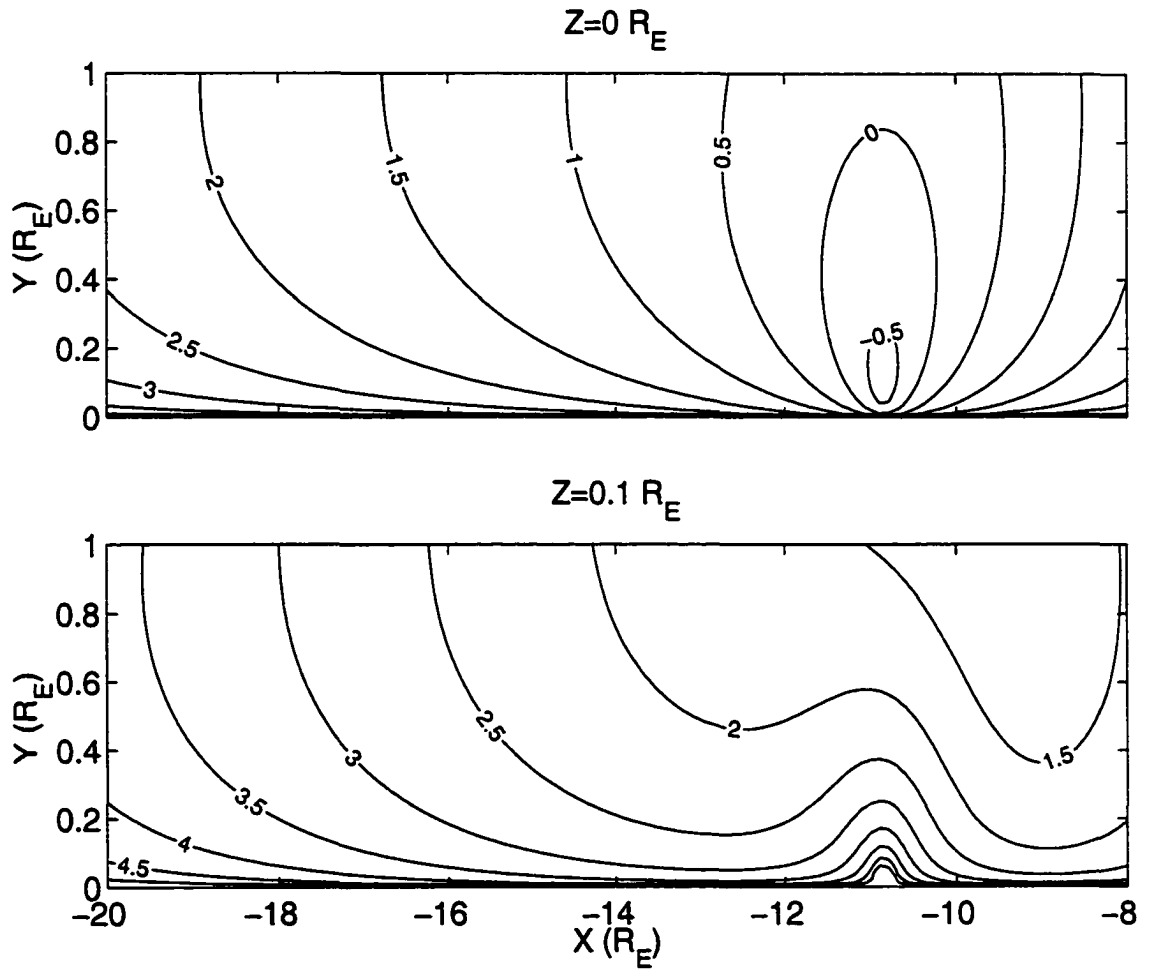


Figure 4.18: Contour plots of $\log_{10}(L_g)$ where L_g (in R_E) is the gradient scale length defined in Equation 4.4.4.24. The contours are in the $X - Y$ plane at $Z=0 R_E$ (top) and $Z=0.1 R_E$ (bottom).

Now that the variation of E_y is established to be slowly varying in Y , a reasonable approximation for the model E_x and E_y is

$$\begin{aligned} E_x &= y\partial_x E_y \\ E_z &= y\partial_z E_y. \end{aligned} \tag{4.4.4.25}$$

With the full electric field expressed by the terms thus described, one finds that in general $E_x, E_z \ll E_y$. However in the narrow region at $X \sim -11 R_E$, for $|Y| > 0.5 R_E$, it is possible to have $E_z > E_y$. This is to be expected since this is where L_g becomes quite small because E_y is not slowly varying here. In the test particle simulations, one might be tempted to avoid possible complications by excluding any particles from this region. However, it turns out that whether they are excluded or not makes no noticeable difference to the model distribution functions.

4.4.3 Curl time scale

It is necessary to consider the effect of $\nabla \times \vec{E} \neq 0$. Because E_y varies so sharply about the NS, this is a region where problems may arise. Equation 4.4.4.22 is ideally equal to zero. The electric field can be used provided $\nabla \times \vec{E} \ll 1$. To examine this quantitatively it is necessary to calculate a curl scale time, which is defined as

$$t_{curl} = \left| \frac{\nabla \times \vec{E}}{\vec{B}} \right|^{-1} \tag{4.4.4.26}$$

If this timescale is much greater than the simulation timescale (t_{sim}), and the Alfvénic transit time (t_A), then unrealistic effects caused by a curl in the electric field will be minimal over the particle trajectory. Thus the inequality that must be satisfied is

$$\frac{T}{t_{curl}} \ll 1; T = \sup\{t_{sim}, t_A\} \quad (4.4.4.27)$$

The model simulations are stopped by $t_{sim}=30$ minutes, which is almost always larger than the Alfvén transit time, given by

$$t_A = L/V_A \quad (4.4.4.28)$$

where L is the scale size of the system ($\sim 200 R_E$), and V_A is the Alfvén speed

$$V_A = \frac{B}{(\mu_0 \rho_m)^{1/2}} \quad (4.4.4.29)$$

where ρ_m is the mass density. The only place where \vec{E} changes rapidly is near the WFR and near the NS. If a number density is known then one may test to see where equation 4.4.4.27 is valid. A density of 0.2 cm^{-3} is assumed in the NS at $X=-10 R_E$, decreasing linearly to 0.08 cm^{-3} at $-100 R_E$. Figure 4.19 shows the variation of t_A/T at $Z = 0 R_E$ (top) and $Z = 0.1 R_E$ (bottom). The ratio is largest in the NS and around the WFR (top figure). However, the inequality of Equation 4.4.4.27 is satisfied everywhere. This means that the electric field is suitable for use in test particle tracing.

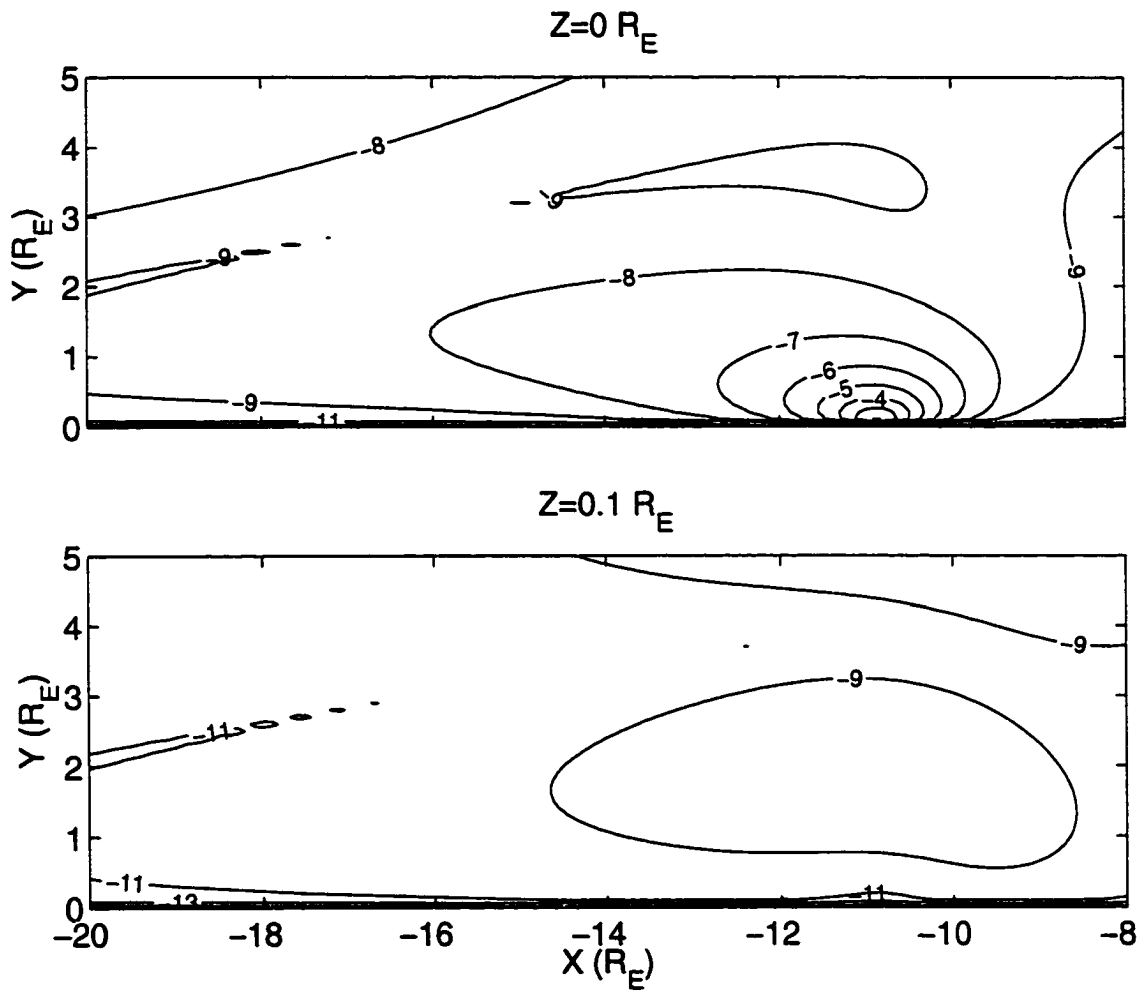


Figure 4.19: Contour plot of $\log_{10}(T/t_{curl})$ defined in Equation 4.4.4.27. The top figure shows contours in the $X - Y$ plane at $Z=0 R_E$. The bottom figure is for data computed in the $X - Y$ plane at $Z=0.1 R_E$.

CHAPTER 5

Simulation of magnetotail ion distribution functions

In this chapter the mapping technique of Chapter 3 will be applied using the new magnetic field model. Ion distribution functions are calculated in the model magnetotail, to determine whether fast flows can develop in the stretched magnetic field geometry, especially in the current sheet region. The existence of fast ion flows in the magnetotail is well known; the source of these flows is not. Fast earthward flows in the PSBL are typically identified as ion beams. These beams are considered to be formed in two possible ways, viz. 1.) when ions are ejected from a neutral line to form beams at the edge of the PS (e.g. *Onsager et al.* [1991]) or 2.) when ions have undergone Speiser motion in the current sheet region, and are subsequently ejected out of the current sheet (e.g. *Lyons and Speiser* [1982]). In this chapter the source of these beams will not be considered. Instead, the *consequences* of their existence will be considered in terms of flows at lower latitudes.

Tailward beams develop deeper in the PSBL. They are considered to be the mirrored counterparts of the earthward beams. Accordingly, nearer the current sheet region (CS), the bulk velocities, calculated from distribution functions, normally tend to decrease. However, during magnetospheric substorms, fast earthward or tailward flows can develop in the CS, and are usually interpreted in terms of a NENL [*Angelopoulos et al.*, 1992, 1994; *Kettmann et al.*, 1993; *Machida et al.*, 1994; *Nagai et*

al., 1998; *Baker et al.*, 1999]. *Eastman et al.* [1984] identified fast PSBL-like flows close to the neutral sheet during times when the current sheet was thin, and it is interesting to consider whether such flows might sometimes be interpreted incorrectly in terms of a NENL. In this chapter, the new magnetic field model is used primarily to test the hypothesis that it is possible to have anisotropic anti-sunward flows in the CS through simple magnetotail dynamics, without appealing to a NENL. This is not to discount the possibility that some fast flows are the result of a NENL. Indeed, the technique of distribution function modelling using noninteracting particles has a fundamental nonuniqueness problem: showing a mechanism that can model fast tailward flows, for example, does not prove it is the correct mechanism, or the only one. But such a result poses the suggestive question: could it be that at least some tailward flows are a consequence of PSBL dynamics, independent of any explanation related to neutral lines? The results presented in this chapter are an attempt to answer this question.

First, the new model will be compared with results from a previously published model. Next a novel boundary condition is introduced, which simulates the PSBL-lobe interface. Then this new model is used to describe model ion distributions, particularly near the CS region. Stability of the model distributions is considered through the addition of electrostatic noise at the model boundary.

5.1 Comparison with previous model results

The work of *Onsager et al.* [1991] provides a useful basis for comparison with the present model. They demonstrated that a two-dimensional model, based on quasi-steady reconnection in the distant magnetotail, is able to reproduce all the observed features in the observed electron and ion distribution functions in the PSBL. Their

technique of mapping distribution functions is the same as is used in this work, although the magnetic field and electric field models are different. They used a plasma sheet as well as a lobe source boundary condition to calculate model distribution functions in the PSBL. The source distributions were assumed to be Maxwellian. For the CPS condition, the boundary is located at $Z=0$, in the neutral sheet (NS). The lobe boundary is defined as the high-latitude separatrix, the surface separating the open and closed magnetic field lines in their model. Values of density and temperature they used to specify the CPS boundary condition were, for the ions, $n=0.15 \text{ cm}^{-3}$, $T_i=5 \text{ keV}$ at $15 R_E$ downtail from the earth, and $n=0.002 \text{ cm}^{-3}$, $T_i=4 \text{ keV}$ at $100 R_E$ behind the earth. The parameters varied linearly along the tail. The lobe source was assumed to be constant along the model boundary and featured $n=0.02 \text{ cm}^{-3}$ and $T_i=40 \text{ eV}$. In their work *Onsager et al.* [1991] also studied electron distributions, but here only ions will be considered.

The magnetic field model introduced in Chapter 4 was used to perform comparable simulations using the same boundary conditions as *Onsager et al.* [1991]. Although these two magnetic field models are quite different, the results are essentially the same. Model ion distributions from the new model are shown in Figure 5.1, and are similar to *Onsager et al.* [1991]. The distribution functions are shown in the $V_x - V_y$ plane (V_x is positive towards the earth). The Z -position (distance from the neutral sheet) are shown above each figure. At these Z -values above the neutral sheet the model magnetic field is mainly in the X -direction. Thus V_x corresponds to velocities parallel to the magnetic field. Observations indicate that the nature of the PSBL distribution functions often change in a continuous way [*Forbes et al.*, 1981; *Angelopoulos et al.*, 1989]. The outermost edge of the PSBL is signalled by the presence of only the cold lobe ions (Figure 5.1a). Deeper into the boundary layer only earthward streaming is observed. This is followed by a "kidney bean" shaped set of

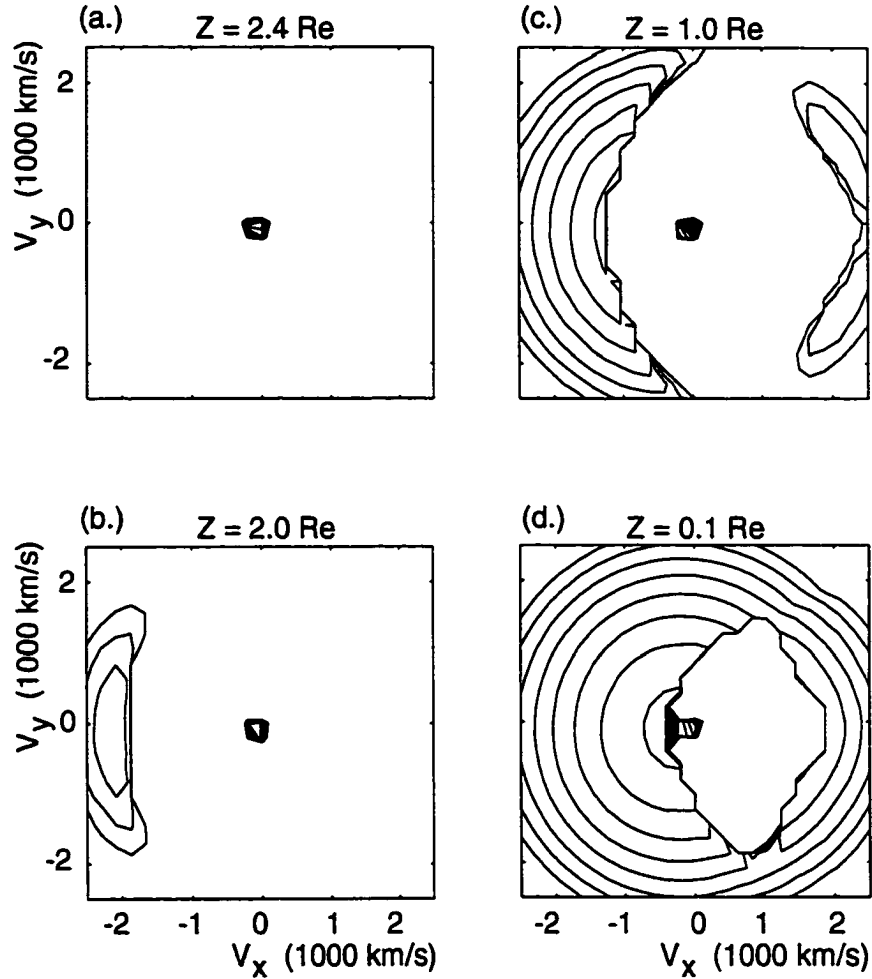


Figure 5.1: Model ion two-dimensional velocity space distributions at four locations in the PSBL, $Z=2.4$, 2.0 , 1.0 , and $0.1 R_E$, all at $X=-15 R_E$. The parallel velocity is in the earthward direction. The closely spaced contours centred at zero speed correspond to the cool lobe plasma. The higher speed particles correspond to the hot central plasma sheet particles which have entered the boundary layer with initially most of their energy in parallel motion. Two contours per decade are shown, with the lowest value being at $-17.5 s^3/m^6$.

contours in the distribution function slightly closer to the equatorial plane (Figure 5.1b), and then counterstreaming beams still deeper in the PSBL (Figure 5.1c). The distribution function at $Z=0.1 R_E$ is quasi-isotropic, or shell-like. These distributions occur at much smaller Z values than for the model of *Onsager et al.* [1991]. This is because the new model purposefully consists of very stretched magnetic field lines that result in beam-like distributions occurring closer to the NS.

What will now be demonstrated is the reverse of the procedure adopted by *Onsager et al.* [1991]. Instead of specifying the boundary condition in the model neutral sheet, and then finding the distributions in the PSBL, what is proposed here is to specify the boundary condition in the PSBL, and then to calculate the ion distributions in the model CS region.

5.2 A novel boundary condition

Ion beams in the PSBL appear to exist independent of substorm phase [*Lui et al.*, 1983; *Eastman et al.*, 1984], while non-Maxwellian distribution functions are actually rather common in the CPS, especially during substorms. Therefore, instead of specifying the boundary condition in the model CPS, and then finding the distributions in the PSBL, what is proposed here is to specify the boundary condition at higher latitudes, including the PSBL, and then to model the ion distributions in the CPS, especially around the CS region. Since the primary interest in this work is to determine whether fast tailward flows in the CPS can arise as a natural result of PSBL dynamics, a boundary condition which is the antitype of the *Onsager et al.* [1991] case will be introduced. The model boundary condition is constrained by satellite data and previous theoretical studies. What is implicitly assumed is that the magnetic field, that has been previously modelled, is more accurate than any other

magnetotail property. The model electric field has also been pre-selected based on observations. The picture is completed by selection of the energies and properties of the boundary distribution functions.

5.2.1 PSBL/mantle/lobe distributions

The model boundary condition is specified in space as the last closed magnetic field line in the noon-midnight meridian ($Y=0$) which crosses the NS at $X=-100 R_E$, as shown schematically in Figure 5.2. *Eastman et al.* [1998] used the GEOTAIL dataset to demonstrate that the probability of observing the plasma mantle increases with distance downtail, from 18% near the earth to about 50% near $205 R_E$. On the other hand, intervals during which the plasma sheet is detected, including the CPS and PSBL, decrease with increasing tailward distance. Pure lobe occurrences also decrease in observation probability with distance downtail.

To take this reality into account the model boundary condition takes the form of ion distribution functions that are PSBL- and lobe-like near the earth but become increasingly mantle-like with downtail distance. This is schematically represented in Figure 5.2. The model boundary condition (BC) – viz. the ion distribution function – comprises two components: a beam component featuring motion towards the earth, and a core component that has a small field-aligned drift.

In a recent model of the PSBL, *Ashour-Abdalla et al.* [1993] demonstrated that the PSBL ion density decreases with distance downtail. Therefore, as the distance from the earth increases, the density of the beam term decreases. This is also consistent with the fact that the probability of observing the PSBL decreases with downtail distance [*Eastman et al.*, 1998], assuming that the beam density drops below the detector threshold. *Ashour-Abdalla et al.* [1991a, 1993] demonstrated that

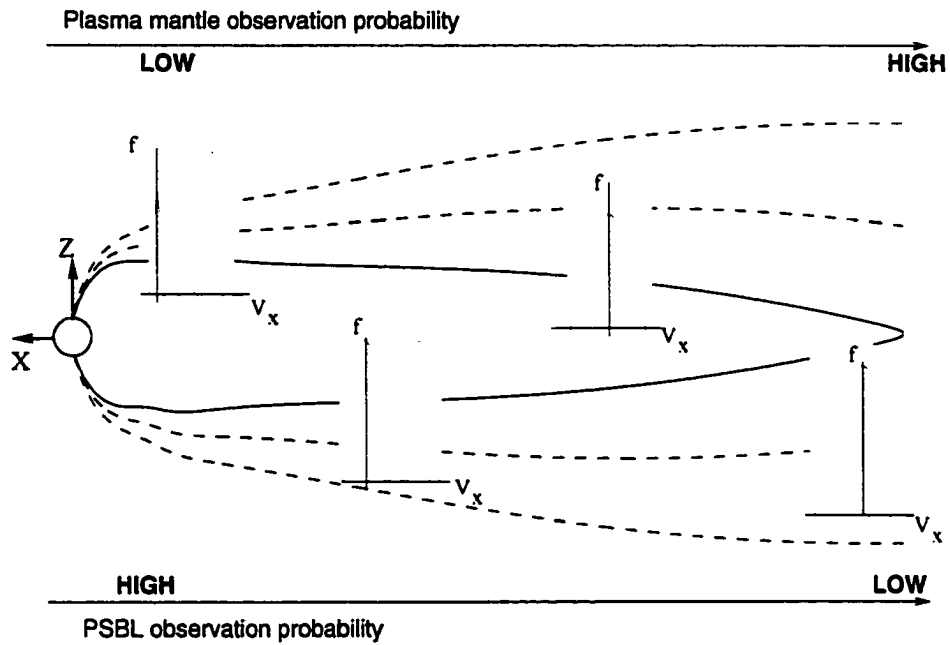


Figure 5.2: A schematic diagram showing the model boundary, which is the magnetic field line which crosses the NS at $X=-100 R_E$ (solid line). The probability of observing mantle/PSBL plasma increases/decreases with distance downtail. Model velocity distribution functions at various positions along the boundary are shown as line drawings with the ordinate corresponding to phase space density and the abscissa to the earthward velocity, V_x .

small scale "beamlets" can develop in the beam component. However, these small scale features are likely to be quickly smeared by wave-particle interactions, to form a single solid, homogeneous ion beam [Schriver *et al.*, 1991]. Accordingly, only a single solid bi-Maxwellian distribution is used for the beam component, with $T_{\perp}/T_{\parallel} = 5$, which is consistent with observations [DeCoster and Frank, 1979; Eastman *et al.*, 1984]. The drift speed of the beam component is allowed to vary along the boundary, fastest near the earth, and slowest in the distant tail. It is allowed a maximum of $V_b \approx 1200 \text{ km/s}$, at $X = -10 R_E$, which is a reasonable value [Eastman *et al.*, 1984], although faster PSBL beams can exist. The reasonable beam parameters chosen have $V_{bth\parallel} \sim 0.08V_b$ [Eastman *et al.*, 1984], where $V_{bth\parallel}$ is the thermal velocity in the magnetic field direction, and V_b is the beam speed.

The various beam parameters are shown as the dashed curves in Figure 5.3. All the variables are allowed to vary linearly between the values chosen at $X = -10$ and $-100 R_E$. The appropriate parameters for the core term are shown as the solid curves in Figure 5.3. Near the earth the core term is cold, and represents lobe ions ($T_{\perp} = 25 \text{ eV}$). The temperature ratio is $T_{\perp}/T_{\parallel} = 2$, which is a reasonable choice [Rosenbauer *et al.*, 1975]. Also, the density is very low in the near-earth ($n = 0.02 \text{ cm}^{-3}$). It increases linearly with distance downtail in order to simulate a transition between pure-lobe to more mantle-like plasma. At $X = -100 R_E$ the core term has $n = 0.11 \text{ cm}^{-3}$ and $T_{\perp} = 560 \text{ eV}$.

The complete model BC near the earth is typical for the outer edge of the PSBL. Since the variables vary linearly downtail, a region in the midtail exists where the core of the distributions is intermediate between mantle-like and lobe-like. In the distant tail, the beam term is negligible, and the complete boundary condition is a mantle-like ion distribution. The magnetic field model used here is defined for growth phase, during which time the mantle becomes an especially important source

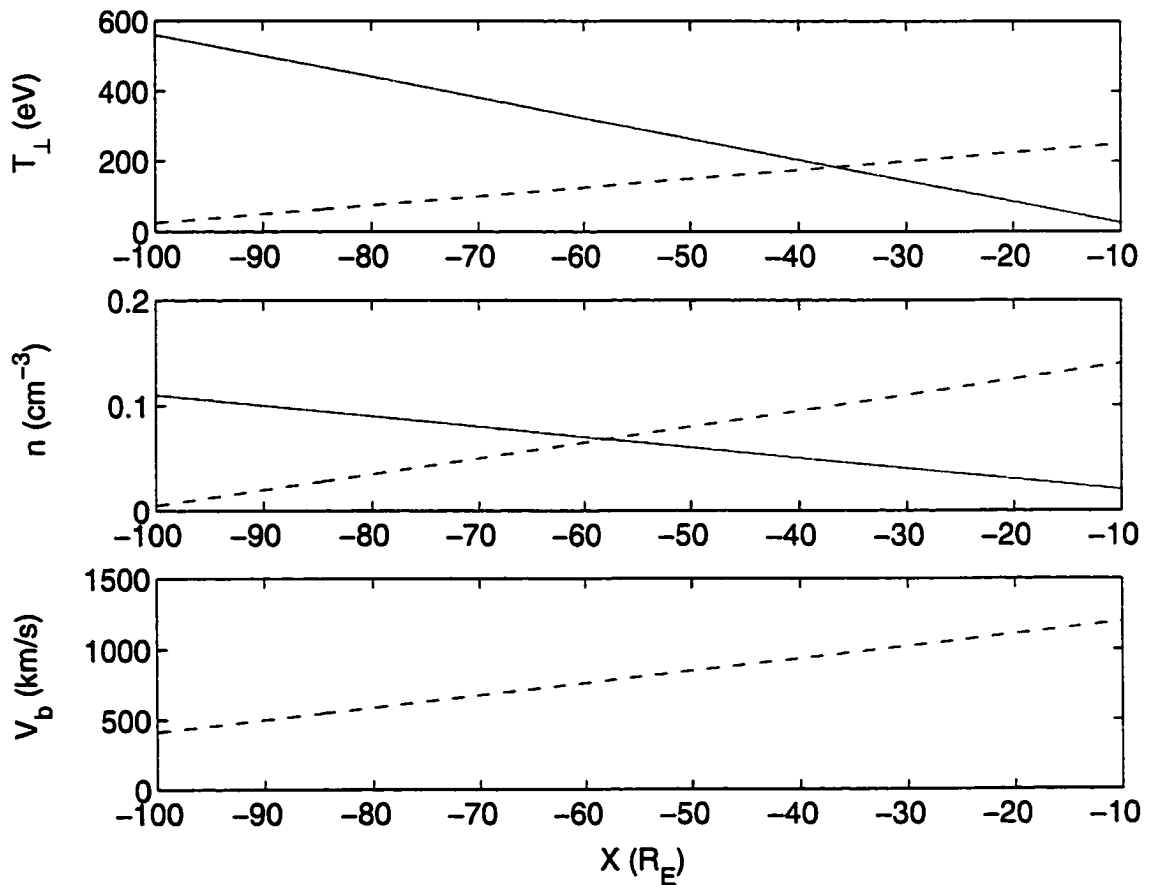


Figure 5.3: Model variables against downtail position for (top) the perpendicular temperature (T_{\perp}), (middle) number density (n), and (bottom) velocity (V_b) are shown for the core term (solid curves) and the beam term (dashed curves).

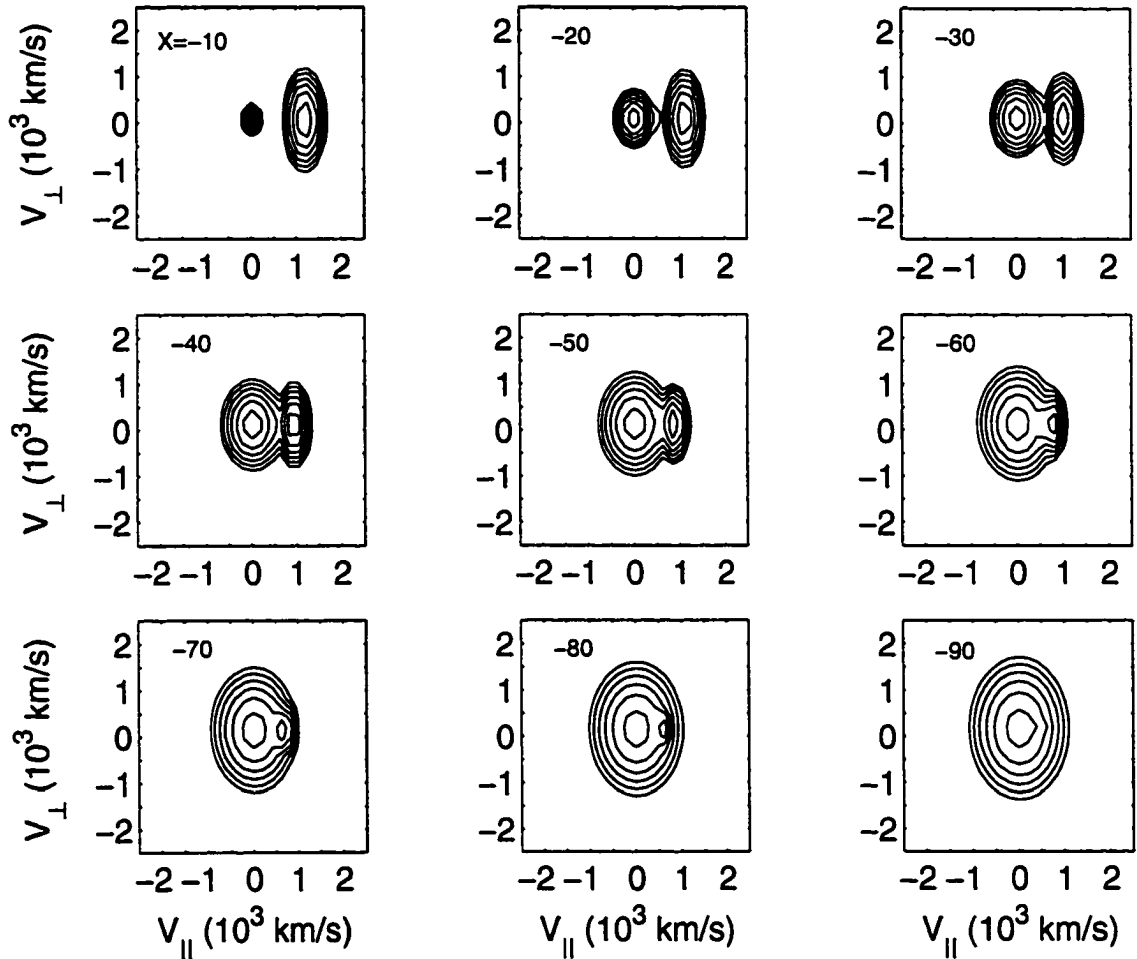


Figure 5.4: Two-dimensional cuts in the $V_{||} - V_{\perp}$ plane of the model boundary condition (BC) distribution functions at different downtail positions for positive Z . The $V_{||}$ direction is earthwards. In the near-earth region the distributions are representative of the outer edge of the PSBL. In the midtail region the distributions are representative of an intermediate region including lobe-mantle plasma. The distant tail is representative of an almost pure mantle BC. The contours of constant phase space density are plotted every two decades from -23 to $-10 \text{ s}^3/m^6$.

of PS plasma [*Liu and Hill, 1990*]. Figure 5.4 shows the sequence of distributions at different X -positions along the model boundary.

Although the model BC does not include sources other than the PSBL-lobe-mantle sources, the use of this approach does not mean that other valid possibilities are not recognised. For example, there is little doubt that part of the plasma sheet population (e.g. O^+) comes from the ionosphere. However, it is assumed here that the different sources act independently, and the focus is on the population of the tail that comes from the sources specified. Ionospheric sources are most important in the near-tail, while sources from the plasma mantle are more appropriate further downtail [*Ashour-Abdalla et al., 1993*].

5.3 Ion distributions from 'zeroth order' test particle simulations

By 'zeroth-order' is meant that all complicated effects are ignored, other than the simple single-particle motion associated with the time-independent electric and magnetic fields. In this section model distributions are calculated at various locations throughout the model magnetotail, from $X=-15 R_E$ to $-90 R_E$, using the BC parameters as described above.

5.3.1 PSBL/CPS region

In Figure 5.5 typical model PSBL ion distributions are shown at various distances above the NS. The velocities are expressed in terms of the direction of the magnetic field (V_B), electric field (V_E), and convection (V_C). Each distribution function is

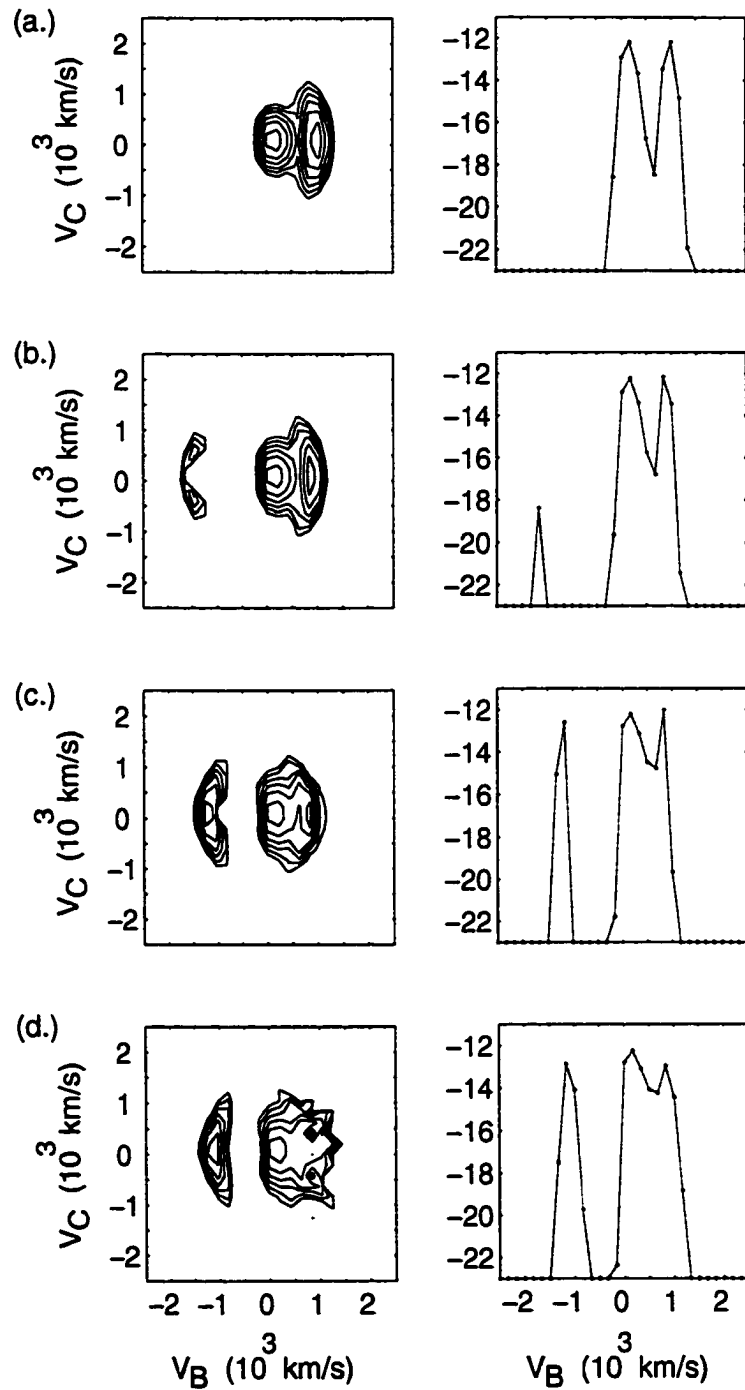


Figure 5.5: Model ion velocity distributions shown as (left column) two-dimensional distributions in the V_B - V_C plane, and (right column) cuts in the V_B direction ($V_C=0$) at four locations in the noon-midnight meridian, (a.) $Z=3.2$, (b.) 2.25 , (c.) 0.75 , and (d.) $0.3 R_E$, all at $X=-20 R_E$.

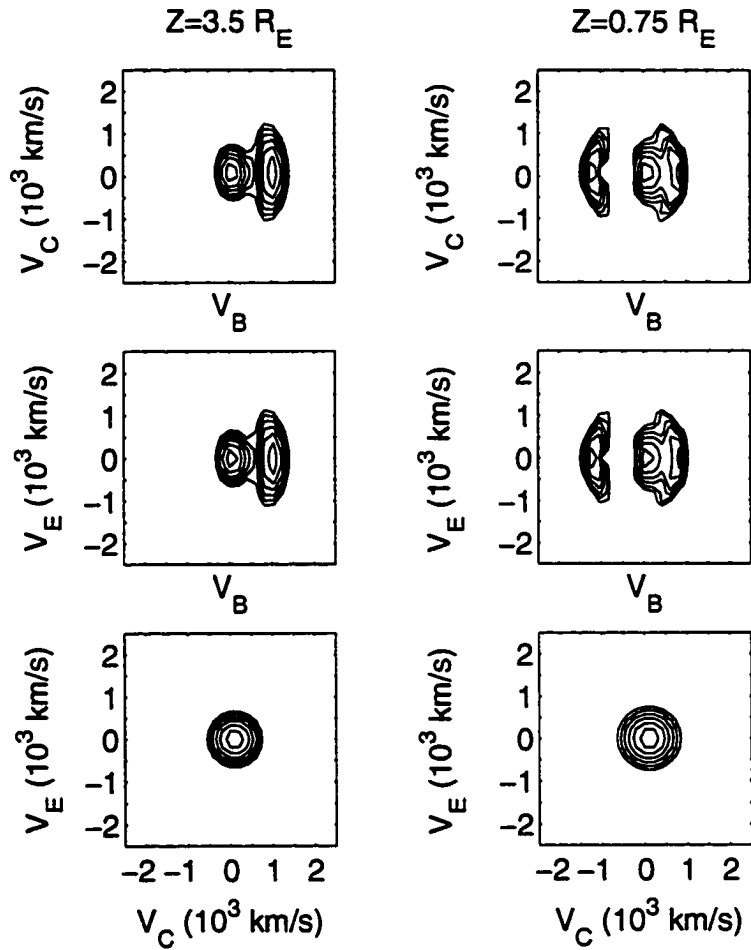


Figure 5.6: Two dimensional cuts through model distribution functions calculated at $X=-20 R_E$ and (left column) $Z=3.5 R_E$ and (right column) $Z=0.75 R_E$. The velocities are expressed in terms of the direction of the magnetic field (V_B), electric field (V_E), and convection (V_C). The top row shows the cut in the $V_B - V_C$ plane, the middle row shows the cut in the $V_B - V_E$ plane, and the bottom row is the cut in the $V_C - V_E$ plane.

calculated at $X=-20 R_E$ in the noon-midnight meridian at different Z locations. The left column shows the distributions in two-dimensional cuts in the $V_B - V_C$ plane, and the right column shows cuts in the V_B direction. The two-dimensional distributions show contours of constant phase space density, with contours every two decades from -23 to $-10 s^3/m^6$. All these distributions are calculated quite far from the NS, so the magnetic field is almost entirely in the X -direction. Thus V_B corresponds approximately to the earthward direction, and V_C corresponds to the $-V_z$ direction.

Of course, immediately equatorward of the model boundary the model BC is recovered, viz. a cold core plus an earthward streaming beam with drift velocity of ≈ 1200 km/s. This is typical for the outer edge of the PSBL. Figure 5.5a illustrates the distributions deeper in the boundary layer, at $Z=3.2 R_E$. Here, the earthward beam is still present, but its distribution function has begun to assume a "kidney bean" shape. At $Z=2.25 R_E$ both earthward and tailward streaming ions are observed, with the tailward ions at slightly higher speeds than the earthward streaming ions. The perpendicular temperature of the tailward beam is slightly smaller than that for the earthward beams. Also, at this location both beam distributions appear somewhat "kidney bean" shaped, due to their velocity space mapping into a region of increasing magnetic field strength, as described by *Onsager et al.* [1991]. The ion core has a higher phase space density than the beams, and the earthward beam ($+V_B$) has a higher phase space density than the tailward beam.

At $Z=0.75 R_E$ the earthward beam is still present, but has a lower field-aligned drift velocity, and is colder in the perpendicular direction. At this point the tailward beam has a larger perpendicular temperature than the earthward beam. Its phase space density continues to increase towards lower latitudes. Still closer to the NS, at $Z=0.3 R_E$, the earthward beam has a lower phase space density than the tailward beam.

In summary, the distributions are all characteristic of the PSBL, with a core component, and with the beam components having $T_{\perp}/T_{\parallel} > 1$. Initially only earthward beams are observed; slightly deeper in the model boundary layer a counterstreaming beam is observed. The counterstreaming beam consistently has a larger field-aligned drift velocity than its earthward counterpart. When it is first observed, the counterstreaming beam has a perpendicular temperature that is smaller than that of the earthward beam. However, closer to the NS its perpendicular temperature is larger than that of the earthward beam. Finally, only the tailward beam is clearly observed, and the earthward beam has a lower phase space density. Figure 5.6 shows different two-dimensional cuts of the full velocity distribution functions calculated at $Z=3.5, 0.75 R_E$. The top row shows the cut in the $V_B - V_C$ plane for the two different Z -positions. The slight drift velocity in the V_C direction is evident in this cut. However, the second row indicates that there is almost no drift in the V_E direction. The third row shows the $V_C - V_E$ cuts. The distribution function is isotropic in this plane, and only the slow convective drift is evident. As can be seen from the preceding figures, the velocity distributions in the CPS can have complicated forms, including asymmetry and counterstreaming. This is contrary to the general view that the CPS is a region of hot isotropic ions, and is similar to previous simulation results [Ashour-Abdalla *et al.*, 1993], and consistent with observations of counterstreaming near the NS [Eastman *et al.*, 1984; Nakamura *et al.*, 1991]. It also demonstrates that PSBL-like distribution functions can occur deep in the CPS.

Several initial positions in velocity space were selected in order to determine the behaviour of particles comprising the core and beam components of the distribution. Figure 5.7 shows examples of representative proton orbits for different initial positions in velocity space. The upper figure shows the model two-dimensional ion velocity distribution in the $V_B - V_C$ plane, calculated at $(X, Y, Z) = (-20, 0, 1) R_E$. The

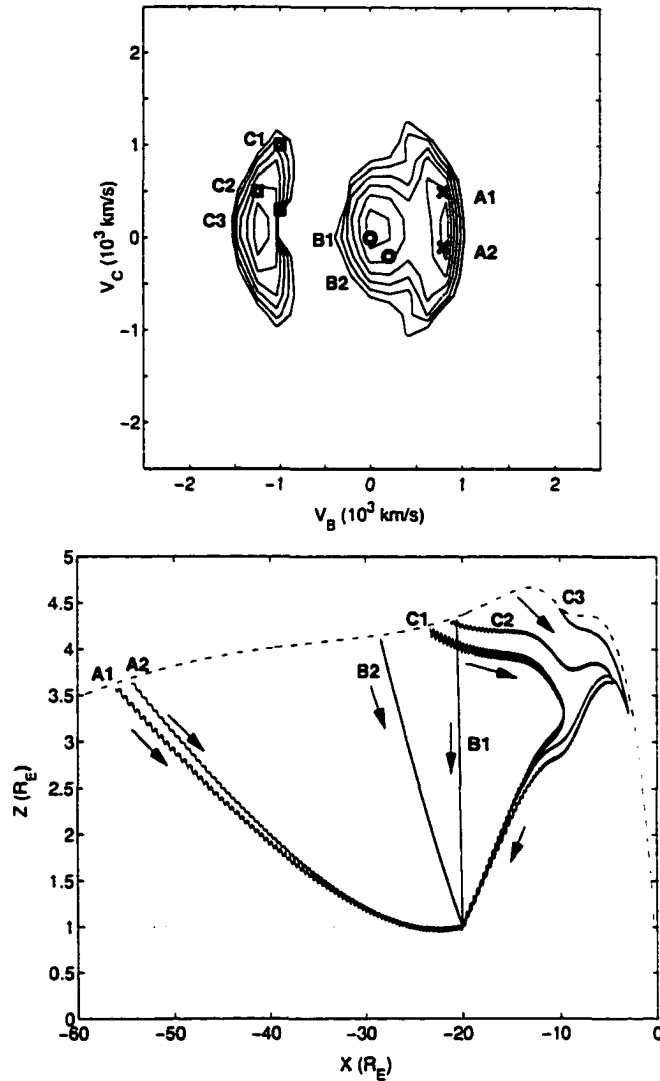


Figure 5.7: (Top) Model two-dimensional ion velocity distribution in the $V_B - V_C$ plane, calculated at $(X, Y, Z) = (-20, 0, 1) R_E$. Several initial positions in velocity space are selected in order to demonstrate the representative behaviour of particles comprising the core and beam components of the distribution. The particles comprising part of the earthward moving beam are labelled with crosses and points A1, A2. The sample particle orbits from the core component are labelled as circles and B1, B2. For the counterstreaming component the labels are squares and C1, C2, C3. The lower figure shows the trajectory traces corresponding to the initial conditions chosen in the upper figure. Arrows show the direction of particle motion.

position in velocity space of particles comprising part of the earthward moving beam are labelled with crosses and A1, A2. For the core component the labels are circles and B1, B2. For the counterstreaming component the labels are squares and C1, C2, C3. The lower figure shows trajectory traces corresponding to the initial conditions chosen in the upper figure. The protons from the core component map to the core term in the model BC (see Figure 5.4). Therefore, they retain the essential features of the core part of the distribution function at the model boundary. The particles forming the earthward beam come from further downtail and have arrived at the observation location after convection under the model electric field. They map to the earthward beam BC, and have a large field aligned component of velocity throughout their motion from source to observation point. Particles comprising the counterstreaming beam also map to the earthward beam part of the source distribution, but mirror in the dipolar magnetic field near the earth, whereafter they continue to convect towards the midplane until they reach the observation point. Since particles are transported by convection to lower latitudes, the tailward beams are observed closer to the NS than their earthward counterparts.

Results from moment calculations

Figure 5.8 shows moments calculated from the full three-dimensional velocity distribution functions computed at various Z -values at $X=-20 R_E$. The density slowly increases from the model boundary (at $Z=4.4 R_E$) to about $Z=3.5 R_E$. This increase in density is due to the slow heating of the plasma while there is only a small decrease in the maximum phase space density of the different components. The distribution function of the earthward beam becomes somewhat "kidney bean" shaped, contributing to this effect. At lower latitudes the observed earthward beam has lower phase space density and velocity, and the temperature becomes somewhat cooler (cf.

Figure 5.5). Thus, between about $Z=3.5-2.5 R_E$, where the earthward beam term is decreasing rapidly in phase space density, the overall particle density decreases. At $Z \approx 2.5 R_E$ the counterstreaming beam is easily identifiable in the distribution function. At first the counterstreaming beam is very weak, and contributes little to the overall particle density, but as one moves to lower latitudes the temperature and phase space density of the tailward beam increase, which results in a slight increase in total particle density. The average density from the model boundary to the NS is about 0.1 cm^{-3} .

The velocity moments are shown in the lower plot of Figure 5.8. The velocities are plotted in terms of the magnetic field (V_B), electric field (V_E), and convection (V_C) directions. At large Z -values $V_B \approx 900 \text{ km/s}$ and decreases steadily towards lower latitudes. This steady decrease in V_B corresponds to the slow decrease of the drift velocity of the earthward beam at lower latitudes. Below $Z \approx 3.2 R_E$ the decrease is faster, due to the appearance of the tailward beam. At $Z=2.0 R_E$ the tailward beam is well developed and results in the overall bulk $V_B < 300 \text{ km/s}$. Between $0.5-2 R_E$ only a very small magnitude flow is observed in the V_B moment even though there are very fast counterstreaming beams in the distribution functions. Soon the tailward beam dominates the distribution function and results in negative V_B . The model predicts that PSBL-like signatures can be observed deep in the CPS. Thus, qualitatively, there is very little difference between the PSBL and CPS ion distributions. The model V_C and V_E are very constant. The V_C component is almost identical to the predicted convection velocity from $(\vec{E} \times \vec{B})/B^2$ ($\sim 100 \text{ km/s}$), and the V_E component is zero.

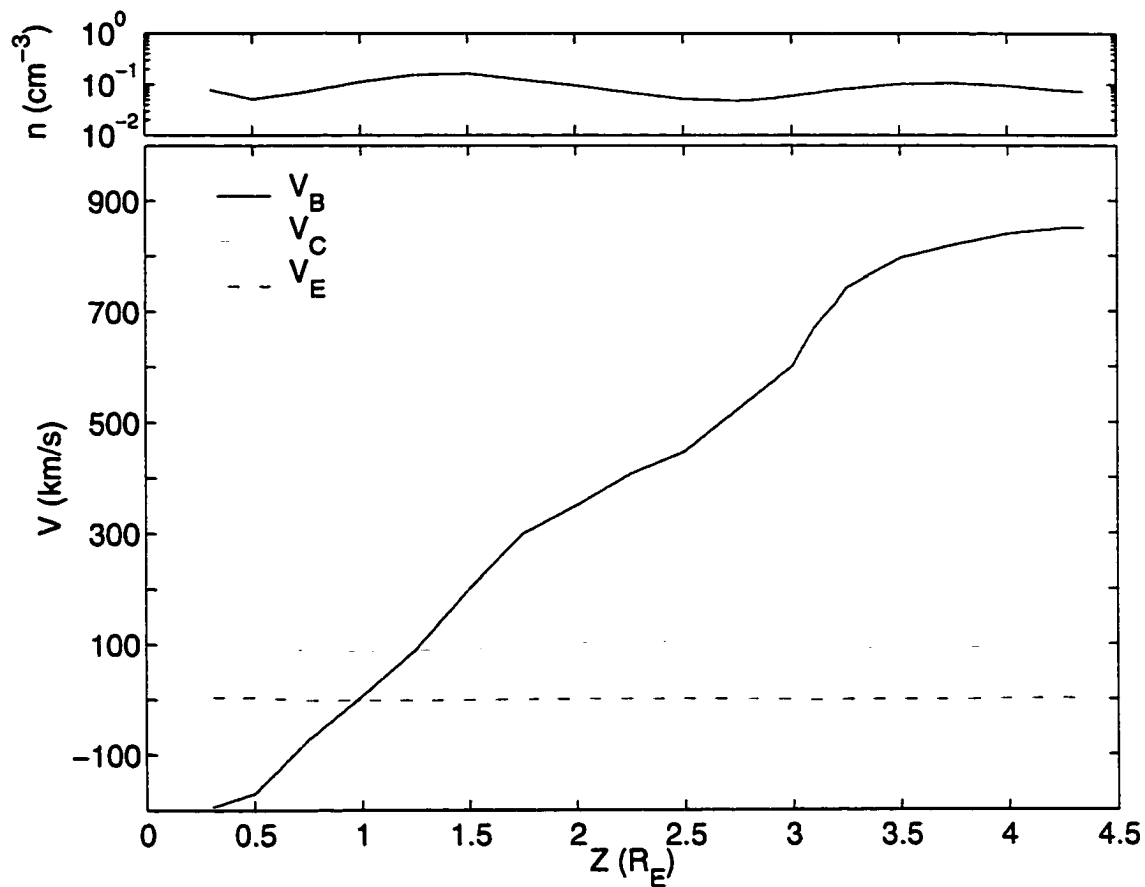


Figure 5.8: Model (top) number density and (bottom) velocity moments calculated at various Z -distances from the NS at $X=-20 R_E$. The velocities are expressed in terms of the directions of the magnetic field (V_B), electric field (V_E) and convection (V_C).

5.3.2 CS region

In this section the behaviour of the distribution functions in the CS is considered. To ensure that distributions are in the CS region, they were all calculated at $Z = 0.0001 R_E$. Figure 5.9 shows two-dimensional cuts of the model distribution functions in the $V_B - V_C$ plane. Each distribution function is calculated in the CS, for the noon-midnight meridian, and at different X -positions, which are indicated in each of the subplots. At these CS region locations, $V_B \approx V_z$ and $V_C \approx -V_x$. Near the earth, in general, the CS distribution functions comprise a quasi-isotropic core term, as well as phase space density enhancements in the $-V_C$ direction (tailwards). Beyond approximately $X = -35 R_E$, the distribution function comprises only a core term. The core term has $T_{\parallel}/T_{\perp} > 1$, and the ratio increases with downtail distance. The phase space density enhancements in the $-V_C$ direction, which will be called convective phase space density enhancements (CPSDE), are largest between about 20 and 30 R_E downtail. The sequence of distribution functions in Figure 5.9 indicates that the presence of the CPSDE may perhaps yield tailward flows.

Figure 5.10 shows a (top) model two-dimensional ion velocity distribution in the $V_B - V_C$ plane, calculated at $(X, Y, Z) = (-24, 0, 0.0001) R_E$. Several initial positions in velocity space are selected in order to demonstrate the representative behaviour of particles comprising the different components of the distribution function (crosses, circles, squares). Particles from the CPSDE regions are labelled 1-4. The CPSDE at negative/positive V_B is formed from mirrored ion beams that initially come from the northern/southern hemisphere. The phase space density of the negative V_B CPSDE is slightly higher than its $+V_B$ counterstreaming counterpart. The lower figure shows the trajectory traces corresponding to the initial conditions chosen in the upper figure. The magnetic moment for one of these particles, with velocity at

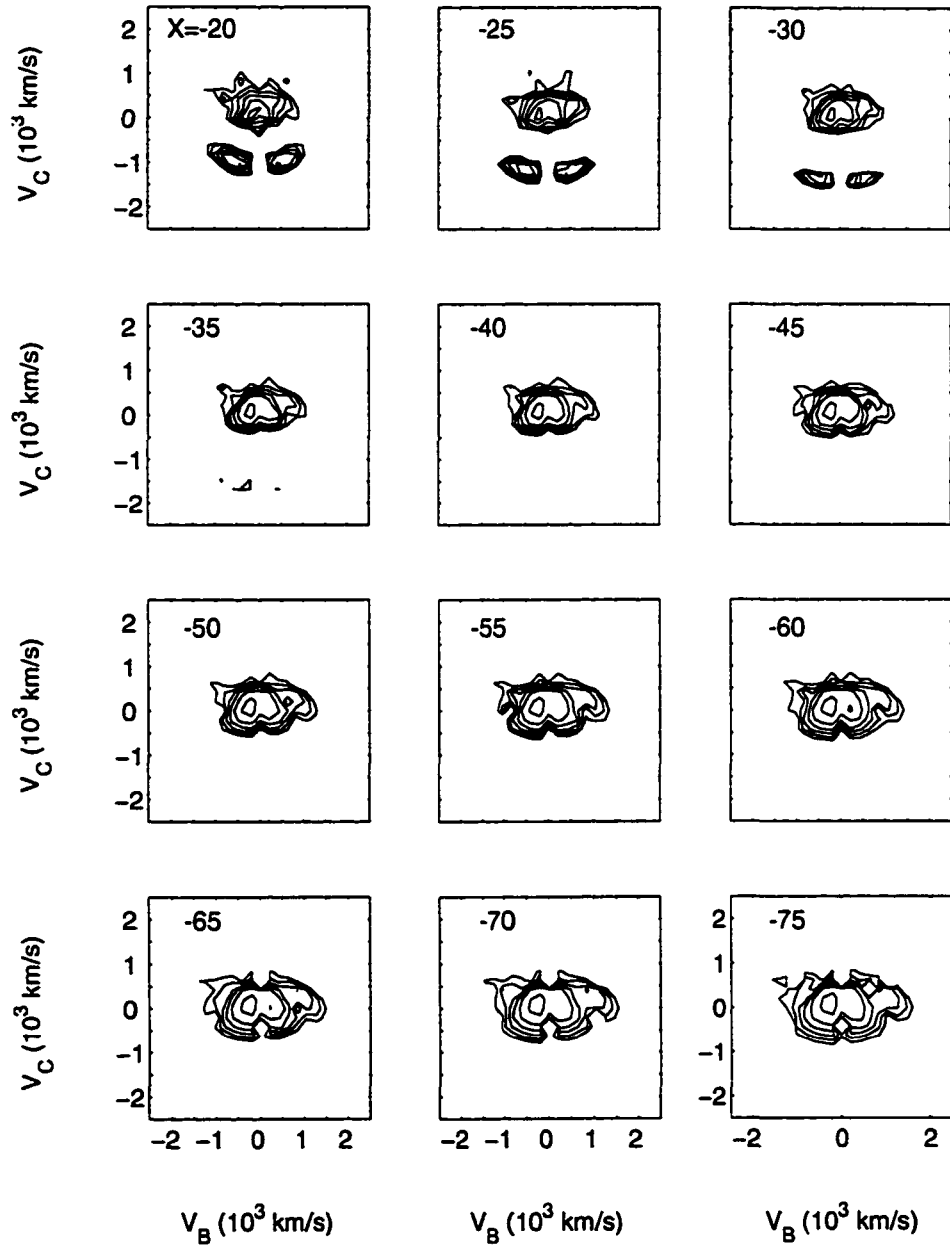


Figure 5.9: Model ion velocity distributions distributions shown as two-dimensional distributions in the V_B - V_C plane. The distribution functions are plotted for different downtail positions, from $X = -20 R_E$ to $-75 R_E$. The X -positions are indicated in each subplot.

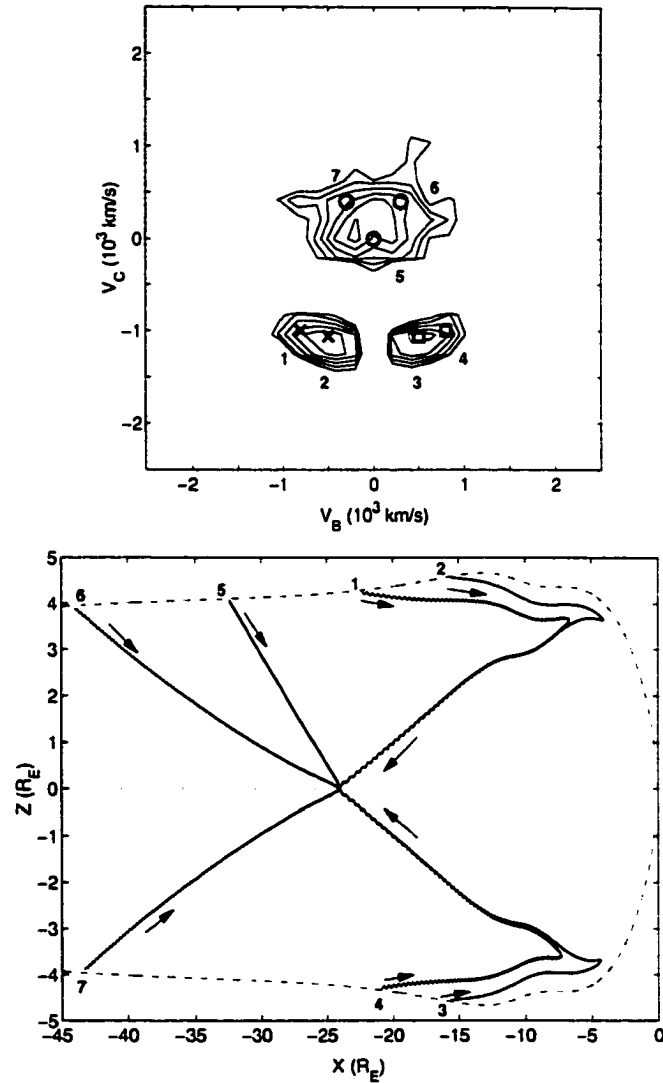


Figure 5.10: (Top) Model two-dimensional ion velocity distribution in the $V_B - V_C$ plane, calculated at $(X, Y, Z) = (-24, 0, 0.0001) R_E$. At this location $V_B \approx V_z$ and $V_C \approx -V_x$. Several initial positions in velocity space are selected in order to demonstrate the representative behaviour of particles comprising the different components of the distribution function. Particles from the convective phase space density enhancements (CPSDE), are labelled 1-4. The CPSDE at negative/positive V_B is formed from mirrored ion beams that initially come from the northern/southern hemisphere. The phase space density of the negative V_B CPSDE is slightly higher than its $+V_B$ counterstreaming counterpart. The lower figure shows the trajectory traces corresponding to the initial conditions chosen in the upper figure. Arrows show the direction of particle motion.

the observation location of $(V_B, V_C, V_E) = (500, -1060, 0)$ km/s is shown as the dashed-dot line in Figure 5.11. The solid line, corresponding to the left ordinate, shows the trajectory trace in the $X - Z$ plane. The magnetic moment is well conserved until the particle reaches $Z \approx -0.02 R_E$. It becomes unmagnetised at this point and the conservation of the magnetic moment is subsequently violated as the particle moves through the thin current sheet to the observation location.

Figure 5.12 shows two-dimensional cuts for the distribution calculated in the CS region at $X = -22 R_E$. The top row shows cuts in the $V_B - V_C$ plane at $V_E = 0$ km/s (left) and 200 km/s (right). The middle row shows cuts in the $V_B - V_E$ plane at $V_C = 0$ km/s (left) and 200 km/s (right), and the bottom row shows cuts in the $V_C - V_E$ plane at $V_B = 0$ km/s (left) and 200 km/s (right). The middle row, with cuts in the $V_B - V_E$ plane, shows that the CPSDE components extend to the positive V_E plane. Thus the ions comprising the CPSDE begin to gain significant momentum in the V_E direction once demagnetisation has occurred in the CS region.

Results from moment calculations

The density and velocity moments are calculated for the CS, and shown in Figure 5.13. The upper plot shows the density plotted as a function of downtail position in the CS region. In the distant tail the density is slightly lower than 0.1 cm^{-3} , and decreases slowly until about $X = -30 R_E$. The decrease in density towards the earth occurs in the region where only the core term exists (cf. Figure 5.9). As was shown in the previous section, the core term at the observation location maps to the core component of the distribution function at the model boundary. Since the model BC used here has the core term becoming warmer and more mantle-like with distance from the earth, it follows that the density would slowly decrease closer to the

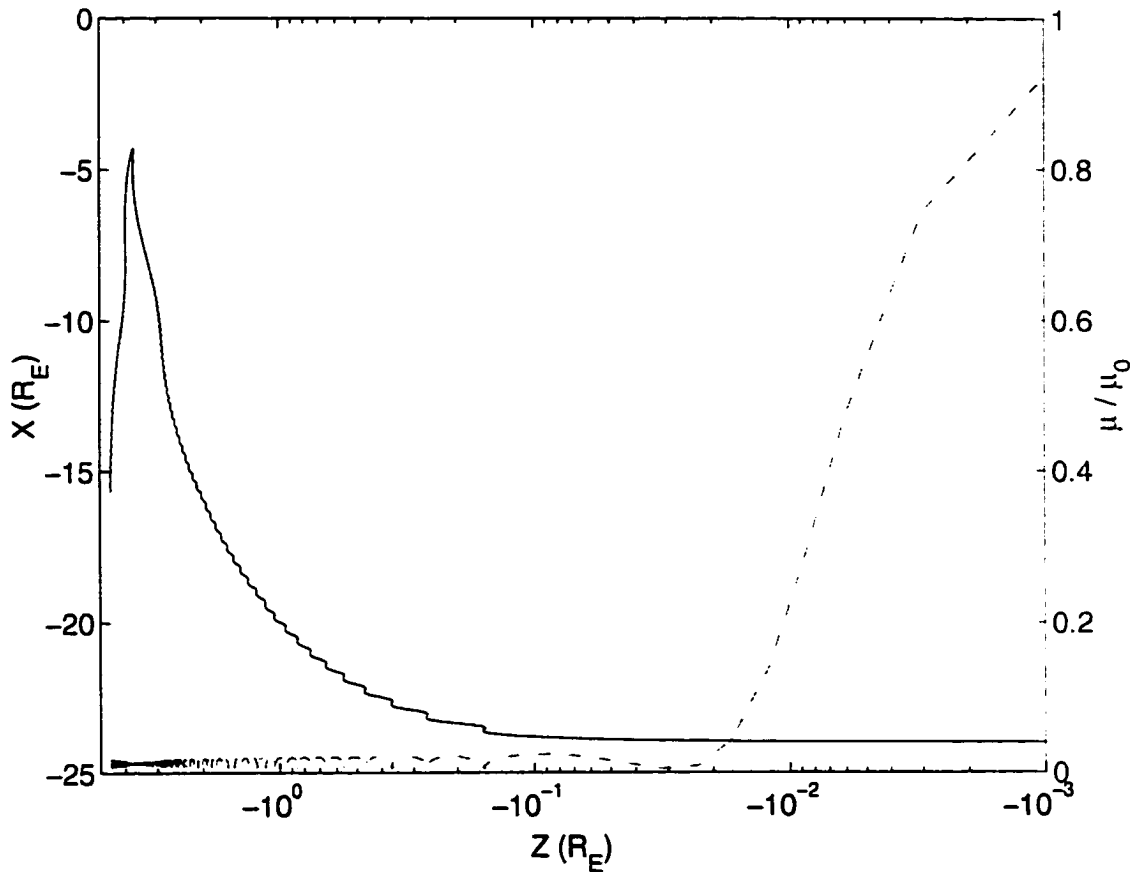


Figure 5.11: The trajectory of a particle in the $X - Z$ plane is shown (left ordinate, solid line) as a reference against which to compare the variation of the magnetic moment (μ) which is the dashed-dot line and right ordinate. The magnetic moment is normalised. The particle comes from the model boundary in the southern hemisphere, and arrives at the observation location at $(X, Z) = (-24, 0.0001) R_E$ with a velocity $(V_B, V_C, V_E) = (500, -1060, 0) km/s$.

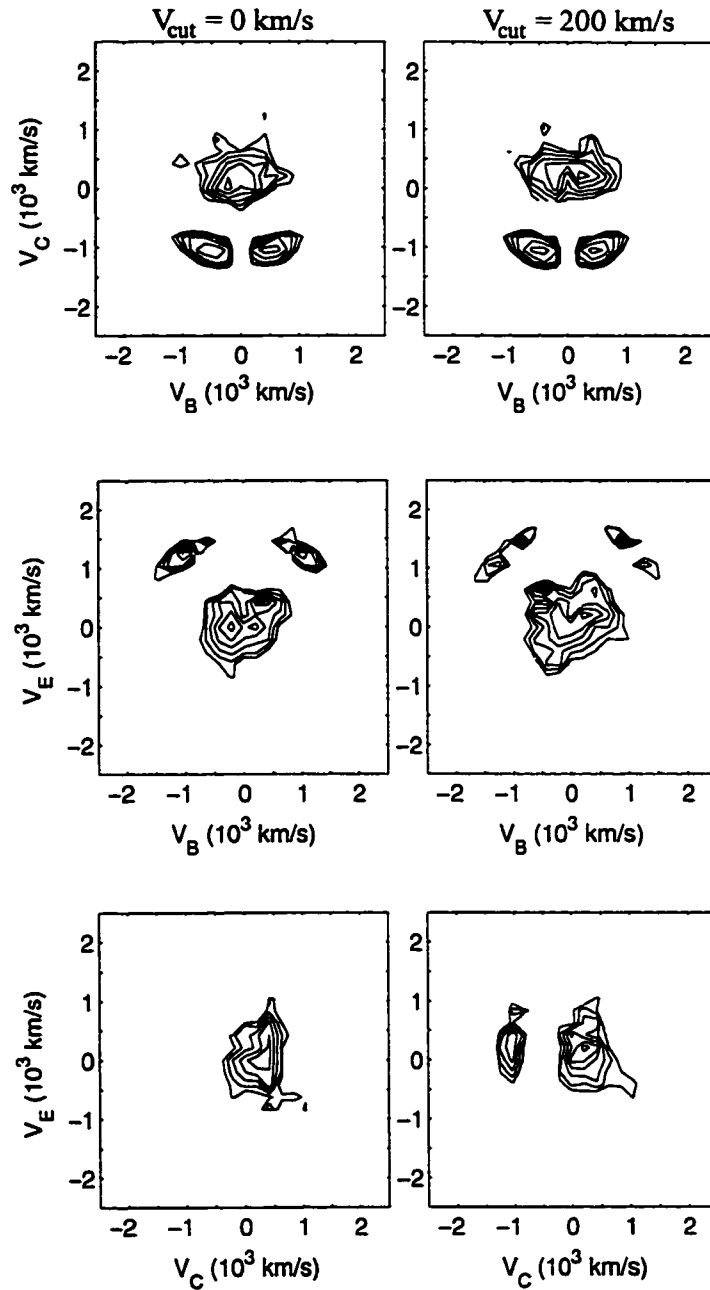


Figure 5.12: Two dimensional cuts of the model velocity distribution calculated at $(X, Z) = (-22, 0.0001) R_E$. The velocities are expressed in terms of the directions of the magnetic field (V_B), electric field (V_E) and convection velocity (V_C). The top row shows cuts in the $V_B - V_C$ plane at $V_E = 0 \text{ km/s}$ (left) and 200 km/s (right). The middle row shows cuts in the $V_B - V_E$ plane at $V_C = 0 \text{ km/s}$ (left) and 200 km/s (right). The bottom row shows cuts in the $V_C - V_E$ plane at $V_B = 0 \text{ km/s}$ (left) and 200 km/s (right). At this location $V_C \approx V_x$, $V_B \approx V_z$, $V_E \approx V_y$.

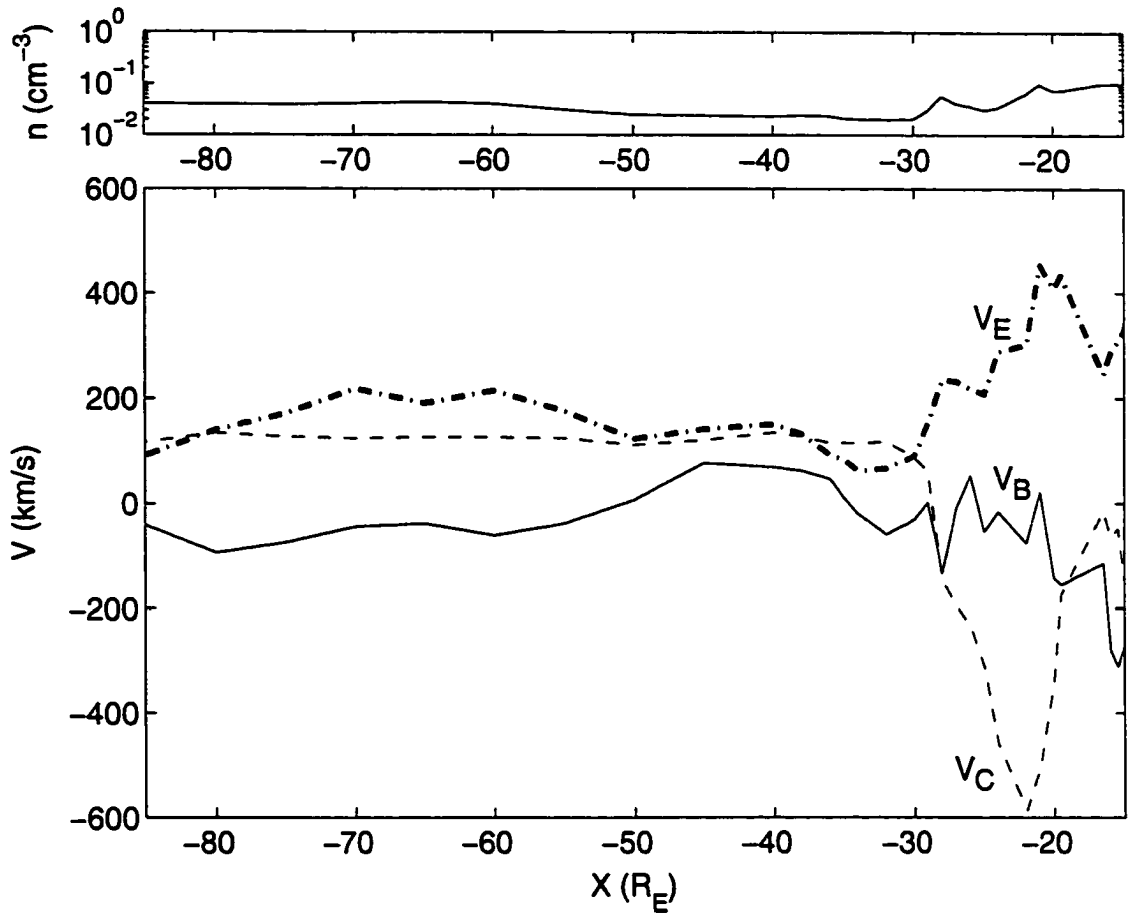


Figure 5.13: Model (top) density and (bottom) velocity moments calculated in the magnetotail CS region ($Z = 0.0001 R_E$) in the noon-midnight meridian. The velocities are expressed in terms of the directions of the magnetic field (V_B), electric field (V_E) and convection velocity (V_C). At these locations in the CS region $V_C \approx V_x$, $V_B \approx V_z$, $V_E \approx V_y$.

earth. At $X = -30 R_E$ the CPSDE terms, which come from the mirrored beams, are well developed and clearly seen in the distribution functions (Figure 5.9). It is these components that contribute to the increasing ion density in the near-earth region.

The velocity moments are even more interesting. The component along the magnetic field direction, V_B , is typically very small. Whereas in the distant tail it is slightly negative, in the midtail it becomes slightly positive, and in the near tail, closer than about $30 R_E$, it becomes quite variable but with a negative average. This is because of the CPSDE terms; the phase space density of the negative V_B term is slightly higher than its $+V_B$ counterpart, resulting in an overall negative V_B drift. The $V_E (\approx V_y)$ term is positive for all distances from the earth. This is due in part to particle trapping in the crosstail current sheet, and subsequent motion in the electric field direction. Increased trapping occurs between $20-30 R_E$, leading to larger V_E in this region. Of greatest interest is the V_C term, which is fairly constant downtail of about $30 R_E$. However, once the CPSDE components appear in the distribution functions, they contribute to negative V_C , viz. tailward flows. At about $X = -22 R_E$ the velocity $V_C \sim -570 \text{ km/s}$. Still closer to the earth the phase space density of the CPSDE becomes lower and V_C begins to increase to smaller values.

Figure 5.14 shows the earthward velocity moment plotted for three different current sheet half-thicknesses. $L_z = 1$ corresponds to the magnetic field model used thus far. Tailward flows are still present for a rather thick current sheet ($L_z = 11$), but are absent by the time $L_z = 19$. For the $L_z = 11$ case the region over which tailward flows occur is narrower, and the minimum is also smaller than for the $L_z = 1$ case. This means that although tailward flows are not as strong for thicker current sheets, one could expect to observe such flows during much of the course of the growth phase, while the current sheet is thinning.

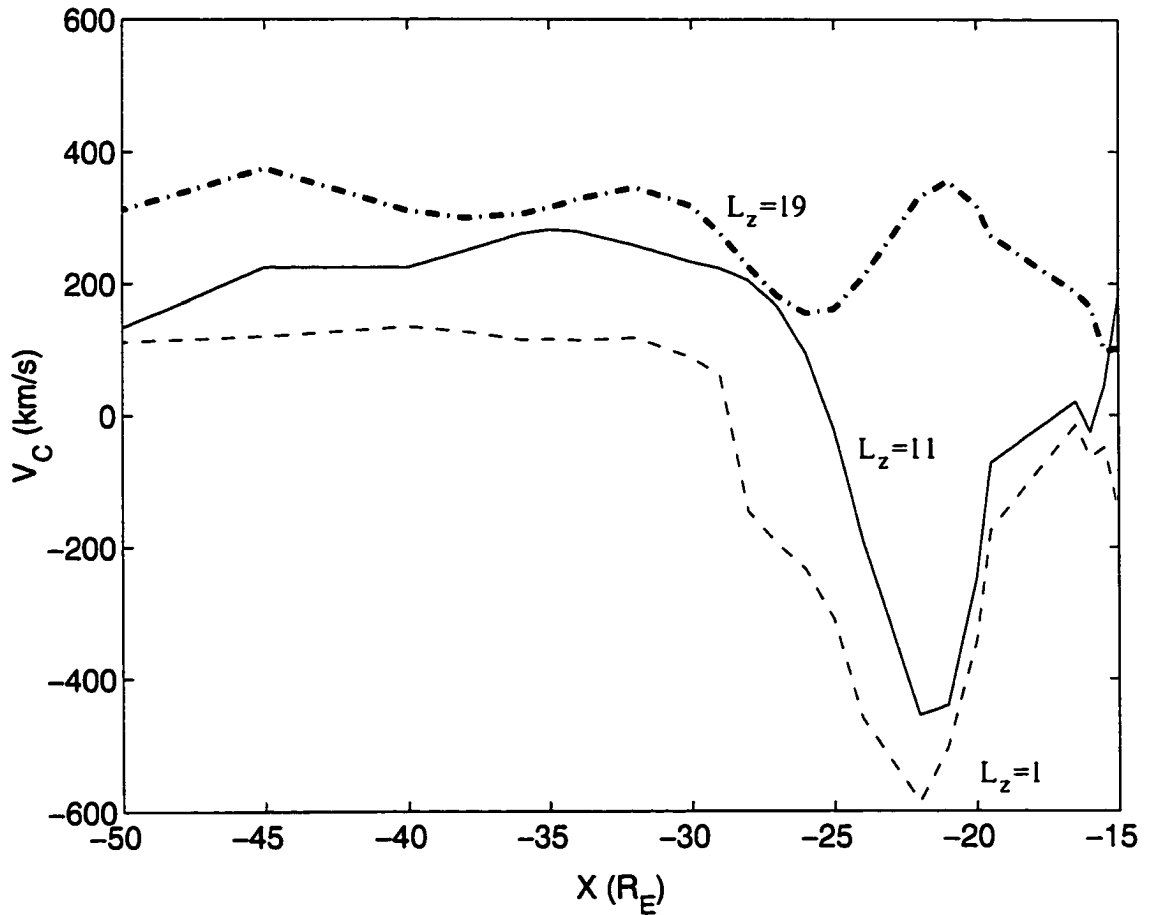


Figure 5.14: Model velocity moments in the V_C ($\approx V_x$) direction calculated in the magnetotail CS region ($Z = 0.0001 R_E$). The moments are shown for three different current sheet half-thickness parameters ($L_z = 1, 11, 19$). L_z has been normalised to the model value selected in the previous chapter, viz. $L_z = 1 \equiv 0.05 R_E$.

5.4 Model of electrostatic noise

The results from the test particle simulations of the CPS show that the velocity distributions contain complicated forms, including asymmetries and counterstreaming; the ion distributions computed in the CS region include complicated tailward CPSDE components. Whether all of these features occur in the real magnetotail remains to be demonstrated through experimental observations of ion distribution functions measured during late growth phase, for example. In the context of this thesis, it is reasonable to ask how significant particle-wave interactions are at the source, and if they will result in significant phase space changes in the distribution functions. Therefore it is important to consider the stability of the test particle model distributions obtained, via the addition of noise.

The nature of the model for the noise is determined by the instabilities that one expects will be excited in the PSBL. Broadband electrostatic noise (BEN) is often seen in the PSBL [*Parks et al.*, 1984; *Matsumoto et al.*, 1994; *Omura et al.*, 1994, 1996], and is thought to be associated with high speed ion flow in the PSBL [*Gurnett and Frank*, 1977; *Eastman et al.*, 1984]. Although BEN appears to occur at all times in the PSBL, it is mainly absent from the lobe and CPS [*Frank et al.*, 1976; *Gurnett et al.*, 1976; *Williams*, 1981; *Lui et al.*, 1983; *Eastman et al.*, 1984]. The frequency of PSBL BEN ranges from about 10 Hz up to the local electron plasma frequency, ω_{pe} . Most of the wave power is concentrated at low frequencies (<100 Hz), with a steady decrease in wave power up to the electron plasma frequency [*Gurnett et al.*, 1976]. Theoretical studies on the origin of BEN abound [*Grabbe and Eastman*, 1984; *Grabbe*, 1987; *Ashour-Abdalla and Okuda*, 1986; *Schriver and Ashour-Abdalla*, 1987, 1990; *Dusenbery and Lyons*, 1985; *Dusenbery*, 1986], and have greatly advanced the understanding of BEN generation. In this work the mechanism of BEN formation

will not be considered. Instead the effect of model BEN on the distribution functions will be considered. Although some of the BEN wave spectrum has been observed to have oblique wave propagation, in this preliminary model only electrostatic instabilities which are magnetic field-aligned will be taken into account. A three species Maxwellian plasma will be considered - viz. a warm electron background, an ion core term (both with zero drift velocity), and an ion beam term. This particular case is well studied [*Fried and Wong*, 1966; *Grabbe and Eastman*, 1984; *Akimoto and Winske*, 1985; *Dusenbery and Lyons*, 1985; *Dusenbery*, 1986; *Akimoto and Omidi*, 1986; *Ashour-Abdalla and Okuda*, 1986; *Grabbe*, 1987; *Schrivver and Ashour-Abdalla*, 1987; *Roth et al.*, 1989]. For this situation the electrostatic linear dispersion relation is given by

$$0 = 1 + \sum_{\sigma=e,i,b} \frac{1}{k^2 \lambda_\sigma^2} (1 + \zeta_\sigma Z_\sigma). \quad (5.5.4.1)$$

where the subscripts e , i , and b refer to the electrons, ion core, and ion beam terms, respectively. The species' Debye length is given by

$$\lambda_\sigma = (\epsilon_0 k_B T_\sigma / n_\sigma e^2) \quad (5.5.4.2)$$

where ϵ_0 is the permeability of space, k_B is Boltzmann's constant, T_σ is the temperature, n_σ is the number density, and e is the charge. The function $Z_\sigma = Z(\zeta_\sigma)$ is the plasma dispersion function, derived from

$$Z'(\zeta_\sigma) = -2[1 + \zeta_\sigma Z(\zeta_\sigma)]; \quad Z(0) = i\pi^{1/2} \quad (5.5.4.3)$$

and the argument is

$$\zeta_\sigma = (\omega - kV_\sigma)/V_{th\sigma||} \quad (5.5.4.4)$$

V_σ is the species' drift velocity, ω is the complex wave frequency, and

$$V_{th\sigma||} = \sqrt{2k_B T_{\sigma||}/m_\sigma} \quad (5.5.4.5)$$

is the thermal velocity along the ambient magnetic field direction; $T_{\sigma||}$ and m_σ are species' parallel temperature and mass, respectively.

5.4.1 Solution of the electrostatic dispersion relation

Analytic solutions

For a plasma comprising an ion beam, stationary ions, and warm electrons, beam acoustic modes can arise, with $\omega/k \sim \pm V_b$. The electrostatic instabilities that can arise for parallel propagation are the ion-electron acoustic instability [Grabbe and Eastman, 1984] and the ion-ion acoustic instability [Gary and Omid, 1987]. Both of these instabilities generate waves with similar dispersion relations, i.e. $\omega \propto k$.

In the PSBL typically $\zeta_{i,b} \gg 1$ and $\zeta_e \ll 1$ [Grabbe and Eastman, 1984]. Through use of the appropriate expansions for the plasma dispersion function equation (5.5.4.1) reduces to

$$0 = 1 + \frac{1}{k^2 \lambda_e^2} - \frac{\omega_{pi}^2}{\omega^2} - \frac{\omega_{pb}^2}{(\omega - kV_b)^2} \quad (5.5.4.6)$$

Solutions are first sought for the instability depending on the interaction between the beam and the electrons. For this case, one can ignore the ion core term. Then

the solution for the ion-electron acoustic instability has approximate frequency and growth rate given by

$$\omega_r \approx kV_b - \frac{kC_{ia}}{(k^2\lambda_e^2 + 1)^{1/2}} \left[\frac{n_b}{n_e} + \frac{3T_b}{T_e}(k^2\lambda_e^2 + 1) \right]^{1/2} \quad (5.5.4.7)$$

and

$$\gamma \approx \left(\frac{\pi}{8}\right)^{1/2} \left(\frac{m_e n_b}{m_i n_e}\right)^{1/2} \omega_r. \quad (5.5.4.8)$$

where $C_{ia} = \sqrt{k_B T_e / m_i}$ is the sound speed. The ion beam will thus excite ion-acoustic waves propagating close to the beam velocity provided it is far enough away from the thermal electron distribution to not be Landau damped; a condition for this instability to exist is $V_b > C_{ia}$.

For the ion-ion acoustic instability the solution is more complicated because this instability depends on the interaction between the ion beam and core terms. The approach of *Mikhailovskii* [1974] can be followed by looking for solutions near the crossing of the ion-acoustic and beam modes, viz.

$$\omega_r = \omega_{ia}(k_r) = k_r V_b \quad (5.5.4.9)$$

where k_r is the wavenumber at the crossing of the acoustic and beam modes and

$$\omega_{ia}^2(k) = \frac{\omega_{pi}^2 k^2 \lambda_e^2}{1 + k^2 \lambda_e^2} \quad (5.5.4.10)$$

Let

$$\omega = \omega_r + \delta\omega$$

$$k = k_r + \delta k \quad (5.5.4.11)$$

where $\delta\omega$ is a small complex frequency shift, and δk a small real wavenumber shift. After some manipulation equation 5.5.4.6 can be written in the form

$$(\delta\omega - V_g\delta k)(\delta\omega - V_b\delta k)^2 = \frac{1}{2}\omega_r\omega_{pb}^2 \frac{k_r^2\lambda_e^2}{1 + k_r^2\lambda_e^2} = \xi^3 \quad (5.5.4.12)$$

where the group velocity

$$V_g = \omega_{pi}\lambda_e(1 + k_r^2\lambda_e^2)^{1/2}. \quad (5.5.4.13)$$

Equation (5.5.4.12) can be numerically solved, and the maximum growth rate found is the same as the *Akimoto and Winske* [1985] result, viz.

$$\gamma \simeq \frac{\sqrt{3}}{2^{4/3}} \left(\frac{n_b}{n_e}\right)^{1/3} \omega_r \quad (5.5.4.14)$$

The wavenumber k_r is found to be

$$k_r = \left(\frac{C_{ia}^2}{V_b^2} - 1\right)^{1/2} / \lambda_e, \quad (5.5.4.15)$$

and thus a necessary condition for the ion-ion acoustic mode to be unstable is $V_b < C_{ia}$ [*Omidi*, 1985].

The maximum growth rate for the ion-electron acoustic instability is for parallel propagation, but for perpendicular propagation in the case of the ion-ion acoustic instability. The ion-ion acoustic instability generates parallel propagating waves when the beam velocity is small, and when the velocity is larger than the sound speed maximum wave growth shifts to obliquely propagating waves [*Akimoto and Omidi*, 1986].

Numerical solution

Results are now presented from the numerical solution of equation (5.5.4.1) for growth rate and wave frequency. Figure 5.15 is a plot of normalised peak growth and corresponding frequency and wavenumber versus normalised beam drift speed. The frequencies are normalised to the electron plasma frequency (ω_{pe}) and the beam speed is normalised to the ion core thermal velocity, V_{thi} . Three cases are shown with plots in the different columns corresponding to different values for the density ratio, n_b/n_e . For $n_b/n_e=0.8, 0.7$ parameters chosen are $T_i/T_e=0.09$, $T_b = T_i$, and $T_e=500$ eV. The warm electron temperature is average for the PSBL [Eastman et al., 1984; Lui et al., 1987]. Wave growth can be observed over a wide frequency range and beam drift speeds, V_b . The mode with peak growth at $V_b \approx 4V_{thi}$ is the ion-ion instability. In Figure 5.15 growth at small V_b is due to the ion-ion instability, whereas at higher beam speeds it is due to the ion-electron instability. The maximum growth rate of the ion-electron instability increases as the beam speed becomes larger. The first two columns correspond approximately to the model density ratios at $X=-21 R_E$ and $-34 R_E$, respectively. The third column, with $n_b/n_e = 0.2$, corresponds to the situation at approximately $X=-85 R_E$, and has $T_e/T_i=2$ and $T_b/T_i=0.05$.

Figure 5.16 plots the dispersion relation solution, $\omega = \omega_r + i\gamma$, at various X -positions along the model boundary (cf. Figure 5.3 for the parameters used). Figure 5.16a shows plots of γ versus ω_r with downtail distance. The position of the maximum growth rate is indicated by the circle markers. Figure 5.16b shows the maximum growth rate as a function of downtail distance, X , and the corresponding real frequency. Near the earth only the ion-electron acoustic mode is unstable, but in the distant tail the ion-ion acoustic mode becomes unstable and the growth rate here is larger than near the earth. As well, the maximum frequency of the ion-ion

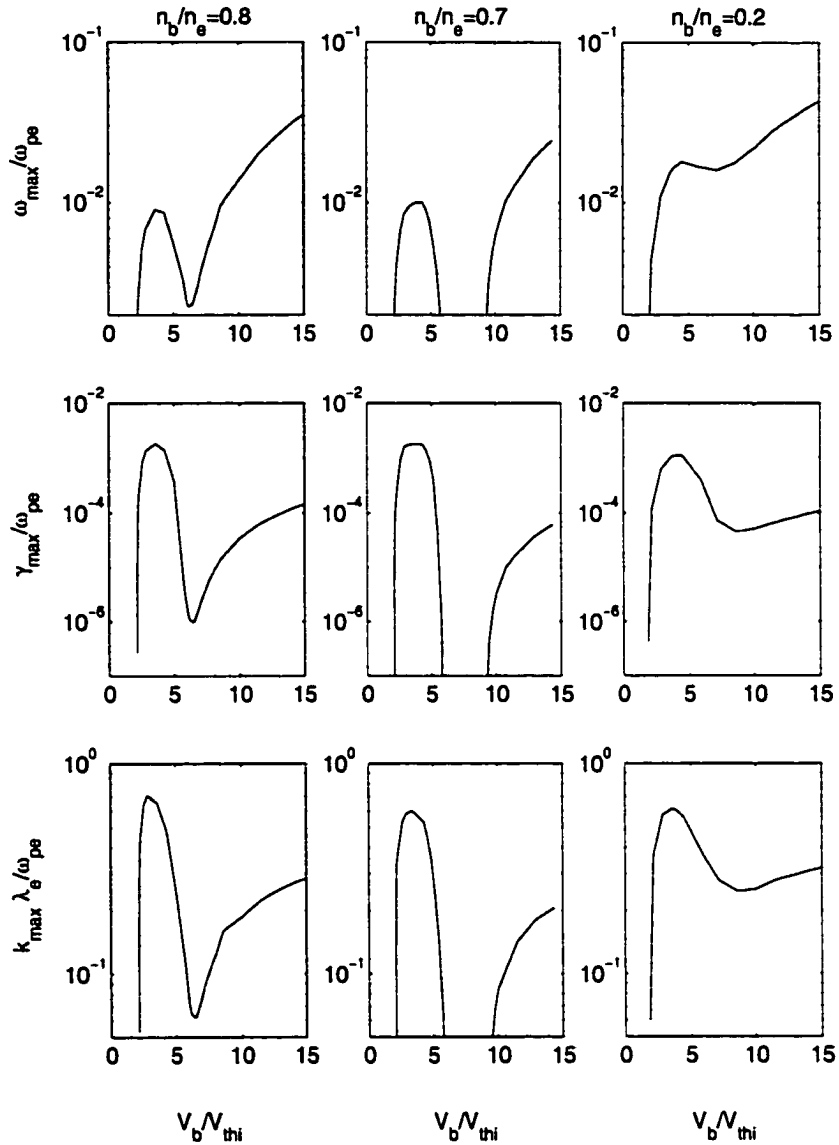


Figure 5.15: Solutions to the kinetic dispersion relation in the simple plasma model for (a.) $n_b/n_e=0.8$, (b.) 0.7., (c.) 0.2. For both (a.) and (b.) $T_i/T_e = 0.09$; $T_i = T_b$; $T_e=500$ eV. These temperatures and densities correspond approximately to the situation at $X=-21 R_E$ ($V_b \sim 12V_{thi}$) and $X=-34 R_E$ ($V_b \sim 10V_{thi}$), respectively, along the model boundary. For (c.) $T_e/T_i=2$ and $T_b/T_i=0.05$. This corresponds to the situation at $X=-85 R_E$ ($V_b \sim 2.5V_{thi}$). The upper panels show the normalised frequency at peak growth versus normalised beam drift speed. The middle panels show the normalised peak growth, and the bottom panels show the wavenumber at peak growth.

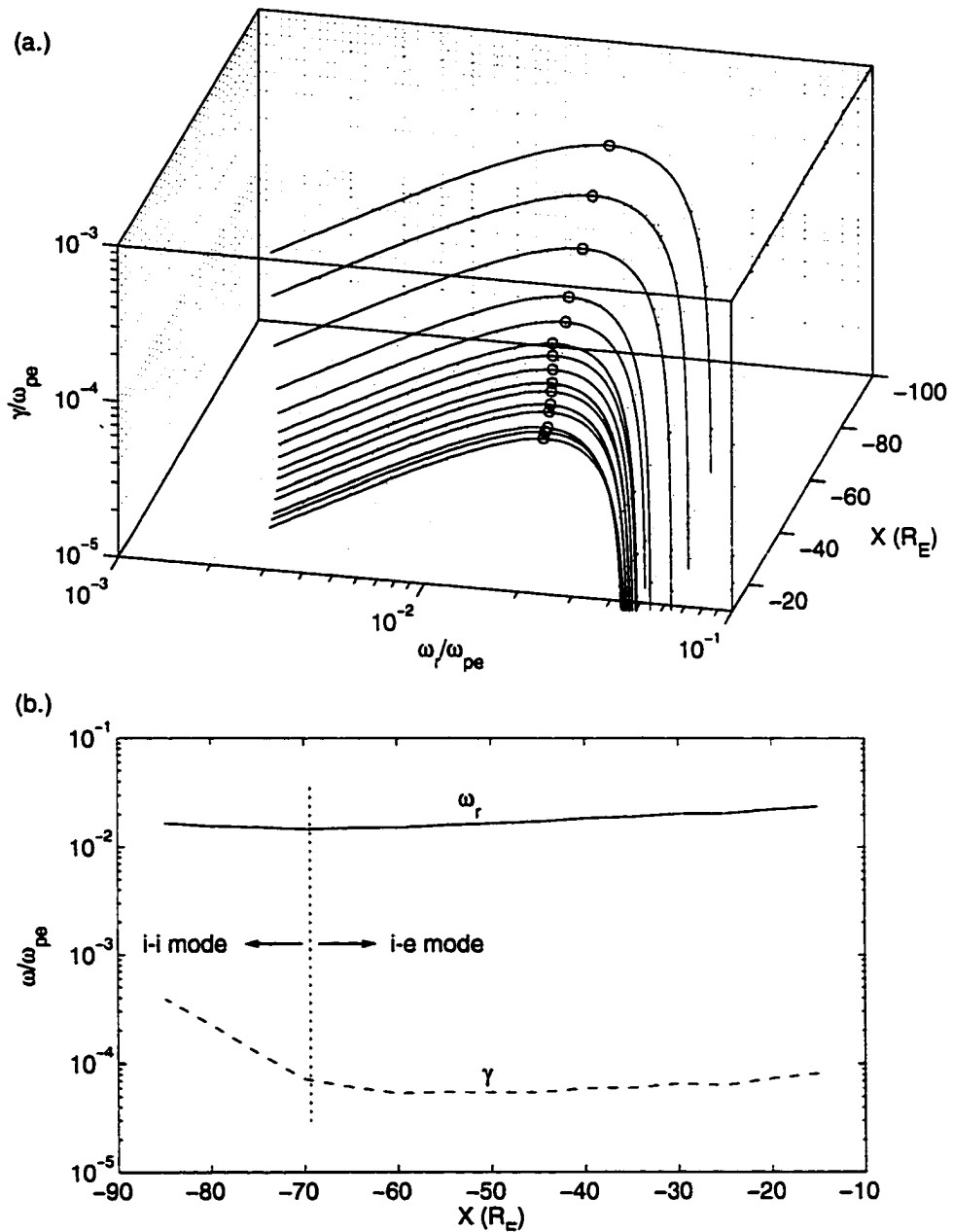


Figure 5.16: (a.) Growth rate γ versus ω_r as a function of downtail distance. The position of the maximum growth rate is indicated by the circle markers. (b.) Maximum growth rate, γ , as a function of downtail distance, X , and the corresponding real frequency, ω_r , all normalised to the electron plasma frequency ω_{pe} . The vertical line separates the regions where the instability is dominated by the ion-ion or ion-electron acoustic modes.

acoustic mode is less than that for the ion-electron acoustic mode.

5.4.2 Electrostatic noise spectrum

The model for the noise comprises only a perturbation electric field, parallel to the ambient magnetic field direction. The ES noise will affect the model distribution functions through the source terms at the model boundary. It will be assumed that the BEN only occurs in the model PSBL and is absent from the CPS [Frank *et al.*, 1976; Gurnett *et al.*, 1976; Williams, 1981; Lui *et al.*, 1983; Eastman *et al.*, 1984]. The effect of the ES noise will be to perturb the observed velocity of individual particles at the boundary, hence producing phase space changes. In a one-dimensional case, with the source distribution at the boundary given by

$$f_0(V) = A \exp\left(\frac{-V^2}{V_{th}^2}\right), \quad (5.5.4.16)$$

a modification in velocity V will result in a diffusive change in the phase space. That is, the phase space density will be modified as

$$f_1(V) = f_0(V) \exp\left(\frac{-\delta V(\delta V - 2V)}{V_{th}^2}\right), \quad (5.5.4.17)$$

where the perturbation in the velocity for the i th particle, due to the ES noise, is given by

$$\delta V_i = \frac{e}{m} \int_t \int_x E(x) S(x - x_i) dx dt \quad (5.5.4.18)$$

The parameters e and m are the proton charge and rest mass, $E(x)$ is the perturbation electric field from the ES noise model as a function of downtail position, and $S(x - x_i)$

is a particle shape function.

The perturbation electric field is obtained by summing the electric field in k -space, E_k , via

$$\vec{E}(\vec{x}) = \sum_k |E_k| \operatorname{Re}[e^{i(\omega_k t + \delta_k)}] \quad (5.5.4.19)$$

where ω_k is the dispersion at a given downtail position, and δ_k is a random phase factor. The electric field is normalised to have an intensity of $\bar{5}$ mV/m [Gurnett *et al.*, 1976]. Due to the ordering of the phase velocity ($\omega > kV_b$), only non-resonant particles interact with the wave. Applying this to the non-resonant particles described by equation (5.5.4.18) therefore results in a velocity perturbation appropriate for non-resonant particle diffusion, viz.

$$\delta V_i = \frac{e}{m} \sum_k |E_k| \frac{\sin(\omega_k t + \delta_k)}{\omega_k} \quad (5.5.4.20)$$

The model boundary, viz. the last closed field line which crosses the NS at $X = -100 R_E$, is divided into a grid, with a grid spacing of $\bar{5} R_E$. Then the BC's (temperatures, densities, and beam velocity), indicated in Figure 5.3, were used to solve the plasma dispersion relation. The dispersion results have been previously shown in Figure 5.16. Two model fluctuation spectra, E_k , were chosen for comparison. viz. (1.) Gaussian spectrum, (2.) white noise spectrum. The maximum of the fluctuation spectrum was normalised so that the model perturbation electric field was consistent with observed BEN electric field amplitudes in the PSBL. For the first case

$$E_k^2 \sim e^{-(k-k_{max})^2/2dk^2}, \quad (5.5.4.21)$$

where k_{max} is the wavenumber at maximum growth (determined from linear theory), and dk is the half-width of the Gaussian distribution. The half-width is estimated from a fit of the linear growth rates that were calculated for different downtail positions. For the second case

$$E_k^2 \sim constant. \quad (5.5.4.22)$$

Of course, the power spectrum of each Fourier mode has sharp peaks. Instead of simply using a delta-function for the wave modes, the spectrum was fitted to a Gaussian so that some wave power is present around the maximum ω_k . The white noise fit to individual modes is not as realistic, since it ascribes equal power to all wavelengths. However, BEN is likely to be caused by a superposition of different wave modes, many of which are not considered here. A summation over Fourier modes corresponds to a single point observation as from satellites, and will give a broader spectrum. Thus the white noise case is a crude approximation to the broadband spectrum.

5.5 Ion distributions from 'first order' test particle simulations

The first order model creates distribution functions as before, but now the additional effects of the perturbation electrostatic field are included. This model electric field, described in the previous section, provides a ballistic push in velocity space to individual test particles once they arrive at the model boundary. The stability of beams and CPSDE is investigated via the addition of this noise.

5.5.1 PSBL/CPS region

Figure 5.17 shows two-dimensional cuts of the velocity distribution calculated in the noon-midnight meridian at $(X,Z)=(-20,1) R_E$. For this case a Gaussian spectrum was used. Figure 5.18 shows the same plots, but now using a white noise spectrum. The different plots show cuts in the $V_B - V_C$ plane for noise levels labelled by A_o , which refers to the electric field intensity normalised to 5 mV/m. A_o varies between 1 (=5 mV/m) and 40 in this figure. Only Figures 5.17a,b and 5.18a,b have noise levels that are the same order of magnitude as satellite observations. The other plots are included to demonstrate the effect of increasing noise intensity on the distribution function. For $A_o=1$ only very slight changes occur in the distribution function, but the beams are not grossly affected. It is only at much higher intensities that the velocity space diffusion becomes substantial. This indicates that realistic electric field intensities do not result in the beams being destroyed.

5.5.2 CS region

As for the PSBL case, realistic electrostatic noise intensities produce only small phase space changes in the model distribution functions. Figures 5.19 and 5.20 show the variation of the distribution function for different noise levels, for the Gaussian and white spectra, respectively. The velocity distribution shown is calculated in the CS region, at $(X,Z)=(-26,0.0001) R_E$. The diffusion in phase space is most effective for the white noise case - the case $A_o=40$ shows that the CPSDE is still evident for the Gaussian noise (Figure 5.19f), but it is completely destroyed in the white noise case (Figure 5.20f).

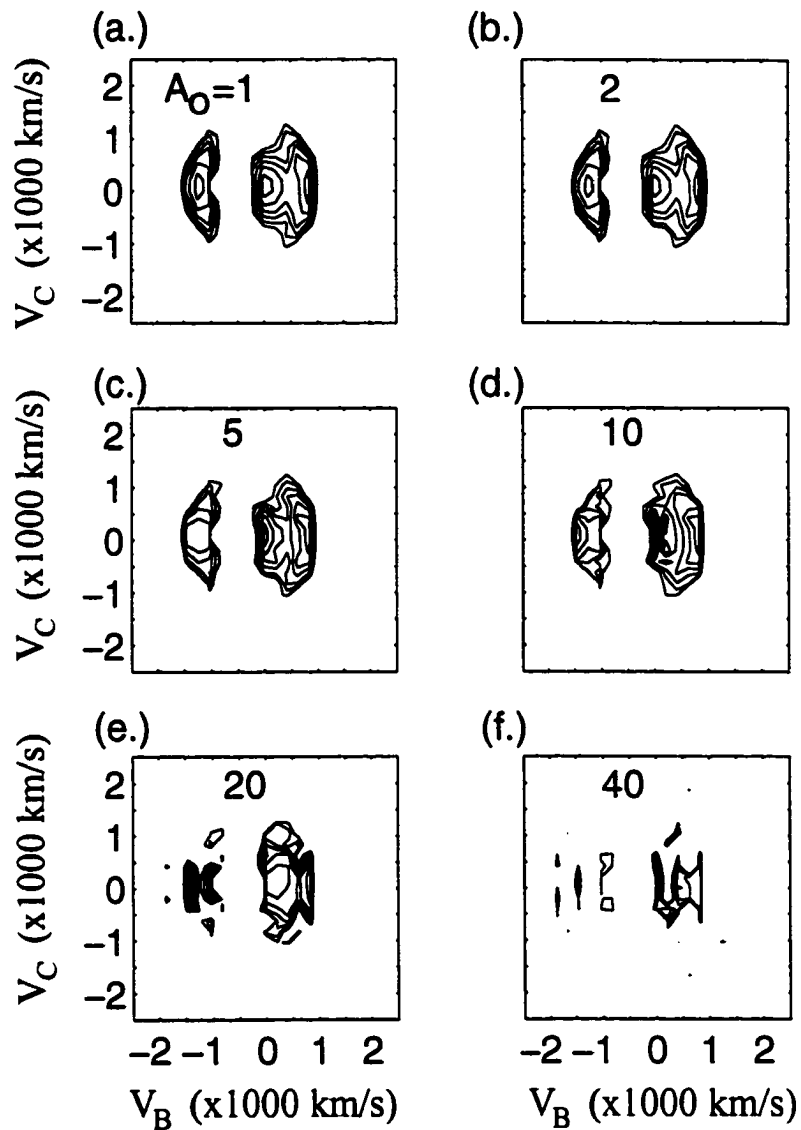


Figure 5.17: Two-dimensional cuts of the distribution function calculated in the noon-midnight meridian and at $(X,Z)=(-20,1) R_E$. The parameter A_0 refers to the electric field intensity normalised to 5 mV/m, and varies from (a.) 1 to (f.) 40. A Gaussian electrostatic spectrum was used for this case.

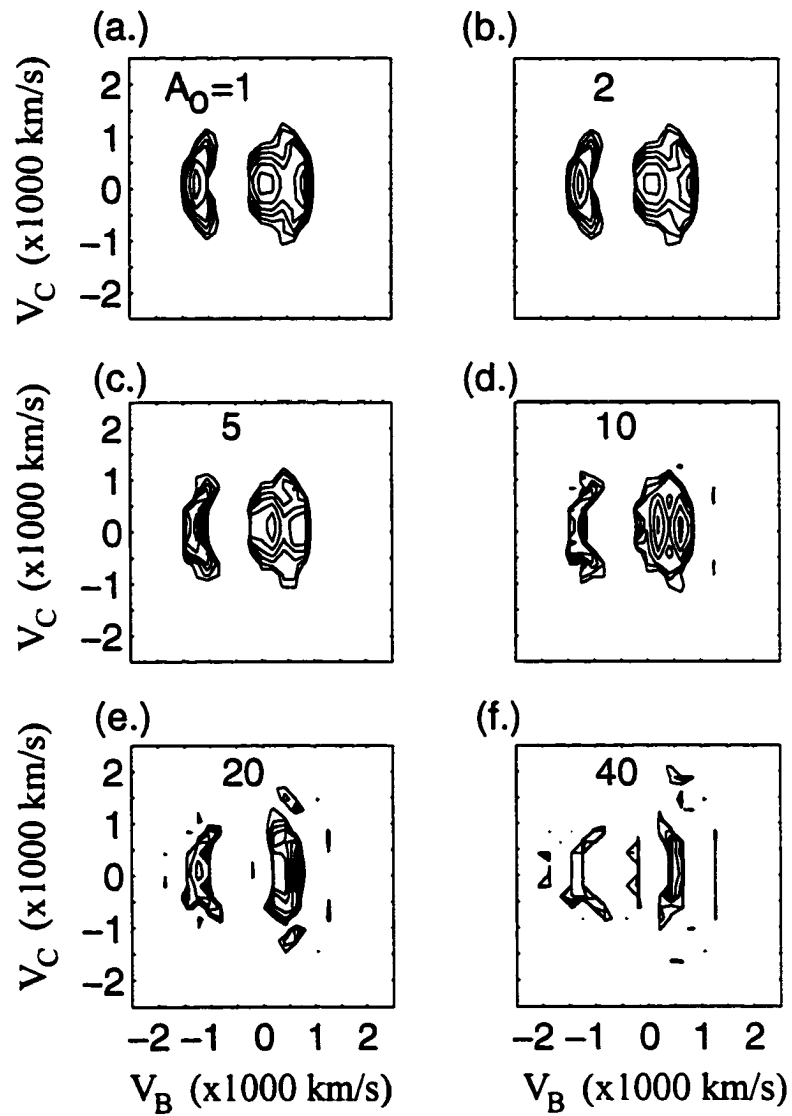


Figure 5.18: Two-dimensional cuts of the distribution function calculated in the noon-midnight meridian and at $(X,Z)=(-20,1) R_E$. The parameter A_0 refers to the electric field intensity normalised to 5 mV/m, and varies from (a.) 1 to (f.) 40. A white electrostatic spectrum was used for this case.

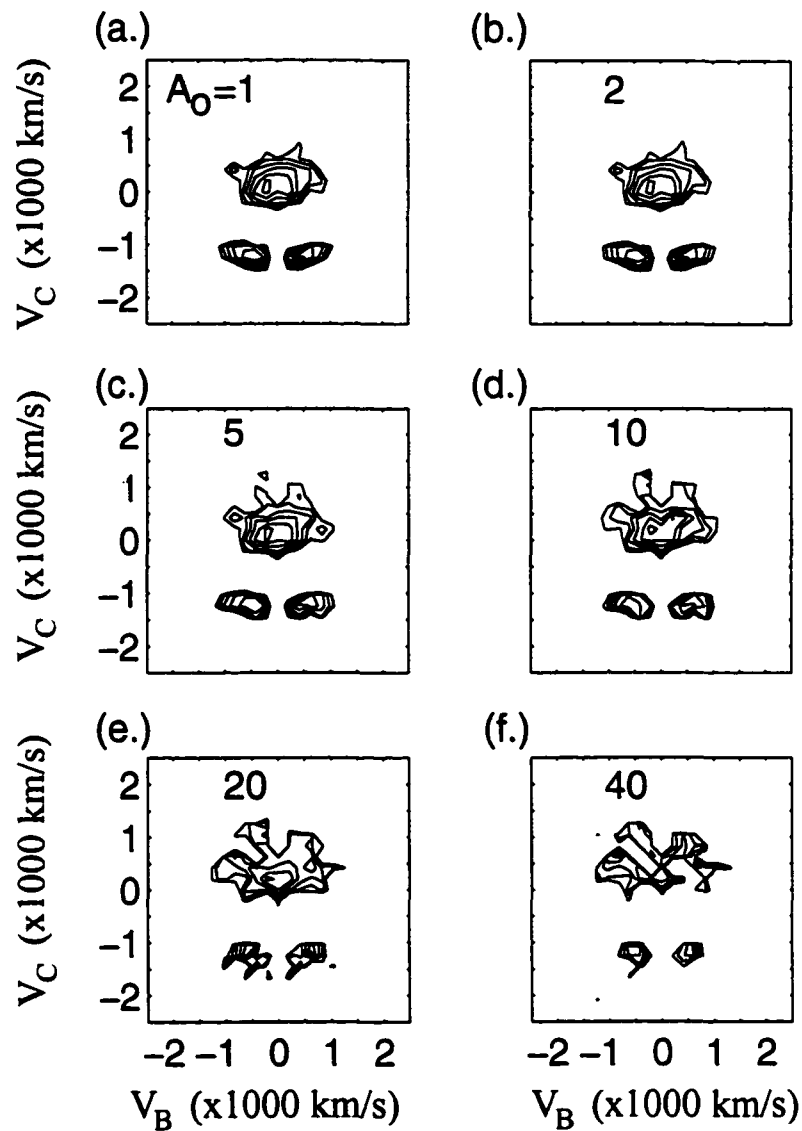


Figure 5.19: Two-dimensional cuts of the distribution function calculated in the noon-midnight meridian and at $(X,Z)=(-26,0.0001) R_E$. The parameter A_0 refers to the electric field intensity normalised to 5 mV/m, and varies from (a.) 1 to (f.) 40. A Gaussian electrostatic spectrum was used for this case.

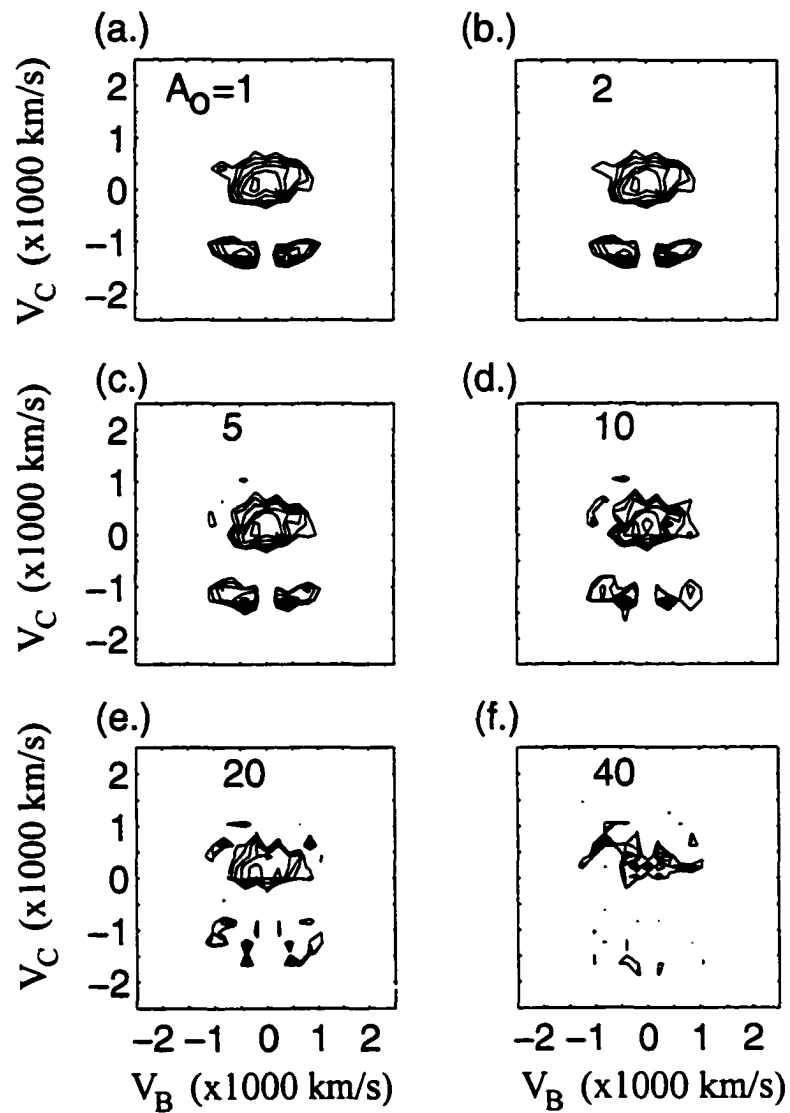


Figure 5.20: Two-dimensional cuts of the distribution function calculated in the noon-midnight meridian and at $(X,Z)=(-26,0.0001) R_E$. The parameter A_0 refers to the electric field intensity normalised to 5 mV/m, and varies from (a.) 1 to (f.) 40. A white electrostatic spectrum was used for this case.

5.6 Summary

The work presented in this chapter is based on the numerical modelling of ion distributions in the magnetotail. It was found that mirroring of initially earthward beams, and their subsequent convection to the CS region, should be considered a strong potential candidate for the mechanism behind anti-earthward anisotropic flows in a stretched magnetotail geometry. Strong tailward flows ($> 300 \text{ km/s}$) were observed in the CS region at $X = -20$ to $30 R_E$.

Despite the limitation of the test-particle model, it has the advantage that it makes only a small number of assumptions and is basically very simple; it just follows the exact trajectories in a model of electric and magnetic fields. It predicts quite complicated and sophisticated shapes for proton distributions in certain regions of the magnetotail. Especially in the CS region, the results have shown that ion behaviour is very different from the usual guiding centre approximation, and results in asymmetry in the ion distribution functions. This means that the distributions should have a complicated three-dimensional structure, which requires an appropriate experimental three-dimensional measurement technique. It is not sufficient to form conclusions based on moments only, especially in the CS region.

The addition of a model electrostatic field does not result in large changes in the phase space. With realistic electrostatic field intensities the beams and other non-isotropic features remain stable in the model simulations. Large changes are only achieved when electrostatic field intensities are used that are an order of magnitude or more above satellite observations.

CHAPTER 6

Concluding remarks

Conventional explanations of fast ion flows in the earth's magnetotail focus on neutral line acceleration mechanisms. The question raised in this thesis was: is it possible that a mechanism related entirely to PSBL dynamics can account for at least some fast magnetotail flows? A positive answer does not negate the likelihood that neutral lines do in fact cause fast flows to jet away from them, but rather suggests caution in automatically assuming that fast flows are always caused by neutral lines. The results of model simulations presented here show that fast tailward flows, on the order of several hundred kilometres per second, can occur in the magnetotail CS region purely as the result of PSBL dynamics. The model that was developed applies to the latter stages of the substorm growth phase, when the magnetotail field varies slowly. It does not apply to fast flows that occur after expansive phase onset, when the magnetic field is highly variable and dynamic.

6.1 Summary of results

6.1.1 Plasma flows in the magnetotail

Data from the WIND satellite were considered during times when fast ion flows were observed in the earth's magnetotail. Velocity distribution functions were calculated over two different count times, viz. 96- and 48-s, in order to compare the differences

in the velocity moments derived from these distributions. The primary results relate to aliasing effects on velocity moment calculations.

- Based upon the observational results it can be concluded that calculation of velocity moments from distribution functions which are computed over integration times that do not adequately resolve magnetic field variations can generate ambiguous results.
- Errors of more than 200 *km/s* can arise between moments calculated using 48- and 96-second distribution functions. Differences are most pronounced when the magnetic field is rapidly varying, thus making separation into parallel and perpendicular flows more uncertain.
- These observational results suggest that caution should be exercised in studies that automate the separation of velocity moments into parallel and perpendicular components.

6.1.2 Magnetic field model development

The magnetic field model, which was developed to study magnetotail flows, yielded important information regarding the growth phase of the magnetospheric substorm. The model is made up of three components, viz. dipole, crosstail, and weak field region (WFR) components.

- It was demonstrated that during the course of the growth phase the equatorward motion of region H_{β} luminosity corresponds to thinning and earthward motion of the crosstail current sheet.
- The equatorward motion of the luminosity was therefore shown to be the consequence of stretching of the magnetotail topology.

- For the March 9, 1995 substorm the model inner edge of the plasma sheet was predicted to move from $\sim 7.8 R_E$ to $5.8 R_E$ during the growth phase.
- The model magnetic field predicted that the crosstail current sheet can thin dramatically during the growth phase, from $\sim 2 R_E$ to $0.1 R_E$ in less than 40 minutes.
- The current sheet can remain very thin ($\sim 0.1 R_E$) for tens of minutes prior to expansive phase onset.

6.1.3 Test particle simulations

Ion flows in the magnetotail were modelled using the new magnetic field. The technique that was followed utilised Liouville's theorem to calculate model distribution functions at several locations in the magnetotail. In effect, the investigation considered the consequences of ion beams in the PSBL in terms of possible flows at lower latitudes.

- The simulations of the CPS show that the velocity distributions contain complicated forms, including asymmetries and counterstreaming.
- All beams have $T_{\perp}/T_{\parallel} > 1$.
- Tailward counterstreaming beams have higher speeds than their earthward counterparts. Near the edge of the PSBL the tailward beams have lower T_{\perp} than their earthward counterparts, but deeper in the CPS they have higher T_{\perp} than the earthward beams.
- There is no clear distinction between the PSBL and CPS since distributions with large streaming components occur throughout the CPS.
- Ion distribution functions computed in the CS region include complicated tailward

CPSDE components.

- These CPSDE components contribute to bulk tailward flows ($V > 300 \text{ km/s}$) in the CS region that are perpendicular to the magnetic field direction.
- A simple model of the electrostatic noise in the PSBL showed that the calculated distribution functions remain stable provided the model noise level is within reasonable levels, as determined from satellites. Large diffusion in velocity space only occurs for noise levels an order of magnitude too large.

6.2 Future work

Anisotropic anti-earthward flows in the magnetotail are usually interpreted in terms of a neutral line. A neutral line may be responsible for some fast flows, but this thesis presents an alternative explanation: for at least some of the time, particularly prior to expansive phase onset, tailward flows are a natural result of PSBL dynamics. Theoretical considerations indicate that the attribution of fast bursty flows to a neutral line is not inevitable or necessary [Liu, 2000]. As well, experimental evidence exists which suggests that tailward flows are not necessarily the *smoking gun* for a neutral line earthward of the spacecraft. For example, Lyons *et al.* [1999, 2000] found evidence that CPS and PSBL flows may not be distinct phenomena, and that significant flows exist throughout the entire extent of the PS. They suggested that tailward flows could be associated with some flapping motion of the magnetotail. The results of this thesis suggest that tailward flows exist irrespective of flapping motion, although such motion would certainly make the situation more complex. In order to truly settle the issue of whether some anisotropic anti-earthward flows in the magnetotail are a consequence of PSBL dynamics, further detailed experimental evidence is required.

This thesis has not provided an experimental basis to settle this issue. Whether all of the modelled features occur in the real magnetotail remains to be demonstrated through experimental observations of ion distribution functions measured during late growth phase, for example. A careful, detailed experimental study of ion distribution functions in the magnetotail is thus required to properly answer our question. The model predicts that tailward flows in the CS region will occur during times when the magnetotail is highly stretched. One difficulty that arises in satellite experiments is that it is very difficult to sample a stretched magnetic topology, with a thin current sheet. For example, a satellite moving at 5 km/s through a $0.1 R_E$ current sheet will traverse the CS region in about two minutes. This should be sufficient time to observe several distribution functions, but the situation is complicated in that the magnetotail is itself a moving target. Traditional single-satellite measurements cannot unambiguously distinguish between spatial and temporal variations. With the recent launch of Cluster-II (July 2000), a formation of four scientific satellites, space-time ambiguity may be resolved, and a greater number of local measurements could be available to finally settle this issue.

Bibliography

Akasofu S.I. et al., Magnetotail and boundary layer plasmas at a geocentric distance of $\sim 18 R_E$: VELA 5 and 6 observations, *J. Geophys. Res.*, 78, 7257, 1973.

Akimoto, K. and D. Winske, Ion-acoustic-like waves excited by the reflected ions at the earth's bow shock, *J. Geophys. Res.*, 90, 12095, 1985.

Akimoto, K. and N. Omidi, The generation of broadband electrostatic noise by an ion beam in the magnetotail, *Geophys. Res. Lett.*, 13, 97, 1986.

Alexeev, I. I., E.S. Belenkaya, V.V. Kalagaev, and Yu. G. Lyutov, Electric fields and field-aligned current generation in the magnetosphere, *J. Geophys. Res.*, 98, 4041, 1993.

Angelopoulos, V., R.C. Elphic, S.P. Gary, and C.Y. Huang, Electromagnetic instabilities in the plasma sheet boundary layer, *J. Geophys. Res.*, 94, 15373, 1989.

Angelopoulos, V., W. Baumjohann, C.F. Kennel, F.V. Coroniti, M.G. Kivelson, R. Pellat, R.J. Walker, H. Lühr, G. Paschmann, Bursty bulk flows in the inner central plasma sheet, *J. Geophys. Res.*, 97, 4027, 1992.

Angelopoulos, V., C.F. Kennel, F.V. Coroniti, R. Pellat, M.G. Kivelson, R.J. Walker, C.T. Russell, W. Baumjohann, W.C. Feldman, J.T. Gosling, Statistical characteristics of bursty bulk flows, *J. Geophys. Res.*, 99, 21257, 1994.

Angelopoulos, V., The role of impulsive particle acceleration in magnetotail circulation, *Proc. of the International Conference on Substorms (ICS-3)*, Versailles, France, pp.17-22, ESA, 1996a.

Angelopoulos, V. et al., Statistical characteristics of bursty bulk flow events, *J. Geophys. Res.*, 99, 21257, 1996b.

- Angelopoulos, V., F.S. Mozer, R.P. Lin, T. Mukai, K. Tsuruda, R. Lepping, and W. Baumjohann, Comment on "Geotail survey of ion flow in the plasma sheet: Observations between 10 and 50 R_E " by W.R. Paterson et al., *J. Geophys. Res.*, 104, 17521, 1999.
- Ashour-Abdalla, M., and H. Okuda, Theory and simulations of broadband electrostatic noise in the geomagnetic tail, *J. Geophys. Res.*, 91, 6833, 1986.
- Ashour-Abdalla, M. et al., Large and small scale structures in the plasma sheet: A signature of chaotic motion and resonance effects, *Geophys. Res. Lett.*, 18, 1603, 1991a.
- Ashour-Abdalla, M, J. Büchner, L.M. Zelenyi, The quasi-adiabatic ion distribution in the central plasma sheet and its boundary layer, *J. Geophys. Res.*, 96, 1601. 1991b.
- Ashour-Abdalla, M. et al., Shaping of the magnetotail from the mantle: Global and local structuring, *J. Geophys. Res.*, 98, 5651, 1993.
- Ashour-Abdalla, M. et al., Proton velocity distributions in the magnetotail: theory and observations, *J. Geophys. Res.*, 101, 2587, 1996.
- Baker, D.N. and R.L. McPherron, Extreme energetic particle decreases near geostationary orbit: A manifestation of current diversion within the inner plasma sheet. *J. Geophys. Res.*, 95, 6591, 1990.
- Baker, D.N., T.I. Pulkkinen, R.L. McPherron, J.D. Craven, L.A. Frank, R.D. Elphinstone, J.S. Murphree, J.F. Fennell, R.E. Lopez, and T. Nagai, CDAW-9 analysis of magnetospheric events on 3 May 1996: Event C, *J. Geophys. Res.*, 98, 3815, 1993.
- Baker, D.N., T.I. Pulkkinen, V. Angelopoulos, W. Baumjohann, R.L. McPherron, *J. Geophys. Res.*, 101, 12975, 1996.

- Baker, D.N., T.I. Pulkkinen, J. Büchner, A.J. Klimas, Substorms: A global instability of the magnetosphere-ionosphere system, *J. Geophys. Res.*, 104, 14601, 1999.
- Baker, K.B. and S. Wing. A new magnetic coordinate system for conjugate studies at high latitudes, *J. Geophys. Res.*, 94, 9139, 1989.
- Baumjohann, W., G. Paschmann, and C.A. Cattell, Average plasma properties in the central plasma sheet, *J. Geophys. Res.*, 94, 6597, 1989.
- Baumjohann, W., G. Paschmann, and C.A. Cattell, Characteristics of high-speed flows in the plasma sheet, *J. Geophys. Res.*, 95, 3801, 1990.
- Baumjohann, W. and R.A. Treumann, *Basic Space Plasma Physics*. Imperial College Press, London, pp.318ff., 1996.
- Blanchard, G.T., L.R. Lyons, J.C. Samson, F.J. Rich. Locating the polar cap boundary from observations of 6300 Å auroral emissions, *J. Geophys. Res.*, 100, 7855, 1995.
- Büchner, J. and Zelenyi, L.M., Chaotization of the electron motion as the cause of an internal magnetotail instability and the substorm onset, *J. Geophys. Res.*, 92, 13456, 1987.
- Büchner, J. and Zelenyi, L.M., Regular and chaotic charged particle motion in magnetotail-like field reversals, 1, Basic theory of trapped particle motion, *J. Geophys. Res.*, 94, 11821, 1989.
- Borovsky, J.E., R.C. Elphic, H.O. Funsten, M.F. Thomsen, The earth as a laboratory for flow turbulence in high- β MHD, *J. Plasma Phys.*, 57, 1, 1997.
- Brecht, S.H. and V.A. Thomas, Multidimensional simulations using hybrid particle codes, in *Particle Methods in Fluid Dynamics and Plasma Physics*, ed. J.U. Brackbill

and J.J. Monaghan, p.135, North Holland, NY, 1988.

Burkhart, G.R., P.B. Dusenbery, T.W. Speiser, Particle chaos and pitch angle scattering, *J. Geophys. Res.*, 100, 107, 1995.

Cattell, C.A. and F.S. Mozer, Substorm electric fields in the earth's magnetotail. in *Magnetic Reconnection in Space and Laboratory Plasmas, Geophys. Monogr. Ser.*, vol. 30, ed. E.W. Hones Jr., p.208, AGU, Washington, D.C., 1984.

Chapman, S.C. and C.G. Mouikis, A comparison of self-consistent kinetic and quasi-MHD simulations: Application to a dipolarizing field reversal, *Geophys. Res. Lett.*, 23, 3251, 1996.

Chappell, C.R., T.E. Moore, and J.H. Waite. Jr., The ionosphere as a fully adequate source of plasma for the earth's magnetosphere, *J. Geophys. Res.*, 92, 5896, 1987.

Cladis. J.B., Parallel acceleration and transport of ions from polar ionosphere to plasma sheet, *Geophys. Res. Lett.*, 13, 893, 1986.

Coppi, B., B. Laval, R. Pellat, Dynamics of the geomagnetic tail, *Phys. Rev. Lett.*, 16, 1207, 1966.

DeCoster R.J. and L.A. Frank, Observations pertaining to the dynamics of the plasma sheet, *J. Geophys. Res.*, 84, 5099, 1979.

Delcourt, D.C., J.-A. Sauvaud, R.F. Martin and T.E. Moore. On the nonadiabatic precipitation of ions from the near-Earth plasma sheet, *J. Geophys. Res.*, 101, 17409, 1996.

Donovan, E.F., Modeling the magnetic effects of field-aligned currents, *J. Geophys. Res.*, 98, 13529, 1993.

Dungey, J. W., Interplanetary magnetic field and the auroral zones, *Phys. Rev. Lett.*,

6, 47, 1961.

Dusenbery, P.B. and L.R. Lyons, The generation of electrostatic noise in the plasma sheet boundary layer, *J. Geophys. Res.*, 90, 10935, 1985.

Dusenbery, P.B., Generation of broadband noise in the magnetotail by the beam acoustic instability, *J. Geophys. Res.*, 91, 12005, 1986.

Eastman, T.E., L.A. Frank, W.K. Peterson, and W. Lennartsson, The plasma sheet boundary layer, *J. Geophys. Res.*, 89, 1553, 1984.

Eastman, T.E., L.A. Frank, and C.Y. Huang, The boundary layers as the primary transport regions of the earth's magnetotail, *J. Geophys. Res.*, 90, 9541, 1985.

Eastman, T.E., R.J. DeCoster, and L.A. Frank, Velocity distributions of ion beams in the plasma sheet boundary layer. in *Ion Acceleration in the Magnetosphere and Ionosphere*, (ed.) T. Chang, *Geophys. Monogr. 38*, AGU, Washington D.C., 117, 1986.

Eastman, T.E. et al., Magnetospheric plasma regimes identified using Geotail measurements 1. Regime identification and distant variability, *J. Geophys. Res.*, 103, 23503, 1998.

Elphic, R.C., T.G. Onsager, M.F. Thomsen, and J.T. Gosling, Nature and location of the source of plasma sheet boundary layer ion beams, *J. Geophys. Res.*, 100, 1857, 1995.

Erickson, G.M., On the cause of X-line formation in the near-Earth plasma sheet: Results of adiabatic convection in plasma sheet plasma, in *Magnetic Reconnection in Space and Laboratory Plasmas*, *Geophys. Monogr. Ser.*, vol. 30, ed. E.W. Hones, Jr., p. 296, AGU, Washington, D.C., 1984.

Fairfield, D.H., Magnetotail energy storage and the variability of the magnetotail current sheet, in *Magnetic Reconnection in Space and Laboratory Plasmas, Geophys. Mongr. Ser.*, vol. 30, ed. E.W. Hones Jr., pp. 168-177, AGU, Washington, D.C., 1984.

Fairfield, D.H., N.A. Tsyganenko, A.V. Usmanov, and M.V. Malkov, A large magnetospheric magnetic field database, *J. Geophys. Res.*, 99, 11319, 1994.

Forbes, T.G. et al., Evidence for the tailward retreat of a magnetic neutral line in the magnetotail during substorm recovery, *Geophys. Res. Lett.*, 8, 261, 1981.

Frank, L.A., K.L. Ackerson, and R.P. Lepping, On hot tenuous plasmas, fireballs, and boundary layers in the earth's magnetotail, *J. Geophys. Res.*, 81, 5859, 1976.

Frank, L.A., W.R. Paterson, and M.G. Kivelson, Observations of nonadiabatic acceleration of ions in earth's magnetotail, *J. Geophys. Res.*, 99, 14877, 1994.

Fried, B.D. and A.Y. Wong, Stability limits for longitudinal wave in ion beam-plasma interaction, *Phys. Fluids*, 9, 1084, 1966.

Fusilier, S.A. and T.G. Onsager, Comments on: "New observations of ion beams in the plasma sheet boundary layer", *Geophys. Res. Lett.*, 26, 2637, 1999.

Gary, S.P., and N. Omidi, The ion-ion acoustic instability. *J. Plasma Physics*, 37, 45-61, 1987.

Grabbe, C.L. and T.E. Eastman, Generation of broadband electrostatic noise by ion beam instabilities in the magnetotail, *J. Geophys. Res.*, 89, 3865, 1984.

Grabbe, C.L., Numerical study of the spectrum of broadband electrostatic noise in the magnetotail, *J. Geophys. Res.*, 92, 1185, 1987.

- Gurnett, D.L., L.A. Frank, and R.P. Lepping, Plasma waves in the distant magnetotail, *J. Geophys. Res.*, 81, 6059, 1976.
- Gurnett, D.L. and L.A. Frank, A region of intense plasma wave turbulence on auroral field lines, *J. Geophys. Res.*, 82, 1031, 1977.
- Hardy, D.A., H.K. Hills, J.W. Freeman, Occurrence of the lobe plasma at lunar distance, *J. Geophys. Res.*, 84, 72, 1979.
- Harris, E.G., On a plasma sheath separating regions of oppositely directed magnetic field, *Nuovo Cimento*, 23, 115, 1962.
- Hau, L.N., R.A. Wolf, G.-H. Voight, and C.C. Wu. Steady state magnetic field configurations for the Earth's magnetotail, *J. Geophys. Res.*, 94, 1303, 1989.
- Hau, L.N.. Effects of steady state adiabatic convection on the configuration of the near-earth plasma sheet, 2, *J. Geophys. Res.* 96, 5591, 1991.
- Holland, D.L. and J. Chen, Effects of collisions on the nonlinear particle dynamics in the magnetotail, *Geophys. Res. Lett.*, 18, 1579, 1991.
- Hones, E.W. Jr., Transient phenomena in the magnetotail and their relation to substorms, *Space Sci. Rev.*, 23, 393, 1979.
- Horwitz J.L and M. Lockwood, The cleft ion fountain: A two-dimensional kinetic model, *J. Geophys. Res.*, 90, 9749, 1985.
- Hoshino, M., T. Mukai, T. Yamamoto, and S. Kokubun, Ion dynamics in magnetic reconnection: comparison between numerical simulation and GEOTAIL observations. *J. Geophys. Res.*, 103, 4509, 1998.
- Iijima, T. et al., Substorm currents in the equatorial magnetotail, *J. Geophys. Res.* 98, 17283, 1993.

- Joyce, G., J. Chen, S. Slinker, D.L. Holland, and J.B. Harold, Particle energization near an X line in the magnetotail based on global MHD fields, *J. Geophys. Res.*, 100, 19167, 1995.
- Kan, J.R., L. Zhu, and S.-I. Akasofu, A theory of substorms: onset and subsidence. *J. Geophys. Res.*, 93, 5624, 1988.
- Kaufmann, R.L., Substorm currents: Growth phase and onset, *J. Geophys. Res.*, 92, 7471, 1987.
- Kaufmann R.L. and C. Lu, Cross-tail current: Resonant orbits, *J. Geophys. Res.*, 98, 15447, 1993.
- Kettmann G., T.A. Fritz, E.W. Hones, Jr., and P.W. Daly. Energetic ion anisotropies in the geomagnetic tail 2. Magnetic field and substorm characteristics, *J. Geophys. Res.*, 98, 115, 1993.
- Kokubun, S., and R.L. McPherron, Substorm signatures at synchronous altitude, *J. Geophys. Res.*, 86, 11265, 1981.
- Krauss-Varban, D., F.G.E. Pantellini, and D. Burgess, Electron dynamics and whistler waves at quasiperpendicular shocks, *Geophys. Res., Lett.*, 22, 2091, 1995.
- Kubyskhina, M.V., V.A. Sergeev, T.I. Pulkkinen, Hybrid input algorithm: An even-oriented magnetospheric model, *J. Geophys. Res.*, 104, 24977, 1999.
- Larson, D.J. and R.L. Kauffman, Structure of the magnetotail current sheet. *J. Geophys. Res.*, 101, 21447, 1996.
- Lin, R.P. et al., A three-dimensional plasma and energetic particle investigation for the WIND spacecraft, *Space Sci. Rev.*, 71, 125, 1995.
- Liu, W.W. and T.W. Hill, Effect of plasma mantle injection on the dynamics of the

distant magnetotail, *J. Geophys. Res.*, 95, 18849, 1990.

Liu, W.W., G. Rostoker, and J.C. Samson, Precipitation of hot protons from a stretched near-earth current sheet, *COSPAR Colloquia Series*, V. 9, 165. Elsevier, 1998.

Liu, W.W., Bursty bulk flows without a near-Earth neutral line: Generation of fast intermittent flow in a highly curved magnetic field, accepted *J. Geophys. Res.*, 2000.

Lu, G., N.A. Tsyganenko, A.T.Y. Lui, H.J. Singer, T. Nagai, and S. Kokubun, Modeling of time-evolving magnetic fields during substorms, *J. Geophys. Res.*, 104, 12327, 1999.

Lui, A.T.Y., T.E. Eastman, D.J. Williams, and L.A. Frank. Observations of ion streaming during substorms, *J. Geophys. Res.*, 88, 7753, 1983.

Lui, A.T.Y., Road map to magnetotail dynamics, in *Magnetotail Physics*. ed. A.T.Y. Lui, p.3., Johns Hopkins University Press, Baltimore, Md, 1987.

Lui, A.T.Y., R.E. Lopez, B.J. Anderson, K. Takahashi, L.J. Zanetti, R.W. McEntire, T.A. Potemra, D.M. Klumpar, E.M. Greene, and R. Strangeway, Current disruptions in the near-Earth neutral sheet region, *J. Geophys. Res.*, 97, 1461, 1992.

Lui, A.T.Y., D.J. Williams, R.W. McEntire, S. Ohtani, L.J. Zanetti, W.A. Bristow, R.A. Greenwald, P.T. Newell, S.P. Christon, T. Mukai, K. Tsuruda, T. Yamamoto, S. Kokubun, H. Matsumoto, H. Kojima, T. Murata, D.H. Fairfield, R.P. Lepping, J.C. Samson, G. Rostoker, G.D. Reeves, A.L. Rodger, and H.J. Singer, Multipoint study of a substorm on February 9, 1995, *J. Geophys. Res.*, 103, 17333, 1998.

Lui, A.T.Y., W. Baumjohann, G. Rostoker, Substorm Expansion Onset Mechanism Debated, *EOS Transac.*, Vol. 81, 7, 15 February 2000.

Lyons, L.R. and T.W. Speiser, Evidence for current sheet acceleration in the geomagnetic tail, *J. Geophys. Res.*, 87, 2276, 1982.

Lyons, L.R., T. Nagai, G.T. Blanchard, J.C. Samson, T. Yamamoto, T. Mukai, A. Nishida, S. Kokubun, Association between Geotail plasma flows and auroral poleward boundary intensifications observed by CANOPUS photometers, *J. Geophys. Res.*, 104, 4485, 1999.

Lyons, L.R., T. Nagai, J.C. Samson, E. Zesta, T. Yamamoto, T. Mukai, A. Nishida, and S. Kokubun, Structured currents associated with tail bursty flows during turbulent plasma sheet conditions, *AGU Monograph on Magnetospheric Current Systems*, 2000.

Machida, S., T. Mukai, Y. Saito, M. Hirahara, T. Obara, A. Nishida, T. Terasawa, and K. Maezawa, Plasma distribution functions in the Earth's magnetotail ($X_{GSM} \sim -42R_E$) at the time of a magnetospheric substorm: GEOTAIL/LEP observation, *Geophys. Res. Lett.*, 21, 1027, 1994.

Martin R.F. Jr. and T.W. Speiser, A predicted ion signature of a neutral line in the geomagnetic tail, *J. Geophys. Res.*, 93, 11521, 1988.

Martin, R.F. Jr., T.W. Speiser, K. Klamczynski, Effect of B_y on neutral line ridges and dynamical source ordering, *J. Geophys. Res.*, 99, 23623, 1994.

Martin, R.F., Jr., R. Fricke, T.W. Speiser, Modeled particle signatures of magnetic structures in the geomagnetic tail, *J. Geomag. Geoelectr.*, 48, 809, 1996.

Matsumoto, H., H. Kojima, T. Miyake, Y. Omura, M. Okada, and M. Tsutsui, Electrostatic solitary waves (ESW) in the magnetotail: BEN wave forms observed by GEOTAIL, *Geophys. Res. Lett.*, 21, 2915, 1994.

McPherron, R.L., C.T. Russell, and M.P. Aubry, Satellite studies of magnetospheric substorms on August 15, 1968, 9, Phenomenological model for substorms, *J. Geophys.*

Res., 78, 3131, 1973.

Mikhailovskii, A.B., *Theory of Plasma Instabilities*, vol. 1, Consultants Bureau, New York, 1974.

Mitchell, D.G., D.J. Williams, C.Y. Huang, L.A. Frank, and C.T. Russell, Current carriers in the near-Earth cross-tail current sheet during substorm growth phase, *Geophys. Res. Lett.*, 17, 583, 1990.

Miyashita, Y., S. Machida, A. Nishida, T. Mukai, Y. Saito, and S. Kokubun, GEO-TAIL observations of total pressure and electric field variations in the near and mid-distant tail associated with substorm onsets, *Geophys. Res. Lett.*, 26, 639, 1999.

Nagai, T., M. Fujimoto, Y. Saito, S. Machida, T. Terasawa, R. Nakamura, T. Yamamoto, T. Mukai, A. Nishida, and S. Kokubun, Structure and dynamics of magnetic reconnection for substorm onsets with Geotail observations, *J. Geophys. Res.*, 103, 4419, 1998.

Nakai, H., Y. Kamide, C.T. Russell, Influences of solar wind parameters and geomagnetic activity on the tail lobe magnetic field: A statistical study, *J. Geophys. Research*, 96, 5511, 1991.

Nakai, H and Y. Kamide, A model of the large-scale distribution of the neutral sheet current and its substorm-associated changes, *J. Geophys. Res.*, 99, 2365, 1994.

Nakai, H and Y. Kamide, Magnetic field changes at the neutral sheet associated with substorm expansion onset: A model prediction and observations, *J. Geophys. Res.*, 100, 3521, 1995.

Nakai, H., Y. Kamide, C.T. Russell, Statistical nature of the magnetotail current in the near-earth region, *J. Geophys. Res.*, 102, 9573, 1997.

- Nakamura, M., G. Paschmann, W. Baumjohann, and N. Sckopke, Ion distributions and flows near the neutral sheet, *J. Geophys. Res.*, 96, 5631, 1991.
- Nakamura, M., G. Paschmann, W. Baumjohann, and N. Sckopke, Ion distributions and flows in and near the plasma sheet boundary layer, *J. Geophys. Res.*, 97, 1449, 1992.
- Omidi, N., Broadband electrostatic noise produced by ion beams in the earth's magnetotail, *J. Geophys. Res.*, 90, 12330, 1985.
- Omura, Y., H. Kojima, and H. Matsumoto, Computer simulation of electrostatic solitary waves: A nonlinear model of broadband electrostatic noise, *Geophys. Res. Lett.*, 21, 2923, 1994.
- Omura, Y., H. Matsumoto, T. Miyake, and H. Kojima. Electron beam instabilities as generation mechanism of electrostatic solitary waves in the magnetotail. *J. Geophys. Res.*, 101, 2685, 1996.
- Onsager, T.G. et al., Model of electron and ion distributions in the plasma sheet boundary layer, *J. Geophys. Res.*, 96, 20999, 1991.
- Onsager, T.G. and T. Mukai, The structure of the plasma sheet and its boundary layers, *J. Geomag. Geoelectr.*, 48, 687, 1996.
- Parks, G.K., M. McCarthy, R.J. Fitzenreiter, J. Etcheto, K.A. Anderson, R.R. Anderson, T.E. Eastman, L.A. Frank, D.A. Gurnett, C. Huang, R.P. Lin, A.T.Y. Lui, K.W. Ogilvie, A. Pedersen, H. Reme, and D.J. Williams, Particle and field characteristics of the high-latitude plasma sheet boundary layer, *J. Geophys. Res.*, 89, 8885, 1984.
- Parks, G.K., L.J. Chen, M. Brittnacher, M. McCarthy, R.P. Lin, D. Larsen, T. Phan, H. Reme, T. Sanderson, G. Germany, and J. Spann, New observations of ion beams

in the plasma sheet boundary layer, *Geophys. Res. Lett.*, 25, 3285, 1998.

Parks, G.K., L.J. Chen, M. Brittnacher, M. McCarthy, R.P. Lin, D. Larsen, T. Phan, H. Reme, T. Sanderson, G. Germany, and J. Spann, Reply to Comments on: "New observations of ion beams in the plasma sheet boundary layer", *Geophys. Res. Lett.*, 26, 2639, 1999.

Parks, G.K., L.J. Chen, M. Fillingim, and M. McCarthy, The need for kinetic theories and models for understanding real auroral and tail dynamics. *EOS. Trans. AGU. Spring Meeting, Washington D.C.*, 2000.

Paterson, W.R., L.A. Frank, S. Kokubun, and T. Yamamoto, Geotail survey of ion flow in the plasma sheet: Observations between 10 and 50 R_E , *J. Geophys. Res.*, 103, 11811, 1998.

Paterson, W.R., L.A. Frank, S. Kokubun, and T. Yamamoto, Reply, *J. Geophys. Res.*, 104, 17527, 1999.

Pellinen, R.J. and W.J. Heikkila, Energization of charged particles to high energies by an induced substorm electric field within the magnetotail, *J. Geophys. Res.*, 83, 1544, 1978.

Philipp, W.G. and G. Morfill, The formation of the plasma sheet resulting from plasma mantle dynamics, *J. Geophys. Res.*, 83, 5670, 1978.

Pulkkinen, T.I., et al., Modeling the growth phase of a substorm using the Tsyganenko model and multi-spacecraft observations: CDAW-9, *Geophys. Res. Lett.*, 1963, 1991.

Pulkkinen, T.I., D.N. Baker, R.J. Pellinen, J. Büchner, H.E.J. Koskinen, R.E. Lopez, R.L. Dyson, and L.A. Frank, Particle scattering and current sheet stability in the geomagnetic tail during the substorm growth phase, *J. Geophys. Res.*, 97, 19283, 1992.

Pulkkinen, T.I., D.N. Baker, P.K. Toivanen, R.J. Pellinen, R.H.W. Friedel, and A. Korth, Magnetospheric field and current distributions during the substorm recovery phase, *J. Geophys. Res.*, 99, 10955, 1994.

Pulkkinen, T.I., D.N. Baker, L.L. Cogger, T. Mukai, and H.J. Singer, Coupling of inner tail and midtail processes, in *Substorms-4*, edited by S. Kokubun and Y. Kamide, pp.749-754, Terra Sci., Tokyo, 1998.

Pulkkinen, T.I., D.N. Baker, L.L. Cogger, L.A. Frank, J.B. Sigwarth, S. Kokubun, T. Mukai, H.J. Singer, J.A. Slavin, and L. Zelenyi, Spatial extent and dynamics of a thin current sheet during the substorm growth phase on December 10, 1996, *J. Geophys. Res.*, 104, 28475, 1999.

Rosenbauer H. et al., Heos 2 plasma observations in the distant polar magnetosphere: the plasma mantle, *J. Geophys. Res.*, 80, 2723, 1975.

Rostoker, G. and R. Boström, A mechanism for driving the gross Birkeland current configuration in the auroral oval, *J. Geophys. Res.*, 81, 235, 1976.

Rostoker G., S.-I. Akasofu, W. Baumjohann, Y. Kamide, R.L. McPherron. The roles of direct input of energy from the solar wind and unloading of stored magnetotail energy in driving magnetospheric substorms, *Space Sci. Rev.*, 46, 93, 1987.

Rostoker G and S. Skone, Magnetic flux mapping considerations in the auroral oval and the Earth's magnetotail, *J. Geophys. Res.*, 98, 1377, 1993.

Rostoker, G., et al., CANOPUS - a ground-based instrument array for remote sensing the high latitude ionosphere during the ISTP/GGS program, *Space Sci. Rev.*, 71, 743, 1995.

Roth, I., M.K. Hudson, R. Bergmann, Effects of ion two-stream instability on auroral ion heating, *J. Geophys. Res.*, 94, 348, 1989.

- Samson, J.C., L.R. Lyons, P.T. Newell, F. Creutzberg, B. Xu, Proton aurora and substorm intensifications, *Geophys. Res. Lett.*, 19, 2167, 1992.
- Samson, J.C., Mapping substorm intensifications from the ionosphere to the magnetosphere, in *Proceedings of the International Conference on Substorms 2*, ed. J.R. Kan, J.D. Craven, S.-I. Akasofu, p.189, Univ. Alaska, 1994.
- Sanny, J., R.L. McPherron, C.T. Russell, D.N. Baker, T.I. Pulkkinen, and A. Nishida. Growth phase thinning of the near-Earth current sheet during the CDAW 6 substorm, *J. Geophys. Res.*, 99, 5805, 1994.
- Sarris E.T. and W.I. Axford, Energetic protons near the plasma sheet boundary layer, *Nature*, 277, 460, 1979.
- Sauvaud. J.A. and Delcourt, D., A numerical study of suprathermal ionospheric ion trajectories in three-dimensional electric and magnetic field models, *J. Geophys. Res.*, 92, 5873, 1987.
- Schindler, K., A theory of the substorm mechanism, *J. Geophys. Res.*, 79, 2803, 1974.
- Schriver, D. and M. Ashour-Abdalla, Generation of high frequency broadband electrostatic noise: the role of cold electrons, *J. Geophys. Res.*, 92, 5807, 1987.
- Schriver, David and Maha Ashour-Abdalla, Cold plasma heating in the plasma sheet boundary layer: theory and simulations, *J. Geophys. Res.*, 95, 3987, 1990.
- Schriver, D. and M. Ashour-Abdalla, Consequences of wave-particle interactions on chaotic acceleration, *Geophys. Res. Lett.*, 18, 1607, 1991.
- Sergeev V.A., D.G. Mitchell, C.T. Russell, and D.J. Williams, Structure of the tail plasma/current sheet at $11 R_E$ and its changes in the course of a substorm, *J. Geophys. Res.*, 98, 17345, 1993.

- Sergeev, V.A. et al., In situ observations of magnetotail reconnection prior to onset of a small substorm, *J. Geophys. Res.*, 100, 19121, 1995.
- Sergeev, V.A., R.J. Pellinen, and T.I. Pulkkinen, Steady magnetospheric convection: a review of recent results, *Space Sci. Rev.*, 75, 551, 1996.
- Slavin, J.A., et al., An ISEE 3 study of average and substorms conditions in the distant magnetotail, *J. Geophys. Res.*, 90, 10875, 1985.
- Smets, R., D. Delcourt, and D. Fontaine, Ion and electron distribution functions in the distant magnetotail: modeling of Geotail observations. *J. Geophys. Res.*, 103, 20407, 1998.
- Speiser, T.W., Particle trajectories in a model current sheet. 1. Analytical solutions. *J. Geophys. Res.*, 70, 4219, 1965.
- Speiser, T.W., Particle trajectories in a model current sheet. 2. Applications to auroras using a geomagnetic tail model. *J. Geophys. Res.*, 72, 3919, 1967.
- Speiser, T.W., and L.R. Lyons, Comparison of an analytical approximation for particle motion in a current sheet with precise numerical calculations. *J. Geophys. Res.*, 84, 147, 1984.
- Takahashi, K. and E.W. Hones, Jr., ISEE 1 and 2 observations of ion distributions at the plasma sheet - tail lobe boundary, *J. Geophys. Res.*, 93, 8558, 1988.
- Tidman, D., Turbulent shock waves in plasmas. *Phys. Fluids*, 10, 547, 1967.
- Tsyganenko, N.A. and A.V. Usmanov, Determination of the magnetospheric current system parameters and development of experimental geomagnetic field models based on data from IMP and HEOS satellites, *Planet. Space. Sci.*, 30, 985, 1982.
- Tsyganenko, N.A., Global quantitative models of the geomagnetic field in the cislunar

magnetosphere for different disturbance levels, *Planet. Space Sci.*, 35, 1347, 1987.

Tsyganenko, N.A., A magnetospheric magnetic field model with a warped tail current sheet, *Planet. Space Sci.*, 37, 5, 1989.

Tsyganenko, N.A and M. Peredo, Analytical models of the magnetic field of disk-shaped current sheets, *J. Geophys. Res.*, 99, 199, 1994.

Tsyganenko, N.A. Effects of the solar wind conditions on the global magnetospheric configuration as deduced from data-based models, in *Proc. of ICS-3 Conference on Substorms*, Versailles, France, ESA SP-389, pp.181-185, 1996.

Turner, N.E., D.N. Baker, T.I. Pulkkinen, and R.L. McPherron. Evaluation of the tail current contribution to *Dst*, *J. Geophys. Res.*, 105, 5431, 2000.

Voronkov, I., Friedrich, E., and Samson, J. C., Dynamics of the Substorm Growth Phase as Observed Using CANOPUS and SuperDARN Instruments. *J. Geophys. Res.*, 104: 28491, 1999.

Weimer, D.R., J.R. Kan, and S.-I. Akasofu, Variations of the polar cap potential measured during magnetospheric substorms, *J. Geophys. Res.*, 97, 3945. 1992.

Williams D.J., Energetic ion beams at the edge of the plasma sheet: ISEE 1 observations plus a simple explanatory model, *J. Geophys. Res.*, 86, 5507. 1981.

Williams, D.J., E.C. Roelof, D.G. Mitchell, Global magnetospheric imaging, *Rev. Geophys.*, 30, 3, 183, 1992.

Zelenyi, L., A. Galeev, and C.F. Kennel, Ion precipitation from the inner plasma sheet due to stochastic diffusion, *J. Geophys. Res.*, 95, 3871, 1990.

Zwingmann, W., Self-consistent magnetotail theory: Equilibrium structures including arbitrary variation along the tail axis, *J. Geophys. Res.*, 88, 9101, 1983.